

**PHOTOPHYSICS OF THIOPHENOSALICYLALDIMINE-
FUNCTIONALIZED G1-POLYPROLYLENIMINATO-COPPER
TELLURIDE/ANTIMONIDE CORE-SHELL NANOMATERIALS**



**UNIVERSITY of the
WESTERN CAPE**

**MORONGWA EMMANUEL RAMOROKA
BSc Honours Chemistry**

**A mini-thesis submitted in partial fulfilment of the requirement for
the degree of**

Magister Scientiae in Nanoscience

In the

**Faculty of Science, University of the Western Cape,
Bellville, Cape Town, South Africa**

Supervisor: Prof Emmanuel I. Iwuoha

Co-supervisor: Dr Kwena D. Modibane

January 2018

Keywords

Bimetallic nanoparticles

Metal-chalcogenides nanoparticles

Dendrimers

Core-shell nanoparticles

Photophysics

Photovoltaics

Electrochemical characterization

Schiff base condensation

Chemical reduction

Suzuki coupling reaction

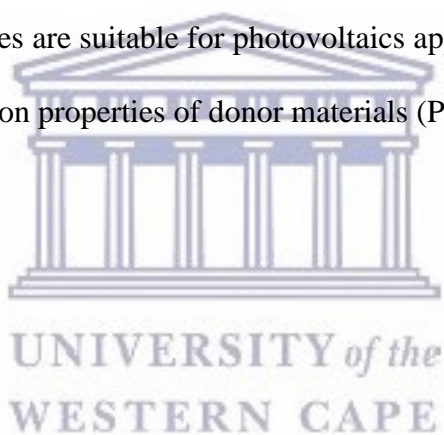


UNIVERSITY *of the*
WESTERN CAPE

Abstract

This work involves the synthesis of copper telluride-polypropylenimine tetra(5-(2-thienyl) salicylaldimine) (CuTe@PPI) and copper antimonide-polypropylenimine tetra(5-(2-thienyl) salicylaldimine) (CuSb@PPI) core-shell nanoparticles (NPs), using two-pots and one-pot synthesis methods, respectively. Their morphology was studied by X-ray diffraction spectroscopy (XRD), high resolution transmission electron microscopy (HRTEM) and high resolution scanning electron microscopy (HRSEM); while their structures were characterized by Fourier transform infrared spectroscopy (FTIR) and elemental analysis. Photophysical properties of the core-shell NPs were determined from ultraviolet-visible absorption spectroscopy (UV-Vis) and photoluminescence spectroscopy (PL). For core-shell NPs produced via two-pots method only CuTe@PPI exhibited $\pi \rightarrow \pi^*$ and $n \rightarrow \pi^*$ which indicate that CuSb@PPI produced via two-pots method was unsuccessfully synthesized. The $\pi \rightarrow \pi^*$ and $n \rightarrow \pi^*$ transitions indicate the presence of polypropylenimine tetra(5-(2-thienyl) salicylaldimine) (PPI) on the surface of CuTe NPs and CuSb NPs. FTIR confirmed coordination of PPI on the surface of CuTe NPs and CuSb NPs by showing a shift in wavenumber of C=N group bands from PPI. HR-TEM showed that the CuTe@PPI synthesized via one-pot method have a wide particles sizes distribution with an average particles size of 13.60 nm while for CuTe@PPI synthesized via two-pots it was impossible to determine the particles size due to aggregation. CuSb@PPI synthesized via two-pots method and one-pot method has a wide particles sizes distribution with an average size of 7.98 nm and 11.61 nm respectively. The average particles sizes determined by HR-SEM were found to be 35.24 nm (CuTe@PPI two-pots method), 33.90 nm (CuTe@PPI one-pot method), 18.30 nm (CuSb@PPI two-pots method), and 16.18 nm (CuSb@PPI one pot method). PL spectra confirmed the polydispersity of synthesized core-shell NPs by showing broad bands and blue

shift of bands as the excitation wavelength decreases which indicates presence of NPs with different particle sizes. The electrochemical behaviour of the core-shell NPs was investigated using cyclic voltammetry (CV) and square wave voltammetry (SWV). They confirmed successful synthesis of CuTe@PPI produced by both methods and CuSb@PPI produced by one-pot method. Core-shell NPs were mixed with Poly[N-9'-heptadecanyl-2,7-carbazole-alt-5,5-(4',7'-di-2-thienyl-2',1',3'-benzothiadiazole)] (PCDTBT) material which is mostly used as donor material in photovoltaics and the photophysical properties of the composite were studied. The photophysical properties of core-shell NPs: PCDTBT composite were compared with those of PCDTBT alone. The core-shell NPs: PCDTBT composites produced a new UV-Vis band at 830 nm indicating that the composites are suitable for photovoltaics application and presence of core-shell NPs improves the absorption properties of donor materials (PCDTBT).



Dedication

I dedicate this work to

My parents

Mr David N Ramoroka and Mrs. Rosina R Ramoroka

&

My Brothers: Michael M Ramoroka, Kenneth L Ramoroka, Obed K Ramoroka and Lethabo K

Ramoroka



UNIVERSITY *of the*
WESTERN CAPE

Declaration

I declare that “**Photophysics of thiophenosalicylaldimine-functionalized G1-polypropyleniminato-copper telluride/antimonide core-shell nanomaterials**” is my own work, that it has not been submitted for any degree or examination in any other university and that all the resources I have used or quoted have been indicated and acknowledged by means of complete references.

Morongwa Emmanuel Ramoroka

January 2018



Signed: 

Acknowledgement

I would like to gratefully and sincerely thank Professor Emmanuel I Iwuoha for his understanding, patience and guidance during my Master's degree studies at the University of the Western Cape. His mentorship was outstanding in providing a well-rounded experience consistent with my long-term career goals. He encouraged me to not only grow as an experimentalist and a chemist, but likewise as an instructor and self-governing thinker. For everything you've done for me, Professor Emmanuel I. Iwuoha, I thank you.

Also, I thank Dr Kwena D. Modibane (University of Limpopo) and Dr Suru V. John (University of the Western Cape) for their support, guidance and many productive discussions. My special thanks go to Mrs. Valencia Jamalie for always helping me with all the administration work.

My friends Mr Ronald Tekanya, Mr Siyabonga B Mdluli, Mr Praise Maapola, Mr Pfano Tshindani, Mr Moses Matlala, Mr Prince Shumbula, Mr Karabo Masha, Mr Luthando Xolo and Mr Joel Ngoasheng, thank you for your support during the entire period of my Masters studies.

I would also like to extend my thanks to the following: SensorLab researchers for their helpful suggestions and friendship, Chemistry Department technical staff and the Electron Microscopy Unit of the University of the Western Cape.

My thanks to the Department of Science and Technology (DST) of South Africa that funded my MSc Nanoscience studies.

I would also like to thank my parents David N. Ramoroka (Father) and Rosina R. Ramoroka (Mother), as well as my brothers Michael M. Ramoroka, Kenneth L. Ramoroka, Obed K. Ramoroka and Lethabo K Ramoroka for their support and encouragement. Finally, I thank the Almighty God, without whom nothing is possible.

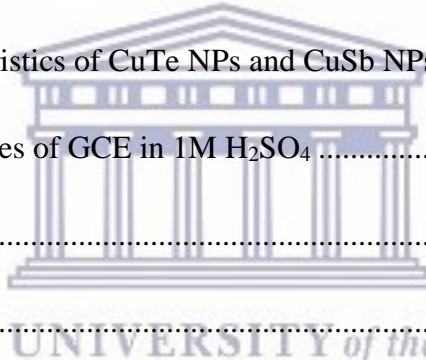
Table of Contents

Keywords	ii
Abstract	iii
Dedication	v
Declaration	vi
Acknowledgement	vii
List of Figure.....	xiii
List of Tables	xvii
List of Schemes.....	xviii
List of Conferences and workshops.....	xix
List of abbreviations	xx
CHAPTER 1: INTRODUCTION.....	1
1.1 Background to the study.....	1
1.2 Aim and Objectives.....	3
1.2.1 Objectives	3
1.3 References	4
CHAPTER 2: LITERATURE REVIEW: CORE-SHELL MATERIALS AS PHOTOVOLTAIC SYSTEMS.....	6
2.1 Abstract.....	6
2.2 Introduction	7



UNIVERSITY of the
WESTERN CAPE

2.3 Environmental impact.....	9
2.4 Types of Core-Shell nanoparticles	10
2.5 Synthesis of Core-Shell nanoparticles.....	17
2.6 Factors affecting the distribution and size of Core-Shell nanoparticles	20
2.7 Application of core-shell nanoparticles in photovoltaics	23
2.8 Conclusion.....	28
2.9 References	29
CHAPTER 3: ANALYTICAL TECHNIQUES AND EXPERIMENTAL METHODS.....	39
3.1 Reagents and materials.....	39
3.2 Characterization Techniques.....	39
3.3 Synthesis of CuSb NPs and CuTe NPs	41
3.4 Synthesis of 5-(2-thienyl)salicylaldehyde (3)	41
3.5 Synthesis of polypropylenimine tetra(5-(2-thienyl)salicylaldehyde) (PPI) (5).....	42
3.6 Core-Shell NPs were synthesized using two-pots method and one-pot method.....	44
3.6.1 Synthesis of Core-Shell Nanoparticles via two-pots method	44
3.6.2 Synthesis of Core-Shell Nanoparticles via one-pot method.....	44
3.7 Blending of PCDTBT and Core-Shell Nanoparticles	44
3.8 References	45
CHAPTER 4: CHARACTERIZATION OF CuTe and CuSb NANOPARTICLES SYNTHESIZED VIA CHEMICAL REDUCTION	47

4.1 UV-Vis studies of the synthesized CuTe NPs and CuSb NPs	47
4.2 FTIR studies of the synthesized CuTe NPs and CuSb NPs	48
4.3 X-ray Diffraction analysis of CuTe NPs and CuSb NPs.....	49
4.4 Morphological and Compositional Analysis of CuTe NPs and CuSb NPs	50
4.4.1 TEM analysis of CuTe NPs and CuSb NPs.....	50
4.4.2 Energy dispersive X-ray (EDX) spectra of the CuTe NPs and CuSb NPs.....	52
4.4.3 SEM analysis of CuTe NPs and CuSb NPs.....	52
4.4.4 Energy dispersive X-ray (EDX) spectra of the CuTe NPs and CuSb NPs.....	53
4.5 Electrochemical characteristics of CuTe NPs and CuSb NPs in sulphuric acid medium ...	54
4.5.1 Electrochemical studies of GCE in 1M H ₂ SO ₄	54
4.6 Sub-Conclusion	59
4.7 References	59
<p style="text-align: center;">  </p>	
CHAPTER 5: CHARACTERIZATION OF SYNTHESIZED POLYPROPYLENIMINE TETRA (5-(2-THIENYL)SALICYLALDIMINE) FIRST GENERATION DENDRIMER (PPI).....	63
5.1 UV-Vis spectroscopy Characterization.....	63
5.2 FTIR analysis of PPI	64
5.3 XRD studies of 5-(2-thienyl) salicylaldehyde and PPI.....	65
5.4 TEM and SEM analysis of PPI	66
5.5 Electrochemical studies of PPI with cyclic voltammetry (CV) and square wave voltammetry (SWV).....	68

5.6 Sub-Conclusion	69
5.7 Reference.....	70
CHAPTER 6: CHARACTERIZATION OF CuTe@PPI and CuSb@PPI CORE-SHELL	
NANOPARTICLES SYNTHESIZED VIA TWO-POTS AND ONE-POT METHODS	72
6.1 UV-Vis studies CuTe@PPI and CuSb@PPI core-shell NPs	72
6.2 FTIR analysis of CuTe@PPI and CuSb@PPI core-shell NPs	74
6.3 PL Characterization of CuTe@PPI and CuSb@PPI NPs	75
6.4 XRD characterization of CuTe@PPI and CuSb@PPI NPs	77
6.5 HR-TEM analysis of core-shell NPs.....	79
6.6 HR - SEM Analysis of CuTe@PPI and CuSb@PPI NPs	82
6.7 EDX Analysis of CuTe@PPI and CuSb@PPI NPs	83
6.8 Electrochemical analysis of Core – Shell NPs	84
6.9 Determination of HOMO and LUMO energy states.....	87
6.10 Sub-Conclusion	88
6.11 References	88
CHAPTER 7: PHOTO-PHYSICAL PROPERTIES OF CORE – SHELL	
NANOPARTICLES:PCDTBT COMPOSITES	92
7.1 UV-Vis characterization.....	92
7.2 PL characterization.....	94
7.3 Absorption, Excitation and Emission spectra	96

7.4 Sub-Conclusion	98
7.5 References	99
CHAPTER 8: CONCLUSIONS	100
8.1 Conclusion.....	100
8.2 Future work	101
8.3 Recommendations	101
8.4 Appendix	102



UNIVERSITY *of the*
WESTERN CAPE

List of Figure

Figure 2. 1: Core-Shell nanoparticles.	8
Figure 2. 2: The structure of Au@PS NPs and architectures of both OPVs and OLEDs [78].	24
Figure 2. 3: The architecture of OPV cell [79].	26
Figure 2.4: Solar cell power conversion efficiency (PCE) as a function of Au@SiO ₂ core-shell NPs concentrations (i) P3HT:PC ₆₀ BM device with Au@SiO ₂ core-shell NPs and (ii) PBDTT-DPP: PC ₆₀ BM Au@SiO ₂ core-shell NPs [79].	27
Figure 2. 5: OPV architecture containing Au@Ag core-shell NPs [81].	28
Figure 4. 1: The absorbance spectra of CuTe NPs (A) and CuSb NPs (B) at room temperature with the variation of $(\alpha h\nu)^2$ versus $h\nu$ for direct band gap calculation for both CuTe NPs (C) and CuSb NPs (D) respectively.	48
Figure 4. 2: FT-IR spectra of CuTe NPs (A) and CuSb NPs (B) milled in KBr at room temperature.	49
Figure 4. 3: Powder X-ray diffraction pattern of CuTe NPs (A) and CuSb NPs (B).	50
Figure 4. 4: TEM image of CuTe NPs (A and C) and CuSb NPs (B and D), Particle sizes distribution of CuTe NPs (E) and CuSb NPs (F).	51
Figure 4. 5: EDX results of CuTe NPs (A) and CuSb NPs (B).	52
Figure 4. 6: SEM image of CuTe NPs (A) and CuSb NPs (B), Particle sizes distribution of CuTe NPs (C) and CuSb NPs (D).	53
Figure 4. 7: EDX results of CuTe NPs (A) and CuSb NPs (B).	54
Figure 4. 8: CV (A) at scan rate of 100 mVs ⁻¹ and SWV (B) of GCE in 1 M H ₂ SO ₄	55

Figure 4. 9: The voltammograms of precursors: (A) Copper, (B) Tellurium, (C) Copper (II) chloride and (D) Antimony (III) chloride in 1 M H ₂ SO ₄ at scan rates of 100 mV s ⁻¹	56
Figure 4. 10: The voltammograms of CuTe NPs and CuSb NPs were obtained at different potential regions: (A) comparison of CuTe NPs with precursors at scan rate of 100 mVs ⁻¹ ; (B) CuTe NPs at different scan rates, (C) SWV of CuTe NPs (D) comparison of CuSb NPs with precursors at scan rate of 100 mVs ⁻¹ ; (B) CuSb NPs at different scan rates, (C) SWV of CuSb NPs at in 1 M H ₂ SO ₄	58
Figure 5. 1: UV-Vis spectra of (A) 2-Thienylboronic acid, 5-bromosalicylaldehyde and 5-(2-thienyl)salicylaldehyde and (B) 5-(2-thienyl)salicylaldehyde, Poly (propylenimine) tetramine G1 dendrimer and PPI.....	64
Figure 5. 2: FTIR spectra of (A) 5-bromosalicylaldehyde (1), 2-Thienylboronic acid (2) and 5-(2-thienyl)salicylaldehyde (3) and (B) 5-(2-thienyl)salicylaldehyde (1), Poly (propylenimine) G1 dendrimer (2) and PPI (3).	65
Figure 5. 3: XRD spectra of (A) 5-(2-thienyl) salicylaldehyde and PPI.	66
Figure 5. 4: HR-TEM images of the synthesized PPI (A and B).....	67
Figure 5. 5: HR-TEM-EDX of PPI.	67
Figure 5. 6: HR-SEM images of the synthesized PPI and HR-SEM-EDX of PPI.	68
Figure 5. 7: (A) CV of 0.05 M PPI and 0.05 M 5-(2-thienyl)salicylaldehyde at scan of 10 mVs ⁻¹ , (B) SWV of 0.05 M PPI and 0.05 M 5-(2-thienyl)salicylaldehyde, (C) CV of 0.05 M 5-(2-thienyl)salicylaldehyde at different scan rates and (D) CV of 0.05 M PPI at different scan rates.	69

Figure 6.1 : UV-Vis spectrum of PPI compared with spectra of (A) CuTe@PPI synthesized via two-pots synthesis (red) and one-pot synthesis (blue) and (B) CuSb@PPI synthesized via two-pots synthesis (red) and one-pot synthesis (blue). 73

Figure 6. 2: $(\alpha h\nu)^2$ against $h\nu$ of synthesized core-shell NPs. 74

Figure 6. 3: FTIR spectrum of PPI compared with spectra of (A) CuTe@PPI synthesized via two-pots synthesis (red) and one-pot synthesis (blue) and (B) CuSb@PPI synthesized via two-pots synthesis (red) and one-pot synthesis (blue). 75

Figure 6. 4: PL spectra of CuTe@PPI synthesized via two-pots synthesis (A) and one-pot synthesis (B), CuSb@PPI synthesized via two-pots synthesis (C) and one-pot synthesis (D)... 77

Figure 6. 5: XRD patterns showing the comparison of (A) CuTe@PPI synthesized via two-pots synthesis with patterns of CuTe NPs and PPI and (B) CuSb@PPI synthesized via two-pots synthesis with patterns of CuSb NPs and PPI..... 78

Figure 6. 6: XRD patterns C and D shows comparison of CuTe@PPI and CuSb@PPI synthesized via two-pots and one-pot methods. 79

Figure 6. 7: HR-TEM images of CuTe@PPI synthesized via two-pots (A, B, and C) and one-pot (D, E and F) at different magnifications of 20 nm, 10 nm and 5 nm..... 80

Figure 6. 8: The particle size of distribution of one-pot synthesized CuTe@PPI (G). HR-TEM-EDX of CuTe@PPI synthesized via two-pots (H) and one-pot (I)..... 80

Figure 6. 9: HR-TEM images of CuSb@PPI two-pots (A, B, and C) and one-pot (D, E and F) and the particle size of distribution of CuSb@PPI (two-pots) G and (one-pot) H.....81

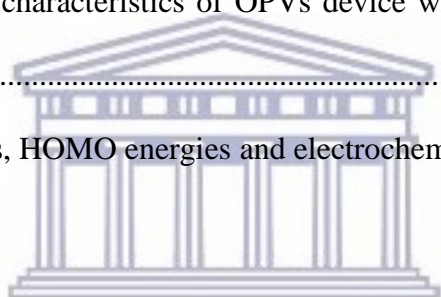
Figure 6. 10: HR-TEM-EDX of CuSb@PPI synthesized via two-pots (I) and one-pot (J)..... 82

Figure 6. 11: HR-SEM images of CuTe NPs (A), CuTe@PPI synthesized via two-pots (B) and one-pot (C), CuSb NPs (D), CuSb@PPI synthesized via two-pots (E) and one-pot (F). The

particle size distribution for CuTe@PPI synthesized via two-pots (G) and one-pot (H) and CuSb@PPI synthesized via two-pots (I) and one-pot (J) are shown.	83
Figure 6. 12: HR-SEM-EDX of CuTe@PPI synthesized via two-pots (A) and one-pot (B) and CuSb@PPI synthesized via two-pots (C) and one-pot (D).....	84
Figure 6. 13: Electrochemical responses of CuTe@PPI synthesized via two-pots and one-pot compared with electrochemical response of CuTe NPs (A and B) at scan rate of 40 mVs^{-1} , C and D shows the response of CuTe@PPI synthesized via two-pots (C) and one-pot (D) at different scan rates.	85
Figure 6. 14: Electrochemical responses of CuSb@PPI synthesized via two-pots and one-pot compared with electrochemical response of CuTe NPs (A and B) at scan rate of 40 mVs^{-1}	86
Figure 6. 15: Electrochemical responses of CuSb@PPI synthesized via two-pots (C) and one-pot (D) at different scan rates.....	87
Figure 7. 1: UV-Vis spectra of PCDTBT and its composites.....	93
Figure 7. 2: UV-Vis spectra of PCDTBT blended with core-shell NPs at different ratios.....	94
Figure 7. 3: PL spectra of PCDTBT blended with core-shell NPs at different ratios.....	95
Figure 7. 4: PL spectra of PCDTBT blended with core-shell NPs at different ratios.....	96
Figure 7. 5: Absorption, excitation and emission spectra for core-shell NPs: PCDTBT composite in chlorobenzene.	98
Figure 8.1: $^1\text{H-NMR}$ spectrum of 5(2-thienyl)salicylaldehyde	102
Figure 8.2: $^{13}\text{C-NMR}$ spectrum of 5(2-thienyl)salicylaldehyde	102
Figure 8.3: $^1\text{H-NMR}$ spectrum of PPI.....	103
Figure 8.4: $^{13}\text{C-NMR}$ spectrum of PPI	103

List of Tables

Table 2. 1: Average emission rates in Kilograms per Megawatt-hour (Kg/MWh) [11].....	9
Table 2. 2: The possible reduction of NO _x , CO ₂ , and SO ₂ via the use of PV technology by 2030 in Gigagram/year (Gg/year) [11].	10
Table 2. 3: Characteristics of OPVs without NPs, with PS and with Au@PS NPs in PEDOT: PSS [78].....	25
Table 2. 4: Characteristics of the Green-Emitting OLEDs device without and with Au@PS NPs [78].....	25
Table 2. 5: Showing electrical characteristics of OPVs device with and without Au@Ag core-shell NPs [81].....	28
Table 6. 1: The LUMO energies, HOMO energies and electrochemical band gaps.	88



UNIVERSITY of the
WESTERN CAPE

List of Schemes

Scheme 3. 1: Synthesis of 5-(2-thienyl) salicylaldehyde.....	42
Scheme 3. 2: Synthesis of polypropylenimine tetra(5-(2-thienyl) salicylaldehyde) (PPI).....	43



UNIVERSITY *of the*
WESTERN CAPE

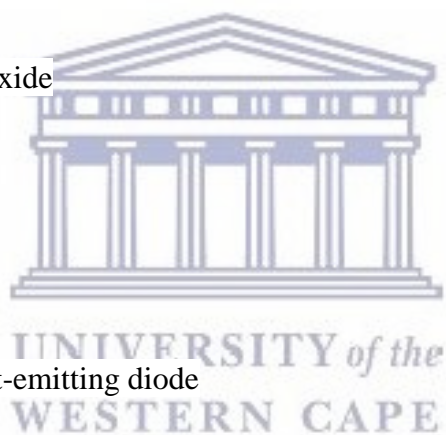
List of Conferences and workshops

- (i) Nanotechnology health, safety and environmental risk research: A necessity and not an impediment in the advancement of nanotechnology benefits, South African Nanoscience and Nanotechnology Summer School, 4-9 December 2016, *Conference*, North-West University, Potchefstroom, South Africa.
- (ii) Photovoltaics of copper telluride dendritic core-shell nanoparticles, The 9th International Conference of the African Materials Research Society, 11-14 December 2017, *Conference*, Gaborone, Botswana.
- (iii) Free liquid surface electrospinning on nanospider technology workshop, The 9th International Conference of the African Materials Research Society, 11-14 December 2017, *Pre-conference workshop*, Gaborone, Botswana.
- (iv) Thin film silicon solar cells and tandem and triple junction cells, including hybrids, Thin Film Photovoltaics Workshop, 10 October 2017, *Workshop*, University of the Western Cape, Bellville, South Africa.
- (v) Potential of hot-wire chemical vapour deposition (HWCVD) and flexible silicon solar cells, Thin Film Photovoltaics Workshop, 12 October 2017, *Workshop*, University of the Western Cape, Bellville, South Africa.
- (vi) Basics and different techniques of Rheometer, Rheometer workshop, 9-10 November 2017, *Workshop*, University of the Western Cape, Bellville, South Africa.

List of abbreviations

NPs	Nanoparticles
CuTe	Copper Telluride
CuSb	Copper Antimonide
PCDTBT	Poly[N-9'-heptadecanyl-2,7-carbazole-alt-5,5-(4',7'-di-2-thienyl-2',1',3'-benzothiadiazole)]
UV-Vis	Ultra-Violet Visible
PL	Photoluminescence
XRD	X-ray powder diffraction
TEM	Transmission Electron Microscopy
SEM	Scanning Electron Microscope
CV	Cyclic Voltammetry
SWV	Square Wave Voltammetry
NMR	Nuclear Magnetic Resonance spectroscopy
FTIR	Fourier-transform Infrared
EDX	Energy-dispersive X-ray spectroscopy
PPI	Polypropylenimine tetra(5-(2-thienyl) salicylaldimine)
CuTe@PPI	CuTe@polypropylenimine tetra(5-(2-thienyl)salicylaldimine)

CuSb@PPI	CuSb@polypropylenimine tetra(5-(2-thienyl)salicylalimine)
CCD	Charge-Coupled Device
CdSe	Cadmium Selenide
CdS	Cadmium Sulfide
ZnS	Zinc Sulfide
ZnSe	Zinc Selenide
Ag	Silver
TiO ₂	Titanium dioxide
Au	Gold
PS	Polystyrene
OLEDs	Organic light-emitting diode
OPVs	Organic photovoltaic cells
PEDOT: PSS	Poly (3, 4-ethylenedioxythiophene): poly (styrene sulfonate)
ITO	Indium tin oxide
SiO ₂	Silicon dioxide
PBDTT-DPP	Poly[2,6'-4,8-di(5-ethylhexylthienyl)benzo[1,2-b;3,4-b]dithiophene-alt-5-dibutyloctyl-3,6-bis(5-bromothiophen-2-yl)pyrrolo[3,4-c]pyrrole-1,4-dione]
PC ₆₀ BM	[6,6]-phenyl-C61-butyric acid methyl ester



P3HT	Poly(3-hexylthiophene)
HOMO	Highest Occupied Molecular Orbital
LUMO	Lowest Unoccupied Molecular Orbital

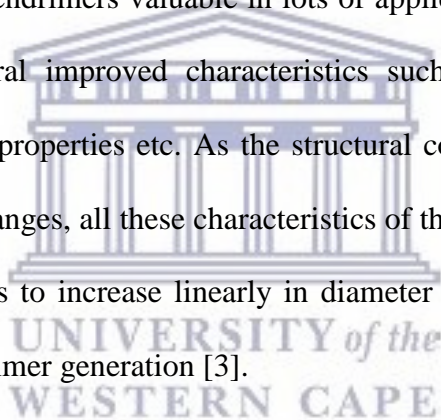


UNIVERSITY *of the*
WESTERN CAPE

CHAPTER 1: INTRODUCTION

1.1 Background to the study

The scientific debates highlighted the term dendrimer as a Greek word in which Dendron means tree while meros means part and additionally the dendrimers might also be called cascade molecule which is not well recognized like dendrimers. Dendrimers are almost mono-dispersed macromolecules that have symmetric branching units (peripheral end groups) building around a linear polymer or small molecular core [1], [2]. Dendrimers are hyper-branched macromolecules with a carefully modified structural designed with peripheral end groups. Functionalizing their peripheral end groups makes dendrimers valuable in lots of applications. Dendrimers consisting of hetero-atoms provide several improved characteristics such as high flexibility, variable branching multiplicity, optical properties etc. As the structural configuration, well-defined size and shape of the dendrimers changes, all these characteristics of the dendrimers mentioned above also changes. Dendrimers tends to increase linearly in diameter and approve a more spherical shape with an increase in dendrimer generation [3].



There has been increasing attention during the past few decades in the semi-conducting copper based chalcogenides NPs because of their broad range of applications in different fields of research. They are mostly used as p-type semiconductors due to the availability of copper vacancies. Copper vacancies also give copper chalcogenides a composition-dependent localized surface plasmon resonance (LSPR) in the near infrared region [4]. Copper based chalcogenides NPs have several applications in different devices such as photovoltaics cells, light emitting diodes, etc. Mostly used copper based chalcogenides is copper telluride (CuTe) [5]. Studies showed that CuTe exists in different non-stoichiometric (Cu_{2-x}Te) and stoichiometric (CuTe,

Cu₂Te, Cu₃Te₄, Cu₄Te, Cu₇Te₅, and Cu₇Te₄) compositions with different crystal structure which helps to adjust their different properties by changing the Cu:Te ratio[6]. Therefore, a broad range of structural variety of transitional metals is taking place due to the incompletely filled d-orbital which permit them to take on many oxidation states [4].

The optical properties of copper-chalcogenides NPs have been widely studied [6], [7]. It is important to note that a lot of disadvantages associated with optical properties have been directed to copper-chalcogenides NPs. However, when comparing the optical properties of copper-chalcogenides NPs to those of organic materials, the optical properties of copper-chalcogenides NPs have numerous advantages that have allowed them to be widely used in different fields of science and technology. Their advantages over organic materials are tuneable-size photoluminescence emission (there is a known correlation between the size of the NPs and its emission wavelength), strong absorption of light, narrow emission bands, broad absorption spectra, highly resistance to photo-degradation and excellent fluorescence brightness [8], [9].

Polymers have been widely used in OPVs devices. The OPVs devices have exceeded 10% power conversion efficiency [10]. Still, the optical band gap of the organic materials is usually greater than 2 eV which covers the visible range wavelength from 300 nm to 650 nm. One crucial requirement in photovoltaic energy conversion is the collection of as much sun radiation as possible [11]. Smaller optical energy band gap of organic materials is needed to extend absorption to longer wavelength region to take benefit of the high flux, red light and near infrared of the solar spectrum. Therefore, it has been a major work to develop novel polymers with a narrow optical band gaps recently [12]. Recent studies showed that the optical properties of organic materials can be improved by blending them with inorganic materials [14].

In this study, we report the synthesis of CuTe@PPI and CuSb@PPI core-shell NPs. The presence of the shell material on the surface of metallic NPs was reported that it improves the optical properties of metallic NPs [9]. To the greatest of our knowledge, CuTe@PPI and CuSb@PPI are novel. The method used to synthesize core-shell NPs was reported by Kumar et al. to synthesize metal chalcogenides but without the presence of the capping agent [13]. In this study, we employ similar method but in the presence of a capping agent. The synthesized core-shell NPs were blended with commercial Poly[N-9'-heptadecanyl-2,7-carbazole-alt-5,5-(4',7'-di-2-thienyl-2',1',3'-benzothiadiazole)] (PCDTBT) material in order to study optical properties of the mixture for possible application in PVs field. The optical properties of the PCDTBT: Core-shell NPs composites were studied using UV-Vis spectroscopy and PL spectroscopy.

1.2 Aim and Objectives

The aim of this study is to come up with novel core-shell nanoparticles and blend them with PCDTBT to study their photophysics properties.

1.2.1 Objectives

1.2.1.1 Synthesis of CuTe NPs and CuSb NPs, characterize with UV-Vis spectroscopy, XRD, TEM, SEM, CV and SWV.

1.2.1.2 Synthesis of 5-(2-thienyl)salicylaldehyde and characterize with NMR, UV-Vis spectroscopy, FTIR spectroscopy, CV and SWV.

1.2.1.3 Synthesis of polypropyleniminetetra(5-(2-thienyl)salicylaldehyde) (PPI) and characterize with NMR, UV-Vis Spectroscopy, FTIR Spectroscopy, XRD, TEM, SEM, EDX, CV and SWV.

1.2.1.4 Synthesis of CuTe@PPI and CuSb@PPI core-shell nanoparticles UV-Vis Spectroscopy, PL Spectroscopy, FTIR Spectroscopy, XRD, TEM, SEM, EDX, CV and SWV.

1.2.1.5 Blending of synthesized CuTe@PPI and CuSb@PPI core-shell nanoparticles with PCDTBT as possible active layer in photovoltaic cells and characterize the composites with UV-Vis Spectroscopy and PL Spectroscopy.

1.3 References

1. E. Abbasi, S. F. Aval, A. Akbarzadeh, M. Milani, and H. T. Nasrabadi, "Dendrimers : Synthesis , applications , and properties," *Nanoscale. Res. Lett.*, vol. 9, pp. 1–10, 2014.
2. V. Viswanath, and K. Santhakumar, "Perspectives on dendritic architectures and their biological applications: From core to cell," *J. Photochem. Photobiol. B.*, vol. 172, pp. 61-83, 2017.
3. X. H. Dai, W. H. Yang, W. L. Yan, J. M. Hu, Y. R. Dai, J. M. Pan, and Y. S. Yan, "Porphyrin-cored dendrimers consisting of novel siloxane-poly(amido amine) dendron-like arms: Synthesis, characterization, and photophysical properties," *Colloids. Surf. A Physicochem. Eng. Asp.*, vol. 520, pp. 222-230, 2017.
4. D. Cadavid, A. Shavel, R. A. Alvarez-puebla, W. J. Parak, J. Arbiol, and A. Cabot, "CuTe nanocrystals: shape and size control, plasmonic properties, and use as SERS probes and photothermal agents," *J. Am. Chem. Soc.*, vol. 135, pp. 7098-7101, 2013.
5. H. M. Pathana, C. D. Lokhande, D. P. Amalnerkar, and T. Seth, "Preparation and characterization of copper telluride thin films by modified chemical bath deposition (M-CBD) method," *Appl. Surf. Sci.*, vol. 218, pp. 291-297, 2003.
6. P. V. Bhuvaneshwari, K. Ramamurthi, and R. Ramesh Babu, "Influence of substrate temperature on the structural, morphological, optical and electrical properties of copper telluride thin films prepared by electron beam evaporation method," *Thin. Solid. Films.*, vol. 632, pp.44-49, 2017.

7. P. Peranantham Y.L. Jeyachandran, C. Viswanathan, N.N. Praveena, P.C. Chitra, D. Mangalaraj, and K. Narayandass, "The effect of annealing on vacuum-evaporated copper selenide and indium telluride thin films," *Mater. Charact.*, vol. 58, pp. 756–764, 2007.
8. H. M. E. Azzazy, M. M. H. Mansour, and S. C. Kazmierczak, "From diagnostics to therapy : Prospects of quantum dots," *Clin. Biochem.*, vol. 40, pp. 917–927, 2007.
9. O. Adegokea, T. Nyokong, and B.C. Forbesa, "Photophysical properties of a series of alloyed and non-alloyed water-soluble l-cysteine-capped core quantum dots," *J. Alloys. Compd.*, vol. 695, pp. 1354-1361, 2017.
10. D. Hashemi, X. Ma, J. Kim, and J. Kieffer, "Design principles for the energy level tuning in donor / acceptor conjugated polymers," *Mater. Sci.*, pp. 1–29, 2017.
11. A. C. Mayer, S. R. Scully, B. E. Hardin, M. W. Rowell, and M. D. Mcgehee, "Polymer-based solar cells," *Mater. Today.*, vol. 10, pp. 28–33, 2007.
12. B. Kim, X. Ma, C. Chen, Y. Ie, E. W. Coir, H. Hashemi, Y. Aso, P. F. Green, J. Kieffer, and J. Kim, "Energy level modulation of HOMO, LUMO, and band- gap in conjugated polymers for organic photovoltaic applications," *Adv. Funct. Mater.*, vol. 23, pp. 439–445, 2013.
13. p. Kumar, and K. Singh, "Element directed aqueous solution synthesis of copper telluride nanoparticles, characterization, and optical properties." *Cryst. Growth. Des.*, vol. 9, pp. 3089-3094, 2009.
14. L. Tzounis, C. Gravalidis, A. Papamichail, and S. Logothetidis, "Enhancement of P3HT: PCBM photovoltaic shells efficiency incorporating core-shell Au@Ag plasmonic nanoparticles," *Mater. Today.*, vol. 3, pp. 832–839, 2016.

CHAPTER 2

LITERATURE REVIEW: CORE-SHELL MATERIALS AS PHOTOVOLTAIC SYSTEMS

2.1 Abstract

Nanoparticles based photovoltaic energy is attracting a lot of attention as a potential candidate for attaining extreme improvement in photovoltaic energy conversion efficiency and stability. Meanwhile, these nanoparticles can be synthesized in a very cheap fashion, leading to a cost-effective production of photovoltaic cells. Today's photovoltaic cells are not efficient enough and are too costly to fabricate for large-scale generation of electricity. There is an increasing need for more efficient and lightweight photovoltaic cells especially in aerospace and other related industries. Photovoltaic cells can rule the energy sector only if their performances are improved and its cost are also comparable to other sources of energy. Different approaches have been intended to increase the performance of the photovoltaic cells, while application of nanotechnology does help with the photovoltaic cells which are more economical. This paper reviews core-shell nanoparticles and their application in photovoltaic systems in order to increase their performance.

2.2 Introduction

Nanomaterials are known to be the foundation of nanoscience and nanotechnology, are defined as a cluster of ions, atoms or molecules with at least one dimension within the nano-scale range (1 – 100 nanometres). A nano-scale range is an interesting range which bridges the space of bulk materials with continuous energy state and tiny molecules with discrete energy states. Since it is recognized that size and morphologies have a huge influence on the properties of nanomaterials, they display exclusive properties such as catalytic, magnetic, optical, physical, chemical and electronic properties as the size changes which are unlike those of the bulk materials[1].

With the current improvement in nanotechnology, one of the main goals for research is to achieve nanomaterials with advanced properties and multi-functionality in order to improve their performances in different applications. This has brought the attention of research for combining two or more nanomaterials which can display distinct properties[2]. It was found that coating other nanoparticles (NPs) with thin surface layer nanoparticles considerably changes their properties and functionalities, such as thermal stability, dispensability, catalytic activities, chemical reactivity or electronic, magnetic and optical properties. These combined nanomaterials were realized initially in the late 1980s, which were later termed core-shell NPs. This term was well accepted by researchers and their use was extended to different fields of science[3], [4]. Core-shell NPs are a kind of biphasic materials which have inner core material and the outer shell material; both materials are made up of different components. The structure of core-shell NPs is shown in figure 2.1 below. These NPs have been of interest because they can display distinct properties which are arising from the combination of core and shell materials, their design, and their geometry. Because of coating the core with shell material, properties of the core such as oxidation decrease, thermal

stability can be tailored, or reactivity decrease so that the dispensability and stability of the core NPs are improved. Sometimes properties which arise from either shell or core material are different. The properties of core-shell NPs can be changed by changing the core to shell ratio or the constituting materials[2], [3].

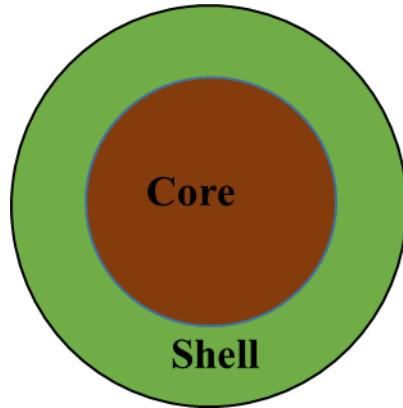


Figure 2. 1: Core-Shell nanoparticles.

Recently, core-shell NPs composed of noble metal nanoparticles mostly gold (Au), silver (Ag), platinum (Pt) and palladium (Pd) have fascinated a lot of attention because of their unique chemical and physical properties such as surface-to-volume ratio, tiny size effect, quantum effect and high surface chemical activity. These noble metal core-shell NPs because of their properties can lead to better performance in various electronics such as optoelectronics, sensors, and also in catalysis[5], [6]. Semiconductors and polymer based core-shell NPs have attracted a great interest as new materials with applications in different electronics such as sensors, organic field effect transistors (OFETs), organic light-emitting diodes (OLEDs) and organic photovoltaics (OPVs) due to their advantages such as easy to fabricate and low cost [7]–[9]. In this study, we review different types of core-shell NPs, environmental impact of photovoltaics (PVs), the methods used to synthesize core-shell NPs, their applications in photovoltaic systems and factor affecting distribution and size of core-shell NPs.

2.3 Environmental impact

The uses of fossil fuels for power generation have produced serious negative consequences in the environment such as air pollution, climate change, acid rain, and global warming. These consequences result to a negative impact on the life of living things. PVs are silent, produces clean energy, maintainable, abundant, renewable, and naturally safer than other traditional systems used for generation of electricity. PVs energy can solve many problems in the environment which are caused by the fossil fuels [10].

2.3.1 Emissions reduction

PVs technology is an emission-free technology; therefore, have a minor effect on the greenhouse gas emissions. During the operation of the PV system, gasses such as nitrogen oxides (NO_x), Sulfur dioxide (SO₂) and carbon dioxide (CO₂) are not released and the system does not contribute to global warming. PVs technology can save 0.53 Kg emission of CO₂ for each kilowatt-hour (kWh) of electricity generated. Table 2.1 below shows the average emission rates of gasses and table 2.2 shows the reduction of emissions of gasses such as NO_x, CO₂ and SO₂ due to the use of PV technology[11]. There are two different sets of emission rates in use: (i) EPA from eGRID 2000 database and (ii) calculations made by ECONorthwest using best accurate eGRID data available[11], [12].

Source	Coal			Natural gas		
	CO ₂ (kg/MW)	NO _x (kg/MWh)	SO ₂ (kg/MWh)	CO ₂ (kg/MWh)	NO _x (kg/MWh)	SO ₂ (kg/MWh)
EPA	515.29	77.18	0.05	1021.05	2.72	5.90
ECONorthwest	530.73	0.31	0.01	982.46	1.59	4.68

Table 2. 1: Average emission rates in Kilograms per Megawatt-hour (Kg/MWh) [11].

Probability	Total Photovoltaic capacity	Coal			Natural gas		
	Capacity (Giga Watts)	CO ₂ (Gg/year)	NO _x (Gg/year)	SO ₂ (Gg/year)	CO ₂ (Gg/year)	NO _x (Gg/year)	SO ₂ (Gg/year)
2030 minimum	70	26,495	42.85	126.11	42,938	25.34	0.55
2030 maximum	100	38,539	62.33	183.43	62,456	36.86	0.80

Table 2. 2: The possible reduction of NO_x, CO₂, and SO₂ via the use of PV technology by 2030 in Gigagram/year (Gg/year) [11].

In summary, PV technology provides significant environmental benefits when compared to other energy sources due to its ability to reduce emissions of harmful gasses. Because of this ability, most serious diseases such as Asthma, heart attacks, cardiovascular problems, and others will be minimized due to the reduction of harmful gasses emission. Production of the PV system has a negative impact on the environment. Some of the toxic substances employed during the production of the system are produced as by-products. Particularly, the PV cell batteries present a danger on the natural resources by containing heavy metals such as cadmium while having a short lifespan. Emissions associated with transportation after fabrication of the systems are insignificant when compared with production emissions[13].

2.4 Types of Core-Shell nanoparticles

There are different classes of core-shell NPs available with a broad array of applications. Mostly, the classification of available core-shell NPs is a difficult duty. In this review, we categorize the core-shell NPs depending on the types of materials used during their synthesis

and the number of their layers. It is clear that the core or shell materials of core-shell NPs are either chalcogens, organic or inorganic materials. Depending on the properties of materials and number of layers, core-shell NPs are categorized into six different groups:

2.4.1 Organic-organic Core-Shell NPs

In Organic-organic core-shell NPs, core and shell materials are both made up of polymers or any other organic materials. Materials of core and shell are different from each other. Organic-organic core-shell NPs (known as smart particles) have been studied and were found to have a broad range of applications in many fields such as catalysis[14], drug delivery[15] and bio-sensing[16]. The advantages of having this category of core-shell NPs are to adjust the physical properties such as toughness[17] or glass transition temperature (T_g) [18], [19] of the whole NPs. T_g is a very important property of organic materials (polymers) because below this temperature, polymers change to a glassy state. While above T_g the polymers change to an elastic material (rubbery state) from a glassy state. As the mechanical properties of the organic-organic core-shell NPs change, their applications also change. For example, coating a polymer with a polymer of different T_g was employed to modify latex based waterborne paints which were the work done by Overbeek. A shell material with low T_g improves the ability to form films, while a core material with high T_g has an impact on adjusting mechanical stability [20].

Mostly, poly (N-isopropyl acrylamide) (PNIPAM) or related polymers are used as major components in organic-organic core-shell NPs because of their thermo-responsive properties. PNIPAM present a lower critical solution temperature in aqueous media at about 32°C and its size decreases drastically upon heating in aqueous solution [21]. Below the lower critical solution temperature, the polymers are easily soluble in water because of bonds formation between the amide side chains and water molecules, while above the lower critical solution temperature, the polymer undergoes volume transition phase. PNIPAM can be used either as

a core or shell in a core-shell NPs synthesis [22]. Richtering *et al.* [23] investigated the rheological properties of core-shell latex using poly (styrene) as a core (with 84 nm in diameter) and temperature responsive PNIPAM as a shell using emulsion polymerization method. They also studied temperature responsive PNIPAM as a function of temperature and concentration. They found that the rheological properties of core-shell latex can be controlled by temperature and are stable against flocculation even at higher temperatures. Also found that thickness of the shell decreases with temperature, which gives rise to a noticeable dependence modulus, shear viscosity, and yield stress on temperature. Xiao *et al.* [24] have prepared mono-dispersed thermo-responsive core-shell polymeric hydrogels (with a mean diameter of 200 nm to 400 nm) with poly(N-isopropyl acrylamide-co-styrene) as core and PNIPAM as shell using seed polymerization method and studied their particle size, morphology and mono-dispersity, and thermo-responsive characteristics experimentally. They found that mean diameter increases, mono-dispersity improves and thermo-responsive increases with an increase in the poly (N-isopropyl acrylamide-co-styrene) dosage.

2.4.2 Organic-inorganic Core-Shell NPs

Organic-inorganic core-shell NPs can be generally defined as nano-composites with organic components such as polystyrene, poly(ethylene oxide), polyurethane, poly(vinyl benzyl chloride), poly(vinylpyrrolidone), etc. as core materials and inorganic components such as metals, metal oxides, metal chalcogenides, or silica as shell material [16]. Organic-inorganic core-shell NPs are widely studied and have been employed in different fields such as delivery system, smart microelectronics, optics, separation devices and functional materials. This category of core-shell NPs contains the double properties of both the organic and inorganic components [25]. It is reported that an organic material coated with the metal oxide is helpful in some aspects such as increasing the strength of the whole material, oxidation resistivity, colloidal and thermal stability. These core-shell NPs also shows the properties of the organic

material such as flexibility, toughness and brilliant optical properties, and also show developed brittleness of the inorganic material [15], [26].

Zho *et al.* [27] have investigated the optical and mechanical properties of their synthesized Acrylic-based polyurethane/nano-silica particles. Their results showed that as the content of nano-silica increases, Young's modulus and tensile strength of the NPs are enhanced. The ultraviolet absorbance in the wavelength between 290 nm and 400 nm improves as the content of nano-silica dioxide increases. After coating polyurethane with silica, only abrasion resistance, and hardness increases.

Khadem *et al.* [28] have studied the properties of optically active poly (amide–imide)/alumina nano-composites with different amounts of alumina NPs. They found that their nano-composites an improved heat stability as compared to a pure polymer which was confirmed by thermal gravimetric analysis. They employed TEM and FESEM which showed a good dispersion of alumina in poly (amide–imide) at nano-scale. Polymers coated with noble metals such as silver and gold were found to have an increased immobilization characteristic of proteins. Therefore, these NPs can be used in different field of immune-sensing, biomedical and biotechnology applications.

2.4.3 Inorganic-organic Core-Shell NPs

These NPs are made up of metal, a metallic compound, metal oxide or silica as a core material with a polymer or any other organic material as a shell. The advantages of coating inorganic material with organic is to increases the oxidation stability of the metal core because the surface atoms of the metal core can be easily oxidized to metal oxide in a room temperature environment and also shows an improvement in biocompatibility for bio-applications [29]. Inorganic-organic core –shell NPs have a wide range of applications, such as optoelectronics and magneto-optic [30], catalysis, coatings, and biomedical applications [31], [32].

Stöver *et al.* [33] reported on metallic iron as core and polymeric dispersant consisting of polyisobutylene, polystyrene or polyethylene chains functionalized with tetraethylenepentamine as a shell for magnetic properties application. They found that the NPs show magnetic properties at room temperature going from super-paramagnetic to ferromagnetic and also found that the saturation magnetization depends on the diameter of the core material.

2.4.4 Inorganic-inorganic Core-Shell NPs

This category is of the most widely used than all other different classes of core-shell NPs. These types of NPs are mostly used for development of semiconductor efficiency, optoelectronics, optical biological imaging and biological labelling, etc. They are various types of inorganic-inorganic core-shell NPs in which both cores and shells consist of metal, metal oxide, silica or other inorganic compounds. Depending on the materials of the shells, the inorganic-inorganic core-shell can be classified as either silica-containing or non-silica core-shell NPs.

2.4.4.1 Inorganic-inorganic (Silica) Core-Shell NPs.

Coating inorganic NPs such as metals, metal oxides, metal salts and binary composites, with silica, have several advantages such as reduction of bulk conductivity, give rise to an increase in suspension stability of core particles and can also be used to adjust the intensity of the surface plasmon absorbance band because silica is optically transparent, allowing the spectroscopic studies of chemical reactions at the core surface. Also, silica is largely chemically inert material; it can cover the core surface without disturbing redox reaction at the core surface [4]. Researchers have studied metals such as gold, silver, metal oxides and binary metal composites coated with silica.

Kobayashi *et al.* [34] worked on colloid solution silica coated gold NPs which were used for X-ray imaging of mouse. Silica was deposited onto the gold NPs via a sol-gel method which

produced silica-coated gold nanoparticles with diameter of 136.4 nm. They reported that the mouse tissues can be imaged by injection of the silica-coated gold nanoparticles colloidal solution into them.

Hu *et al.* [35] studied the optical and structural properties of silica-coated zinc oxide nanoparticle which were synthesized by radio frequency magnetron sputtering method and other NPs treated by a rapid thermal annealing process at various temperatures ranging from 400 °C to 800 °C. Structural and optical properties were studied by X-ray and photoluminescence respectively. Their results show an improved Ultra-violet (UV) emission from the NPs annealed at 600 °C which is caused by the improved quality of silica-coated zinc oxide NPs due to the effective relaxation of residual compression stress and reaching maximum grain size.

From the literature, the thickness of the silica shell material depends strongly on the concentration of the reactants, coating time and other precursors, which enable the shell to be controlled in the region of tens to several hundred nanometers [36]. The spectroscopic analysis of core-shell NPs shows that, as the silica shell thickness increases, the intensity of the UV absorbance increases and the reflectance move to longer wavelength region. This has been shown further in order to control uniformity thickness of the silica-coated silver NPs by Ung *et al.* [37].

2.4.4.2 Inorganic-inorganic (Non-silica) Core-Shell NPs

Except for silica, different inorganic materials such as metals and metal oxide can be employed as shell materials. Many researchers have done their work on core-shell NPs using gold as a shell material. Gold coated on any other particles improves their physical properties such as chemical stability by shielding the core from corrosion and oxidation, biocompatibility and optical properties [38]–[41]. The surface-enhanced Raman scattering

(SERS) of silver-coated gold NPs is more powerful than gold coated silver NPs, showing that the SERS does depend on the core materials [42].

Samal *et al.* [43] demonstrated a method for synthesis of size-controlled silver-coated gold NPs capped with citrate and studied the SERS properties of synthesized NPs. They found that with their method, NPs with size ranging from 30 nm to 300 nm can be obtained by simply varying the core size or controlling shell thickness. The SERS properties of their NPs were studied at three different excitation wavelengths and it was found that the SERS efficiency increases as the size of the NPs increases, irrespective of the laser lines.

2.4.5 Core-multiple shells NPs

In this category, the core material is coated with more than one shell materials. Hong *et al.* [44] came up with a synthetic way to control a number of shells and inter-shell distance. They studied their optical properties as a number of shells increases. They used gold nano-disk as a core and silver NPs as shells. They studied the effect of gold nano-disk core by synthesizing the multiple shells NPs with and without core and found out that the controllability and uniformity of the gold nano-disk core-shell NPs depend strongly on the core. They reported that this method makes it possible to synthesize more complicated nanostructures.

Wang *et al.* [45] used a sol-gel method to synthesize magnetic Fe₃O₄-SiO₂-TiO₂ composites with core-multiple shells structure and investigated their photo-degradation properties of methylene blue under ultra-violet light irradiation at different pH values with dihydrogen peroxide and without it. They found that the photo-degradation ability can get up to 60% after 5 min under UV irradiation in the presence of H₂O₂. They used acetic acid as model organic acid during the demonstration of photo-catalytic activity of FeO₂-SiO₂-TiO₂ and TiO₂. The results showed that carbon dioxide evolution is proportional to the irradiation time, but the yield rate of pure TiO₂ was found to be lower than that of FeO₂-SiO₂-TiO₂.

2.4.6 Chalcogenides-type core-shell NPs

Chalcogenides NPs are materials which show potential for a wide range of applications such as optoelectronics [46], catalysis [47], [48], etc. due to their interesting optical, electrical and chemical properties. They have been studied recently because of their properties such as reduced thermal conductivity as compared to bulk material properties. Chalcogenides hybrid or Nano-alloys combined with more than one chemically different chalcogenides phases are attractive because they provide new properties and increase the functionality of the material [49], [50]. The well-controlled thickness of the chalcogenides layers is very important to the performance of the device. For example, a thick layer of chalcogenides used on CCD array to successfully increases the absorption path length, thus improving the sensitivity of the detector [51].

Malik *et al.* [52] reported synthesis of CdSe/CdS, CdSe/ZnS, and CdSe/ZnSe chalcogenides core-shell NPs and CdSe/CdS nano-alloy using bis (hexyl (methyl) dithiols-/diselenocarbamate) cadmium- (II)/zinc (II) compounds as a single source precursors. They studied their optical properties and compared them to the once of CdSe alloys. The absorption spectra and an emission maximum of core-shell NPs display an increase and a red shift as compared to the parent CdSe NPs.

2.5 Synthesis of Core-Shell nanoparticles

Core-shell NPs are mostly synthesized by more than one steps, firstly synthesis of the core material then synthesis of the shell material on the surface of core material using different methods depending on the types of core and shell materials [53]. Synthesis method of core-shell nanoparticles can be classified in two ways depending on the core particles: (I) core particles can be incorporated into a system modified for selective coating with the shell material, this is advantageous because the core materials are available in pure form, (ii) synthesis of core particles and followed by coating with a shell material in the same reaction

system, the disadvantage of the method is that impurities can be trapped between the core and shell particles. During synthesis of core-shell NPs, proper control of uniform coating and thickness of the shell is difficult. The stabilizer can modify the selectivity and charge on the surface of the core particles [54].

2.5.1 Layer-by-layer deposition

Layer-by-layer deposition (LbL) is a method which can be used to synthesize core-shell NPs via electrostatic interaction (or covalent bonding, hydrogen bonding, Van der Waals) between oppositely charged materials to bring multiple layers together. Modified particles with suitable charges are used as a core and oppositely charged materials are built up onto the core particles. The core particles should be synthesized first in order to use this method [55], [56].

Chen *et al.* [57] report an approach to produce custom-shape capsules by employing hydrogel templates which are achieved by stop flow lithography. Hydrogel templates were coated with a single layer of poly-L-lysine (polyelectrolyte) to achieve core-shell structure. They showed control of shell thickness by tuning parameters such as ionic strength, pH, and pre-polymer composition. This approach is distinctive to other capsules formed by LbL because in their method only one is deposited onto the core as polyelectrolyte and shell which makes this method advantageous with eliminated much time costing coating and rinsing steps. These capsules are useful in therapeutic applications. Koktysh *et al.* [58] used LbL to produce Ag@TiO₂ via the one-pot route. Reduction of Ag⁺ to Ag and under controlled polymerization of TiO₂ onto the Ag core surface occurs simultaneously. The NPs are organized in a closely packed arrangement interlaced by polyelectrolyte generating core-shell material with distinct structure, catalytic, and electron transport properties.

2.5.2 Chemical reduction

Metallic core or shell NPs can be synthesized by reduction of metals salts. The metal salts are dissolved in appropriate synthesis media in the presence of reducing agents and capping

agents such as polymeric ligand, citrates, alkyl thiols, etc. The NPs size average and size distribution can be achieved by changing the synthesis conditions (temperature, reaction time, solvent, reducing agent, capping agent). Chemical reduction happens by simultaneous reduction of metal salts [59], [60]. Studies showed that strong reducing agents like borohydrides results to small particles, while weaker reducing agents such as citrate results to slow rate of reduction and gives larger particles. It is important to use capping agents to stabilize NPs by binding onto or being adsorbed on the surface of NPs to ignore agglomeration [61], [62].

2.5.3 Sol-Gel method

This is a process of forming solid materials from small units which are used mostly in synthesizing metal oxides through poly-condensation reactions of a molecular precursor in a liquid. The required solid particles are suspended in a liquid to form a sol. The sol is deposited on the substrate by coating, spinning or dipping. The sol particles are polymerized by addition of an inhibitor or restricted evaporation of a solvent to give a gel which is heated to give a final solid product.

Mirzaei *et al.* [63] used a two-step reduction-sol gel approach to synthesize highly sensitive Ag@ α -Fe₂O₃ nano-composite for sensing ethanol. They prepared the iron sol by using iron (III) sulfate as an iron source, citric acid as the chelating agent, and polyethylene glycol as esterification agent. Sol was added dropwise to the silver colloids and the mixture was stirred for 15 min. After the mixture was refluxed at 120 °C for 2 h under stirring and the core-shell nanocomposite was prepared with a silver core of 20 nm in diameter covered by a Fe₂O₃ shell with a thickness of 20 nm.

2.5.4 Electrochemical synthesis

Electrochemical synthesis is a method that is used to synthesize NPs in an electrochemical cell. This method is a solution based method with ambient conditions that makes it practical

and inexpensive. It is already used in painting vehicles bodies, showing that is applicable in industrial level. This method can produce different types of materials using almost all semiconductors (chalcogenides, metals, alloys, oxides, etc.). Its solution based environment allows controlling of various synthetic parameters such as temperature, solvents, pH, etc. which turn to have an effect on morphologies. During electrochemical synthesis, deposition current and potential can be employed as other parameters to control nucleation and growth rate of desired NPs. Materials grow directly on the surface of working electrode and the film thickness can be controlled by monitoring the charge passed to persuade electrochemical reactions [64]. Chumming *et al.* [65] synthesized Fe₃O₄-Prussian blue core-shell nanoparticles in situ on a glassy carbon electrode modified with nano-Fe₃O₄ by CV. The properties of synthesized core-shell nanoparticles were determined by electrochemical impedance spectroscopy, CV, and superconducting quantum interference device.

2.6 Factors affecting the distribution and size of Core-Shell nanoparticles

Distribution and particle size are critical parameters in the synthesis of NPs and their applications. The NPs properties depend on the size of the NPs, therefore, their properties changes as the size changes. At a certain range, NPs have better properties. For example, magnetic nanoparticles below 50 nm can be used for in vivo applications such as magnetic resonance imaging, but above 50 nm cannot be used for in vivo applications because they are not easily transported by blood and the particles turn to coagulate within the cell. For a specific application, NPs with large size distribution are unacceptable. Particles size, size distribution and less ability to agglomerate are crucial factors to consider. These factors can be easily controlled by parameters such as the concentration of reactants, temperature, pH and concentration of surface modifier.

2.6.1 Effect of the concentration of reactants

The concentration of reactants is a vital parameter for monitoring the core size or shell thickness. The size of the NPs increases as the concentration of the reactants increases. The size of the NPs is mostly affected by two factors (i) reaction among reactants to form nuclei (nucleation), (ii) particle growth and agglomeration. Nucleation may be taken as a reaction step which is followed by growth. Nucleation is a fast step. The final size of the NPs depends on the growth process if the rate of reaction is high. The rate of reaction increases with the concentration of reactant [66]. At low concentration of reactant, less number of nuclei will be formed because of a slow rate of reaction. The particles formed later will collide with the nuclei that have been formed instead of starting new nuclei, lead to particles with a larger size. At high concentration of the reactant, a large number of nuclei will be formed because a rate of reaction is increased which lead to particles with small size [67]. Shell material mostly formed on the core material through heterogeneous nucleation. The shell material is deposited on the surface of a core material via continuous formation of nuclei and growth on the surface of the core. The slow rate of reaction is more favoured for the synthesis of core-shell NPs than the fast rate of reaction because the shell thickness decreases with decreasing concentration of the reactants [67].

2.6.2 Effect of temperature

Temperature is another factor that can affect the distribution and size of core-shell NPs by controlling the reaction kinetics for the formation of NPs. The particles size depends on the rate of reaction of nucleation which depends on the type of reaction (either endothermic or exothermic), growth which depends on the type of reaction and diffusion of atoms (directly proportional to temperature) [68], and finally agglomeration [69]. The size of NPs increases with an increase in synthesis temperature [70]. Sampaio da Silva *et al.* [71] synthesized Fe₃O₄ NPs as core coated with a mixture of poly(vinylpyrrolidone) and polyethylene glycol as the

shell at different temperatures. The evaluation of the effect temperature on particle size was done using granulometry analyses. Their studies showed that temperature participates in nucleation and growth steps, and the size distribution of the NPs.

2.6.3 Effect of pH

The pH of the precursor solution plays a crucial role in controlling the size of the particles during the synthesis process. A pH controls the size of the particle by controlling the super-saturation which has a maximum value at a certain pH value. At an optimal pH value, where super-saturation has its maximum value, the radius of the particles formed will be small because of the super-saturation (high concentration of solute) which leads to the generation of a large number of nuclei. Kohli *et al.* [72] and Goh *et al.* [73] studied the effect of pH on the size of particles, they found small particles at pH 9 and pH 10 respectively.

2.6.4 Effect of the concentration of surface modifier

The concentration of surface modifier also plays a crucial role in size control of core-shell NPs. NPs with a small size can be achieved by preventing the agglomeration ability of the particles. The role of surface modifier is two-fold. At low concentration of the surface modifier, the surface modifier provokes agglomeration because of lowering the energy of the coated surface, so the size of the particles tends to be increased (surface area is reduced). The strength of this factor increases as the concentration of the surface modifier increases with respect to the concentration of the material to be coated. Oppositely, the modified surface becomes inactive, which prevents agglomeration. Since a higher concentration of the Surface modifier allows coating on a large surface, this factor limits the increase in the size of the particles [74]. Ionic surface modifiers adsorb onto the surface of the core material to form a charged layer. Therefore, the shell material with opposite charge can be deposited on the surface of the core material. Surface modifiers adsorb onto the surface of core, then play an important role in the synthesis of core-shell NPs such as size control and increases the driving

force for the formation of the shell layer. An adsorption density of a surface modifier increases with the concentration of a surface modifier until certain limit. Surface modifier can be employed to control the size of the core-shell NPs, but the particle size distribution depends mostly on the charges on the surface of the particles, therefore is achieved for ionic surface modifiers [75], [76].

2.7 Application of core-shell nanoparticles in photovoltaics

Synthetic core-shell NPs have shown a broad range of application in different fields such as in chemistry, material sciences and biomedical sciences because of their developed chemical and physical properties. The properties of core-shell NPs depend on their size and their shape which can be tuned from one material to another. Every time the surface of the core is modified or coated with a thin layer of another material, they show improved properties compared to the unmodified or uncoated particles [9], [77]. Core-shell NPs containing metals such as palladium, gold, and platinum were found to exhibit size induced quantum-size effect (surface effect and electron confinement) because of their major difference in properties as compared to their bulk and can be used in different functional applications such as optoelectronics, catalysis, and sensors [9]. In this review, we focus on application of core – shell NPs in PVs cells.

Kim *et al.* [78] synthesized polystyrene coated gold NPs (Au@PS NPs) which were used in OPVs and OLEDs to improve their long-term stability and efficiencies. The Au@PS NPs were incorporated into PEDOT: PSS film which was located in between the ITO substrate and the active layer in OPVs and emitting layer in OLEDs. The figure 2.2 below shows the architectures of both OPVs and OLEDs.

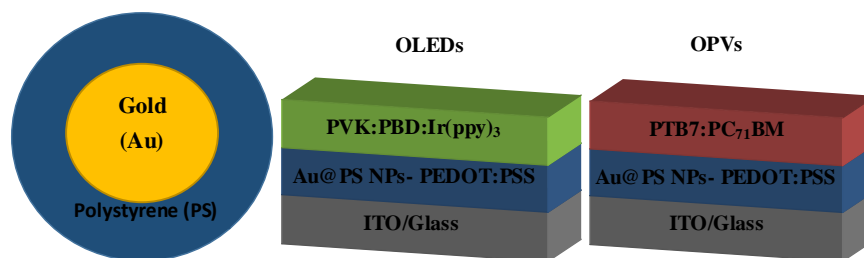


Figure 2. 2: The structure of Au@PS NPs and architectures of both OPVs and OLEDs [78].

The Au@PS NPs incorporation delivered significant improvement in the performance of both OPVs and OLEDs. This improvement benefitted from the plasmonic effect of Au@PS NPs, since these NPs retained the dual function of the plasmonic effect of the gold core and stability, solvent resistance of the polystyrene shell. The table 2.3 below shows the results of efficiencies of OPVs with and without Au@PS NPs. In OPVs, the power conversion efficiency increase from 7.6% (without Au@PS NPs) to 8.4% (with Au@PS NPs). For OLEDs, a green emitting material was employed, the characteristics of OLEDs without and with Au@PS NPs showed an increase in maximum current efficiency which is recorded in table 2.4. Incorporation of Au@PS NPs in PEDOT: PSS layer improves stabilities of OPVs and OLEDs by decreasing the hygroscopic and acidic properties of PEDOT: PSS layer.

Sample	Open-circuit voltage (V)	Short-circuit current density (mA cm ⁻²)	Fill factor (%)	Power conversion efficiency (%)
Without Au@PS NPs	0.75	15.23 ± 0.09	0.67 ± 0.00	7.56±0.02 (7.61)
With polystyrene nanoparticles	0.75	14.68 ± 0.10	0.67 ± 0.01	7.35±0.04 (7.38)
With Au@PS NPs	0.75	16.19 ± 0.03	0.68 ± 0.00	8.27±0.06 (8.36)

Table 2. 3: Characteristics of OPVs without NPs, with PS and with Au@PS NPs in PEDOT: PSS [78].

	Maximum external quantum efficiency (%)	Maximum current efficiency (Cd/A)	Maximum power efficiency (lm/W)
Sample 1: without Au@PS NPs	5.8	20.3	4.5
Sample 3: with Au@PS NPs	7.3	27.0	5.9
Sample 4: with higher number density of Au@PS NPs	7.8	28.9	6.5

Table 2. 4: Characteristics of the Green-Emitting OLEDs device without and with Au@PS NPs [78].

PV cells can be manufactured from the dispersion of core-shell NPs and conducting polymers via spin coating in an active layer [77]. Janković *et al.* [79] demonstrated the incorporation of Au@SiO₂ core-shell NPs into the active layer of OPVs made of two polymers which led to

an increase in photon conversion efficiency. The silica shell layer onto gold NPs provides an electrically insulating surface that prevents interference with the carrier transport and generation inside the active layer. They incorporated Au@SiO₂ core-shell NPs into two different OPVs polymer systems: PBDTT-DPP:PC₆₀BM OPV device and P3HT:PC₆₀BM OPV device. Figure 2.3 below shows the architecture of their OPVs. They found that incorporation of Au@SiO₂ core-shell NPs in PBDTT-DPP:PC₆₀BM and P3HT:PC₆₀BM gave 14.4% and 7.1% improvement as compared to the one without core-shell NPs in photon conversion efficiency respectively. To study the effect of concentration, different concentrations of Au@SiO₂ core-shell NPs were added in active layers. The results showed that as the concentration increases, the photon conversion efficiency also increases until a certain concentration then degrade. In PBDTT-DPP:PC₆₀BM active layer, 0.2 mg/ml of Au@SiO₂ core-shell NPs were found to be optimal concentrations and P3HT:PC₆₀BM active layer, 0.6 mg/ml of Au@SiO₂ core-shell NPs were found to be optimal concentrations. Figure 2.4 below shows the results of the performance of the device containing Au@SiO₂ core-shell NPs in the active layer. Their results indicate that performance of OPVs is sensitive to Au@SiO₂ core-shell NPs concentration as they are incorporated into an active layer.

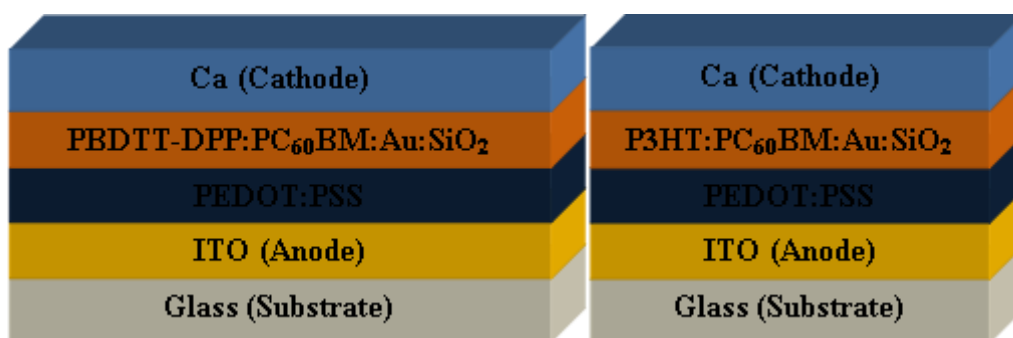


Figure 2. 3: The architecture of OPV cell [79].

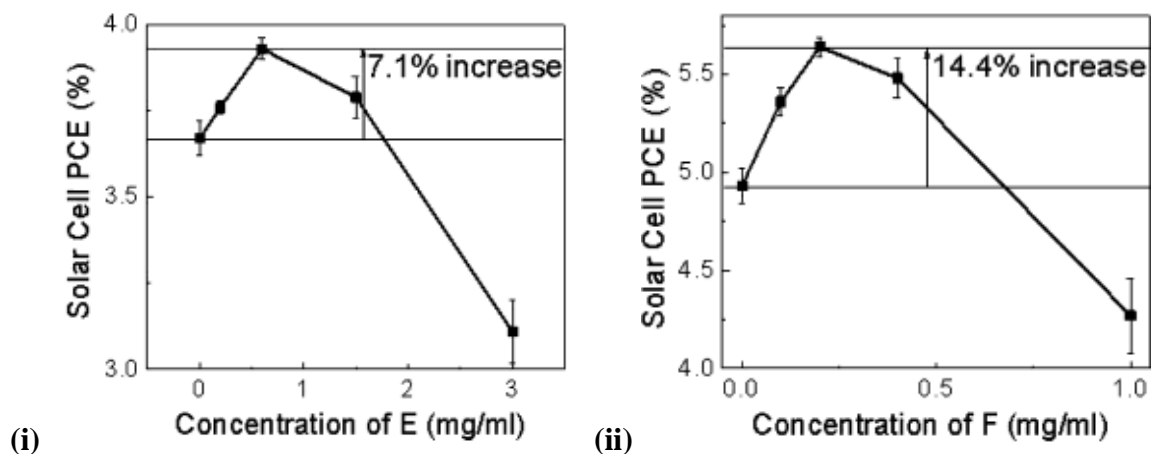


Figure 2.4: Solar cell power conversion efficiency (PCE) as a function of Au@SiO₂ core-shell NPs concentrations (i) P3HT:PC₆₀BM device with Au@SiO₂ core-shell NPs and (ii) PBDTT-DPP: PC₆₀BM Au@SiO₂ core-shell NPs [79].

Jaramillo *et al.* [80] did the same study by incorporating Fe₃O₄@ZnO core-shell NPs in a P3HT:PCBM active layer. After incorporation, the performance of the photovoltaic device improved by 25% better as compared to the device with P3HT:PCBM active layer without Fe₃O₄@ZnO core-shell NPs. Tzounis *et al.* [81] reported a simple method for synthesis of gold@silver (Au@Ag) core-shell NPs which showed an outstanding improvement in power conversion efficiency of OPVs. Their devices were consist of ITO/Glass anode, PEDOT:PSS as hole transport layer, an active layer consisting of P3HT:PCBM, Au@Ag plasmonic NPs layer, a Calcium (Ca) as electron transport layer, and an Aluminium (Al) cathode. The architecture of the device is shown below on figure 2.5. Au@Ag core-shell NPs were deposited onto an active layer below the calcium layer which resulted in an improvement in power conversion efficiency. The results of the device performance are shown below in table 2.5.

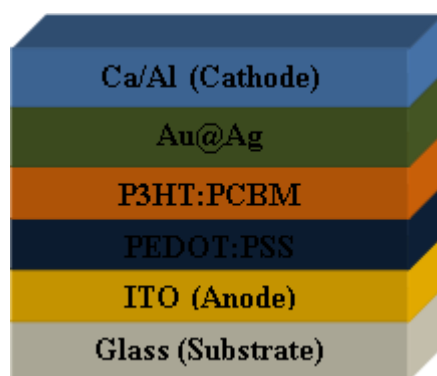


Figure 2. 5: OPV architecture containing Au@Ag core-shell NPs [81].

	Optimizing conditions	Device area (cm ²)	Open-circuit voltage (V)	Short-circuit current density (mA cm ⁻²)	Fill factor (%)	Power conversion efficiency (%)
P3HT: PCBM without Au@Ag Core-Shell nanoparticles	3-5 min at 145 °C	0.045	0.580	7.29	49.25	2.24
P3HT: PCBM with Au@Ag Core-Shell nanoparticles	3-5 min at 145 °C	0.045	0.560	7.99	54.41	2.69

Table 2. 5: Showing electrical characteristics of OPVs device with and without Au@Ag core-shell NPs [81]

2.8 Conclusion

Here, we reviewed the recent progress on core-shell NPs composed of different materials and their applications in the photovoltaic system. The core-shell NPs have been employed in different areas within photovoltaic system. The results from literature indicate that the

introduction of core-shell NPs is beneficial since the performance of the photovoltaic system improves in their presence.

2.9 References

1. X. Liu, Z. Zhong, Y. Tang, and B. Liang, "Review on the synthesis and applications of Fe₃O₄ nanomaterials," *J. Nanomater.*, vol. 2013, pp. 1- 7, 2013.
2. V. V Srdić, B. Mojić, M. Nikolić, and S. Ognjanović, "Recent progress on synthesis of ceramics core/shell nanostructures," *Process. Appli. Ceram.*, vol. 7, pp. 45–62, 2013.
3. A. V Nomove, S. P. Bardakhanov, M. Schreiber, D. G. Bazarova, N. A. Romanov, B. B. Baldanov, B. R. Radnaev, and V. V Syzrantsev, "Structure and mechanism of the formation of core–shell nanoparticles obtained through a one-step gas-phase synthesis by electron beam evaporation," *J. Nanotechnol.*, vol. 6, pp. 874–880, 2015.
4. R. G. Chaudhuri and S. Paria, "Core/shell nanoparticles: classes, properties, synthesis mechanisms, characterization, and applications," *Chem. Rev.*, vol. 112, pp. 2373–2433, 2012.
5. Y. Liu, Y. Ma, J. Zhou, X. Li, S. Xie, and R. Tan, "Synthesis, modification, and biosensing characteristics of Au₂S/AuAgS-coated gold nanorods," *J. Nanomater.*, vol. 2015, pp. 1-8, 2015.
6. Y. Tian, D. Wu, X. Jia, B. Yu, and S. Zhan, "Core-Shell nanostructure of α - Fe₂O₃/Fe₃O₄: synthesis and photocatalysis for methyl orange," *J. Nanotechnol.*, vol. 2011, pp. 1-5, 2011.
7. B. P. Andersson, R. Forchheimer, P. Tehrani, and M. Berggren, "Printable all-organic electrochromic active-matrix displays," *Adv. Funct. Mater.*, vol. 17, pp. 3074–3082, 2007.

8. B. He, W. T. Neo, T. L. Chen, L. M. Klivansky, H. Wang, T. Tan, S. J. Teat, J. Xu, and Y. Liu, "Low bandgap conjugated polymers based on a nature-inspired bay-annulated indigo (BAI) acceptor as stable electrochromic materials," *ACS Sustainable Chem. Eng.*, vol. 4, pp. 2797–2805, 2016.
9. K. S. Kumar, V. B. Kumar, and P. Paik, "Recent advancement in functional core-shell nanoparticles of polymers: Synthesis, physical properties, and applications in medical biotechnology," *J. Nanopart. Res.*, vol. 2013, pp. 1-24, 2013.
10. S. Avril, C. Mansilla, M. Busson, and T. Lemaire, "Photovoltaic energy policy: Financial estimation and performance comparison of the public support in five representative countries," *Energy Policy*, vol. 51, pp. 244–258, 2012.
11. M. Hosenuzzaman, N.A. Rahim, J. Selvaraj, A.B.M.A. Malek, and A. Nahar "Global prospects, progress, policies, and environmental impact of solar photovoltaic power generation," *Renew. Sust. Energ. Rev.*, vol. 41, pp. 284–297, 2015.
12. J. K. O. Brien and G. Forster, "Comparison of air emissions from waste-to-energy facilities to fossil fuel power plants," *14th. North. American. Waste. to. Energy. Conference.*, pp. 69–78, 2006.
13. B. Mahajan and E. Planning, "Energy negative environment impact of solar energy," *Energy Policy.*, pp. 1–5, 2017.
14. A. Lu, D. Moatsou, A. Longbottom, and R. K. O. Reilly, "Tuning the catalytic activity of L-proline functionalized hydrophobic nanogel particles in water," *Chem. Sci.*, vol. 4, pp. 965-969, 2013.
15. W. H. Blackburn and L. A. Lyon, "Size controlled synthesis of monodispersed, core/shell nanogels," *Colloid. Polym. Sci.*, vol. 286, pp. 563–569, 2008.

16. Q. Luo, P. Liu, Y. Guan, and Y. Zhang, "Thermally induced phase transition of glucose-sensitive core-shell microgels," *ACS. Appl. Mater. Interfaces.*, vol. 2, pp. 760-767, 2010.
17. A. Hassan and B. Haworth, "Impact properties of acrylate rubber-modified PVC : Influence of temperature," *J. Mater. Process. Tech.*, vol. 172, pp. 341-345, 2006.
18. I. Berndt, W. Richtering, and D.- Kiel, "Doubly temperature sensitive core-shell microgels," *Macromolecules.*, vol. 36, pp. 8780-8785, 2003.
19. J. Brijitta, B. V. R. Tata, and T. Kaliyappan, "Phase behavior of poly (N-isopropyl acrylamide) nanogel dispersions : Temperature dependent particle Size and interactions," *J. Nanosci. Nanotechnol.*, vol. 9, pp. 5323-5328, 2008.
20. A. Overbeek and A. Overbeek, "Polymer heterogeneity in waterborne coatings Polymer heterogeneity in waterborne coatings," *J. Coat. Technol. Res.*, vol. 7, pp. 1-21, 2009.
21. R. Azlinawati, R. Universiti, and R. A. Ramli, "Core-shell polymers : A review ," *RSC. Adv.*, vol. 3, pp. 15543-15565, 2013.
22. M. Ballauff and Y. Lu, "Smart" nanoparticles :Preparation , characterization and applications," *Polym. J.*, vol. 48, pp. 1815-1823, 2007.
23. H. Senff, W. Richtering, A. Weiss, and M. Ballauff, "Rheology of a temperature sensitive core-shell latex," *Langmuir.*, vol. 15, pp. 102-106, 1999.
24. X. Xiao, L. Chu, W. Chen, S. Wang, and R. Xie, "Preparation of submicrometer-sized monodispersed thermoresponsive core-shell hydrogel microspheres," *Langmuir.*, vol. 34, pp. 5247-5253, 2004.
25. A. K. F. Dyab, H. A. Al-lohedan, H. A. Essawy, A. I. A. A. El-mageed, and F. Taha, "Fabrication of core/shell hybrid organic-inorganic polymer microspheres via

- Pickering emulsion polymerization using laponite nanoparticles,” *J. Saudi. Chem. Soc.*, vol. 18, pp. 610–617, 2014.
26. A. R. Mahdavian, M. Ashjari, and A. B. Makoo, “Preparation of poly (styrene–methyl methacrylate)/SiO₂ composite nanoparticles via emulsion polymerization . An investigation into the compatibilization,” *Eur. polym. j.*, vol. 43, pp. 336–344, 2007.
27. S. Zhou, L. Wua, J. Sun, and W. Shen, “The change of the properties of acrylic-based polyurethane via addition of nano-silica,” *Prog. Org. Coat.*, vol. 45, pp.33-42, 2002.
28. S. Mallakpour and E. Khadem, “A green route for the synthesis of novel optically active poly(amide–imide) nanocomposites containing N-trimellitylimido-L-phenylalanine segments and modified alumina nanoparticles,” *High. Perform. Polym.*, vol. 26, pp. 392–400, 2014.
29. D. J. Bharali, I. Klejbor, E. K. Stachowiak, P. Dutta, I. Roy, N. Kaur, E. J. Bergey, P. N. Prasad, and M. K. Stachowiak, “Organically modified silica nanoparticles : A nonviral vector for in vivo gene delivery and expression in the brain,” *Proc. Natl. Acad. Sci.*, vol. 102, pp. 11539–11544, 2005.
30. S. Li, M. M. Lin, M. S. Toprak, D. K. Kim, and M. Muhammed, “Nanocomposites of polymer and inorganic nanoparticles for optical and magnetic applications,” *Nano. Rev.*, vol. 1, pp. 1–19, 2010.
31. M. A. Hood, M. Mari, and R. Muñ, “Synthetic strategies in the preparation of polymer/inorganic hybrid nanoparticles,” *Materials.*, vol. 7, pp. 4057–4087, 2014.
32. T. Krasia-christoforou, “Organic–inorganic polymer hybrids : Synthetic strategies and applications,” *Springer. Handb. Audit. Res.*, pp. 11–21, 2015.
33. N. A. D. Burke, H. D. H. Sto, and F. P. Dawson, “Magnetic nanocomposites : preparation and characterization of polymer-coated iron nanoparticles,” *Chem. Mater.*, vol 14, pp 4752–4761, 2002.

34. Y. Kobayashi, H. Inose, T. Nakagawa, Y. Kubota, and K. Gonda, "X-ray imaging technique using colloid solution of Au/silica core-shell nanoparticles," *J. Nanostruct. Chem.*, vol. 17, pp. 507-514, 2013.
35. S.Y. Hu, Y.C. Lee, J.W. Lee, J.C. Huang, J.L. Shen, and W. Water, "The structural and optical properties of ZnO/Si thin films by RTA treatments." *Appl. Surf. Sci.*, vol. 254, pp. 1578–1582, 2008.
36. Y. Lu, Y. Yin, Z. Li, and Y. Xia, "Synthesis and self-assembly of Au@SiO₂ core-shell colloids," *Nano Lett.*, vol. 2, pp. 2–5, 2002.
37. T. Ung and L. M. Liz-marza, "Controlled method for silica coating of silver colloids . influence of coating on the rate of chemical reactions," *Langmuir.*, vol. 7463, pp. 3740–3748, 1998.
38. U. Tamer, D. Cetin, Z. Suludere, and I. Hakk, "Gold-coated iron composite nanospheres targeted the detection of escherichia coli," *Int. J. Mol. Sci.*, vol. 14, pp. 6223–6240, 2013.
39. L. Wang, J. Luo, Q. Fan, M. Suzuki, I. S. Suzuki, M. H. Engelhard, Y. Lin, N. Kim, J. Q. Wang, and C. Zhong, "Monodispersed core-shell Fe₃O₄@Au nanoparticles," *J. Phys. Chem. B.*, vol. 109, pp. 21593–21601, 2005.
40. C. Wu and D. Chen, "Spontaneous synthesis of gold nanoparticles on gum arabic-modified iron oxide nanoparticles as a magnetically recoverable nanocatalyst," *Nanoscale. Res. Lett.*, vol. 7, pp. 2–8, 2012.
41. S. Xuan, Y. J. Wang, J. C. Yu, and K. C. Leung, "Preparation , characterization , and catalytic activity of core/shell Fe₃O₄@Polyaniline@Au nanocomposites," *Langmuir.*, vol. 25, pp. 11835–11843, 2009.

42. S. Wojtysiak, M. S. Walczy, and A. Kudelski, "Vibrational Spectroscopy silver-platinum core-shell nanoparticles for surface-enhanced raman spectroscopy," *Vib. Spectro.*, vol. 57, pp. 261–269, 2011.
43. A. K. Samal, L. Polavarapu, S. Rodal-cedeira, L. M. Liz-marza, and I. Pastorizantoss, "Size-tunable Au@Ag core-shell nanoparticles: Synthesis and surface-enhanced raman Ssattering properties," *Langmuir.*, vol. 29, pp. 15076–15082, 2013.
44. S. Hong, H. Y. Jang, and S. Park, "Au nanodisk-core multishell nanoparticles: Synthetic method for controlling number of shells and intershell distance," *Chem. Mater.*, vol. 26, pp. 3618–3623, 2014.
45. R. Wang, X. Wang, X. Xi, R. Hu, and G. Jiang, "Preparation and photocatalytic activity of magnetic Fe₃O₄/SiO₂/TiO₂ composites," *Adv. Mater. Sci. Eng.*, vol. 2012, pp. 1-8, 2012.
46. J. Y. Lee, J. Shin, G. Lee, and C. Lee, "Two-dimensional semiconductor optoelectronics based on van der Waals heterostructures," *J. Nanomater.*, vol. 6, pp. 40–43, 2016.
47. M. Nanocatalysts, T. F. Jaramillo, K. P. Jørgensen, J. Bonde, J. H. Nielsen, S. Horch, and I. Chorkendorff, "Identification of active edge sites for electrochemical H₂ evolution from MoS₂ nanocatalysts," *Science.*, vol. 317, pp. 100–103, 2007.
48. J. D. Benck, T. R. Hellstern, J. Kibsgaard, P. Chakthranont, and T. F. Jaramillo, "Catalyzing the hydrogen evolution reaction (HER) with molybdenum sulfide nanomaterials," *ACS. Catal.*, vol. 4, pp 3957–3971, 2014.
49. M. Han, "Composition-tunable alloyed semiconductor nanocrystals," *Acc. Chem. Res.*, vol. 43, pp. 621–630, 2010.

50. Y. Yang, K. Wang, H. Liang, G. Liu, M. Feng, L. Xu, J. Liu, J. Wang, and S. Yu, "A new generation of alloyed/multimetal chalcogenide nanowires by chemical transformation," *Sci. Adv.*, vol. 1, pp. 1–9, 2015.
51. Y. Zha and C. B. Arnold, "Solution-processing of thick chalcogenide- chalcogenide and metal-chalcogenide structures by spin-coating and multilayer lamination," *Opt. Mater.*, vol. 3, pp. 309–317, 2013.
52. M. A. Malik, P. O. Brien, and N. Revaprasadu, "A simple route to the synthesis of core/shell nanoparticles of chalcogenides," *Chem. Mater.*, vol. 14, pp. 2004–2010, 2002.
53. R. Hayes, A. Ahmeda, T. Edge, and H. Zhanga, "Core–shell particles: Preparation, fundamentals and applications in high performance liquid chromatography." *J. Chromatogr. A.*, vol. 1357, pp 36–52, 2014.
54. H. M. Joshi, M. De, F. Richter, J. He, P. V Prasad, and V. P. Dravid, "Effect of silica shell thickness of Fe₃O₄–SiO_x core–shell nanostructures on MRI contrast," *Contrast. Media. Mol. Imaging.*, vol. 7, pp. 460–468, 2015.
55. G. Schneider and G. Decher, "Functional core/shell nanoparticles via layer-by-layer assembly . investigation of the experimental parameters for controlling particle aggregation and for enhancing dispersion stability," *Langmuir.*, vol. 24, pp. 1778–1789, 2008..
56. A. P. R. Johnston, C. Cortez, A. S. Angelatos, and F. Caruso, "Layer-by-layer engineered capsules and their applications," *Curr. Opin. Colloid. Interface. Sci.*, vol. 11, pp. 203–209, 2006.
57. L. Chen, H. Z. An, and P. S. Doyle, "Synthesis of nonspherical microcapsules through controlled polyelectrolyte coating of hydrogel templates," *Langmuir.*, vol. 31, pp. 9228–9235, 2015.

58. I. Pastoriza-santos, D. S. Koktysh, A. A. Mamedov, M. Giersig, N. A. Kotov, and L. M. Liz-marza, "One-pot synthesis of Ag@TiO₂ core-shell nanoparticles and their layer-by-layer assembly," *Langmuir.*, vol. 16, pp 2731–2735, 2000.
59. B. Khodashenas and H. R. Ghorbani, "Synthesis of silver nanoparticles with different shapes," *Arab. J. Chem.*, 2015.
60. A. Pietro Reverberi, M. Salerno, S. Lauciello, and B. Fabiano, "Synthesis of copper nanoparticles in ethylene glycol by chemical reduction with vanadium (+2) salts," *Materials (Basel).*, vol. 9, pp. 1–11, 2016.
61. A. A. El-kheshen and S. F. G. El-rab, "Effect of reducing and protecting agents on size of silver nanoparticles and their anti-bacterial activity," *Pharm. Lett.*, vol. 4, pp. 53–65, 2012.
62. K. M. M. A. El-nour, A. Al-warthan, and R. A. A. Ammar, "Synthesis and applications of silver nanoparticles," *Arab. J. Chem.*, vol. 3, pp. 135–140, 2010.
63. A. Mirzaei, K. Janghorban, B. Hashemi, A. Bonavita, M. Bonyani, S. G. Leonardi, and G. Neri, "Synthesis, characterization and gas sensing properties of Ag@ α -Fe₂O₃ core-shell nanocomposites," *J. Nanomater.*, vol. 5, pp. 737–749, 2015.
64. D. Kang, T. W. Kim, S. R. Kubota, A. C. Cardiel, H. G. Cha, and K. Choi, "Electrochemical synthesis of photoelectrodes and catalysts for use in solar water splitting," *Chem. Rev.*, vol. 115, pp 12839–12887, 2015.
65. J. Chumming and L. Xiangqin, "Electrochemical synthesis of Fe₃O₄-PB nanoparticles with core-shell structure and its electrocatalytic reduction toward H₂O₂," *J. Solid. State. Chem.*, vol. 13, pp. 1273–1278, 2009.
66. R. G. Chaudhuri and S. Paria, "Synthesis of sulfur nanoparticles in aqueous surfactant solutions," *J. Colloid. Interface. Sci.*, vol. 343, pp. 439–446, 2010.

67. P. Fang, S. Duan, X. Lin, J. R. Anema, J. Li, O. Buriez, and Y. Ding, "Tailoring Au-core Pd-shell Pt-cluster nanoparticles for enhanced electrocatalytic activity," *Chem. Sci.*, vol. 2, pp. 531–539, 2011.
68. A. Abedini, A. R. Daud, M. Azmi, A. Hamid, N. K. Othman, and E. Saion, "A review on radiation-induced nucleation and growth of colloidal metallic nanoparticles," *Nanoscale. Res. Lett.*, vol. 8, no. 1, p. 1, 2013.
69. C. Bantz, O. Koshkina, T. Lang, H. Galla, C. J. Kirkpatrick, R. H. Stauber, and M. Maskos, "The surface properties of nanoparticles determine the agglomeration state and the size of the particles under physiological conditions," *J. Nanotechnol.*, vol. 5, pp. 1774–1786, 2014.
70. D. P. Bisen, R. Sharma, N. Brahme, and R. Tamrakar, "Effect of temperature on the synthesis of CdS: Mn-doped nanoparticles," *Chalcogenide. Lett.*, vol. 6, pp. 427–431, 2009.
71. F. A. Sampaio, E. E. G. Rojas, and M. F. De Campos, "Effect of temperature on the size of Fe₃O₄ nanoparticles coated with PEG/PVP," *Mater. Sci.*, vol. 4, pp. 2518–2524, 2016.
72. N. Kohli, O. Singh, and R. C. Singh "Influence of pH on particle size and sensing response of chemically synthesized chromium oxide nanoparticles to alcohols." *Sens. Actuators. B*, vol 158, pp. 259-264, 2011.
73. K. Wei, G. Mohd, R. Johan, and Y. H. Wong, "Effect of pH variation on the stability and structural properties of In(OH)₃ nanoparticles synthesized by co-precipitation method," *Appl. Phys. A*, vol. 122, pp. 1–9, 2016.
74. T. Prozorov, G. Kataby, R. Prozorov, and A. Gedanken, "Effect of surfactant concentration on the size of coated ferromagnetic nanoparticles," *Thin. Solid. Films.*, vol. 340, pp. 189–193, 1999.

75. N. Saleh and H. Kim, "Ionic strength and composition affect the mobility of in water-saturated sand columns," *Environ. Sci. Technol.*, vol. 42, pp. 3349–3355, 2008.
76. P. K. Sharma, M.H. Jilavi, R. Nass, and H. Schmidt "Tailoring the particle size from μm →nm scale by using a surface modifier and their size effect on the fluorescence properties of europium doped yttria," *J. Lumin.*, vol. 82, pp. 187–193, 1999.
77. E. Arici, D. Meissner, F. Schäffler, and N. S. Sariciftci, "Core/shell nanomaterials in photovoltaics," *Int. J. Photoenergy.*, vol. 5, pp. 199-208, 2003.
78. T. Kim, H. Kang, S. Jeong, D. J. Kang, C. Lee, C. Lee, M. Seo, J. Lee, and B. J. Kim, "Au@Polymer core-shell nanoparticles for simultaneously enhancing efficiency and ambient stability of organic optoelectronic devices," *ACS. Appl. Mater. Interfaces.*, vol. 6, pp. 16956–16965, 2014.
79. V. Jankovi, "Active Layer-Incorporated , Spectrally nanorod-based light trapping for organic photovoltaics," *ACS. Nano.*, vol. 7, pp. 3815–3822, 2013.
80. J. Jaramillo, B. W. Boudouris, A. Barrero, and F. Jaramillo, "Design of superparamagnetic core-shell nanoparticles for enhanced performance of inverted polymer solar cells," *ACS. Appl. Mater. Interfaces.*, vol. 7, pp 25061–25068, 2015.
81. L. Tzounis, C. Gravalidis, A. Papamichail, and S. Logothetidis, "Enhancement of P3HT:PCBM photovoltaic shells efficiency incorporating core-shell Au@Ag plasmonic nanoparticles ," *Mater. Today.*, vol. 3, pp. 832–839, 2016.

CHAPTER 3: ANALYTICAL TECHNIQUES AND EXPERIMENTAL METHODS

This chapter presents the details of experimental methods and materials used when synthesizing CuTe NPs, CuSb NPs, 5(2-thienyl)salicylaldehyde, PPI, CuTe@PPI, CuSb@PPI and the blending of NPs with PCDTBT. Analytical techniques used for characterization of synthesized materials are explained in this chapter.

3.1 Reagents and materials

Copper nanopowder (Cu), copper (II) chloride (CuCl₂), tellurium powder (Te), antimony (III) chloride (SbCl₃), hydrazine monohydrate, ethylene glycol, 5-bromosalicylaldehyde, 2-thienylboronic acid, tetrakis(triphenylphosphine) palladium(0) (Pd(PPh₃)₄), sodium carbonate (Na₂CO₃), 1,2-dimethoxyethane (DME), polypropylenimine tetramine G1 dendrimer (DAB-Am-4), methanol anhydrous, dichloromethane (CH₂Cl₂), anhydrous magnesium sulphate (MgSO₄), deuterated chloroform (CDCl₃), sulphuric acid (H₂SO₄, 98 %), absolute ethanol, potassium bromide (KBr) and poly[*N*-9'-heptadecanyl-2,7-carbazole-*alt*-5,5-(4',7'-di-2-thienyl-2',1',3'-benzothiadiazole)] (PCDTBT) were all purchased from Sigma-Aldrich (Cape Town, South Africa). All chemicals were of analytical reagent grade and were used without any further purification. Deionised water (18.2 MΩ cm) was purified by a Milli-QTM system (Millipore). Analytical grade argon gas was purchased from Afrox Company, South Africa. Alumina polishing pads and powder (0.05 μm, 0.3 μm and 1.0 μm) were obtained from Buehler (Illinois, USA) and were used to polish the glassy carbon electrodes.

3.2 Characterization Techniques

The UV-Vis spectra were recorded using a Nicolet Evolution 100 Spectrometer from Thermo Electron Corporation (UK) and 10 mm cuvettes which holds up to 3.5 mL. All the synthesized materials were dissolved in Chlorobenzene. The UV-Vis absorption spectrum range between 280 nm and 1050 nm was used. FTIR spectra were recorded on a Perkin-Elmer Precisely Spectrum-100 FTIR spectrometer, using Attenuated Total Reflectance. The

samples were mixed with KBr and were milled using mortar and pestle before analysis. The spectra were recorded in the region 4000 cm^{-1} to 400 cm^{-1} . Photoluminescence spectra were carried out using a Horiba Jobin Yvon NanoLog with FluorEssence™ V3 software. Samples were prepared using chlorobenzene as a solvent. The X-Ray Diffraction (XRD) patterns were performed on XRD model Bruker AXS D8 advance with Cu $K\alpha$ radiation ($\lambda = 1.5406\text{ \AA}$). NMR studies were carried out using Bruker High Performance Digital FT-NMR 400 Avance III HD NanoBay Spectrometer using deuterated chloroform as a solvent. For SEM analysis, the Samples were mounted on a carbon tape. Then, the samples were coated with a layer of carbon using EMITECH K950X prior for analysis with 30 KV high resolution Auriga Field Emission Scanning Electron Microscope (FEG SEM) which is equipped with EDS. High Resolution Transmission Electron Microscopy (HRTEM), the sample was dispersed in ethanol. The sample was drop coated on a Nickel grid and allowed to dry prior for analysis. HRTEM studies were carried out using 200 kV Technai G2 F20 S-Twin MAT HRTEM. Energy dispersive analysis by X-ray (EDX) was used to observe the elements that are present in the sample. The electrochemical studies were carried out on a BAS 100W electrochemical workstation from BioAnalytical Systems Incorporation (Lafayette, USA) using a three-electrodes cell system namely: Glassy carbon electrode as working electrode, Platinum wire and Ag/AgCl (saturated NaCl) as counter electrode and reference electrode respectively. A 0.1 M H_2SO_4 was prepared using absolute ethanol and was used as an electrolyte. Working electrode was cleaned using polishing pads and alumina powders. After polishing the working electrode, it was place ethanol then placed in a sonicator for 10 min and ethanol was replaced with water and placed in a sonicator for another 10 min. Further cleaning was done using aqueous 0.1 M H_2SO_4 running 10 cycles at scan rate of 100 mVs^{-1} and potential window from -2000 mV to 2000 mV.

3.3 Synthesis of CuSb and CuTe nanoparticles

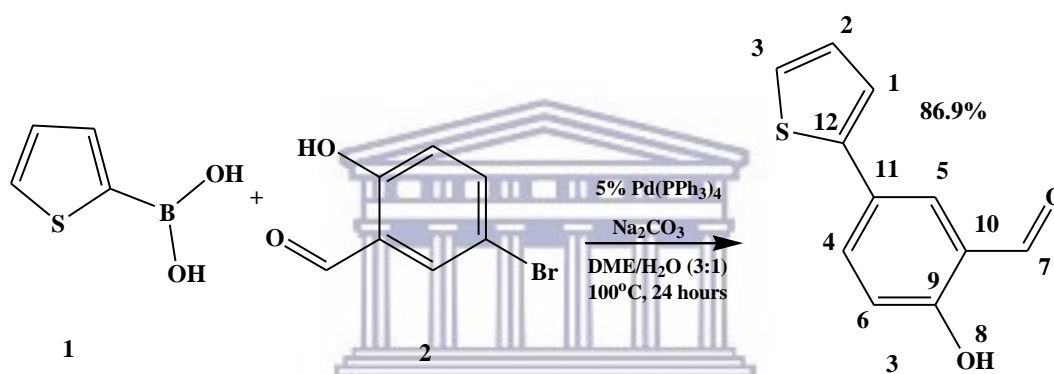
In the synthesis Cu (400 mg, 6.300 mmol) and Te (803 mg, 6.300 mmol) were added in a deionised water, ethylene glycol, and hydrazine hydrate solution with a molar ratio of 7:3:1 respectively in a 50 mL round bottom flask. The mixture was refluxed while stirring vigorously at 75 °C for 24 h. The resulting black precipitates were collected and washed three times with hot water and lastly washed with absolute ethanol three times. After each washing step, the solution was centrifuged for 15 min to separate the product. The precipitates for were dried at 60 °C for overnight. Same procedure was used to synthesize CuSb NPs by adding CuCl₂ (400 mg, 2.980 mmol) and SbCl₂ (679 mg, 2.98 mmol) were added in deionised water, ethylene glycol, and hydrazine hydrate solution with a molar ratio of 7:3:1 respectively in a 50 mL round bottom flask [1].

3.4 Synthesis of 5-(2-thienyl)salicylaldehyde (3)

A 5-(2-thienyl)salicylaldehyde (3) was synthesized by adding 5-bromosalicylaldehyde (2.00 g, 9.940 mmol) (2), 2-thienylboronic acid (1.272 g, 9.940 mmol) (1), 5% mol of Pd (PPh₃)₄ (578 mg, 0.500 mmol), and Na₂CO₃ (1.054 g, 9.940 mmol) into a Schlenk tube. Degassed solution of 1, 2-dimethoxyethane (DME) and water of 3:1 volume ratio (40 mL) was added into the Schlenk tube. Schlenk tube was flushed with argon gas for at least 1 h. The solution was heated at 100°C for 24 h under vigorous stirring. The method is shown schematically on scheme 3.1 below. After 24 h, 15mL of water was added into the solution and the aqueous solution was extracted with CH₂Cl₂. Organic layer was dried over anhydrous MgSO₄ and vacuum filtration was used to remove MgSO₄. Rotary evaporator was used to remove CH₂Cl₂ resulting to a yellow solid product. The product was further purified with preparative thin layer chromatography using CH₂Cl₂: Methanol with a volume ratio of 9:1 resulting to a yellow product (1.7636 g) with percentage yield of 86.9% [2], [3].

$^1\text{H-NMR}$ (400 MHz, CDCl_3): $\delta = 7.0331$ ppm (d, 1H, H-6), $\delta = 7.0891$ ppm (dd, 1H, H-2), $\delta = 7.2477$ ppm (d, 1H, H-1), $\delta = 7.2806$ ppm (d, 1H, H-3), $\delta = 7.7638$ ppm (s, 1H, H-5), $\delta = 7.7859$ ppm (d, 1H, H-4), $\delta = 9.9558$ ppm (s, 1H, H-7), $\delta = 11.0087$ ppm (s, 1H, H-8) (Spectrum shown on chapter 8 figure 8.1).

$^{13}\text{C-NMR}$ (400 MHz, CDCl_3): $\delta = 118.3298$ ppm (C-6), $\delta = 120.6193$ ppm (C-10), $\delta = 122.8941$ ppm (C-1), $\delta = 124.6833$ ppm (C-3), $\delta = 126.9532$ ppm (C-11), $\delta = 128.1742$ ppm (C-3), $\delta = 130.6459$ ppm (C-5), $\delta = 134.6761$ ppm (C-4), $\delta = 142.5374$ ppm (C-12), $\delta = 160.9704$ ppm (C-9), $\delta = 196.5024$ ppm (C-7) (Spectrum shown on chapter 8 figure 8.2).



Scheme 3. 1: Synthesis of 5-(2-thienyl)salicylaldehyde.

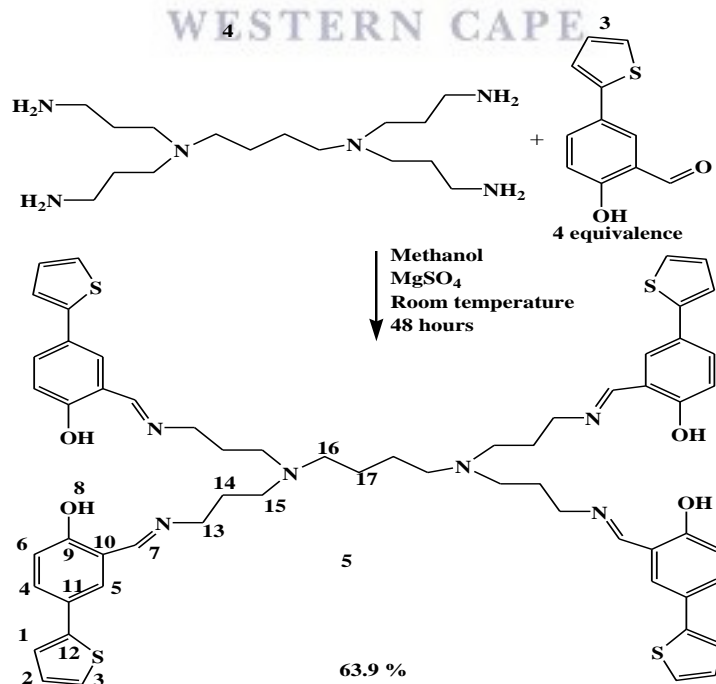
3.5 Synthesis of polypropylenimine tetra(5-(2-thienyl)salicylaldehyde) (PPI) (5)

During synthesis of PPI; anhydrous MgSO_4 (4.00 g, 6.320 mmol) and 5-(2-thienyl)salicylaldehyde (1.290 g, 6.320 mmol) were added into a round bottom flask. Methanol (40 mL) was added into the mixture. Polypropylenimine tetramine G1 dendrimer (4) (500 mg, 1.580 mmol) added drop wise while stirring the mixture and reaction was left to run for 48 h at room temperature. The reaction is shown on the scheme 3.2 below. After 48 h, yellowish methanol was discarded from the product. The yellow product was stacked on the round bottom flask and was removed by addition of CH_2Cl_2 . Vacuum filtration was used to remove anhydrous MgSO_4 . The product was washed three times with deionised water. CH_2Cl_2 was removed using rotary evaporator resulting to an oily dark yellow product. The

product was dried under vacuum for three days resulting to a dark yellow product (1.071 g) with yield percentage of 63.9% [4], [5].

$^1\text{H-NMR}$ (400 MHz, CDCl_3): $\delta = 6.9050$ ppm (d,1H, H-6), $\delta = 7.0282$ ppm (dd,1H, H-2), $\delta = 7.1457$ ppm (d,1H, H-1), $\delta = 7.1915$ ppm (d,1H, H-3), $\delta = 7.4166$ ppm (s, 1H, H-5), $\delta = 7.5176$ ppm (d,1H, H-4), $\delta = 8.3312$ ppm (s, 1H, H-7), $\delta = 13.6349$ ppm (s, 1H, H-8), $\delta = 1.402$ ppm (s, 4H, H-17), $\delta = 2.381$ ppm (s, 4H, H-16), $\delta = 2.491$ ppm (t, 8H, H-15), $\delta = 1.803$ ppm (m, 8H, H-14), $\delta = 3.617$ ppm (t, 8H, H-13) (Spectrum shown on chapter 8 figure 8.3).

$^{13}\text{C-NMR}$ (400 MHz, CDCl_3): $\delta = 117.6826$ ppm (C-6), $\delta = 118.7083$ ppm (C-10), $\delta = 121.9980$ ppm (C-1), $\delta = 123.7607$ ppm (C-3), $\delta = 125.2290$ ppm (C-11), $\delta = 127.9912$ ppm (C-3), $\delta = 128.4788$ ppm (C-5), $\delta = 129.9362$ ppm (C-4), $\delta = 143.8783$ ppm (C-12), $\delta = 161.1953$ ppm (C-9), $\delta = 164.6846$ ppm (C-7), $\delta = 57.2800$ ppm (C-13), $\delta = 51.3385$ ppm (C-14), $\delta = 53.9800$ ppm (C-15), $\delta = 53.4454$ ppm (C-16) $\delta = 28.3857$ ppm (C-17) (Spectrum shown on chapter 8 figure 8.4).



Scheme 3. 2: Synthesis of polypropylenimine tetra(5-(2-thienyl) salicylaldehyde) (PPI).

3.6 Core-Shell NPs were synthesized using two-pots method and one-pot method

3.6.1 Synthesis of Core-Shell Nanoparticles via two-pots method

CuSb NPs (250 mg, 2.053 mmol) and CuTe NPs (250 mg, 1.308 mmol) were added into two different round bottom flasks. A 30 mL ethylene glycol was added into each round bottom flask. The resulting solution was placed in a sonicator for 30 min. After 30 min, 5% molar solution of PPI solution was added in each round bottom flask. The resulting solution was placed in a sonicator for another 30 min. After 30 min, the solution was refluxed at 75 °C for 24 h under vigorous stirring. The resulting precipitates were washed three with absolute ethanol. The products were dried under vacuum at 60 °C for overnight [6].

3.6.2 Synthesis of Core-Shell Nanoparticles via one-pot method

During synthesis; Cu (400mg, 6.300 mmol) and Te (803 mg, 6.300 mmol) were added into a solution of deionised water, ethylene glycol, and hydrazine hydrate with a molar ratio of 7:3:1 respectively in a 50mL round bottom flask. The mixture was refluxed while stirring vigorously at 75 °C for 5 min. A 5% molar solution of PPI solution was added into the solution. The resulting solution was refluxed at 75 °C for 24 h under vigorous stirring. The resulting precipitates were washed three with absolute ethanol. The product was dried under vacuum at 60°C for overnight. Similar procedure was used to synthesize CuSb@PPI by adding CuCl₂ (400 mg, 2.980 mmol) and SbCl₂ (679 mg, 2.98 mmol) into a solution of deionised water, ethylene glycol, and hydrazine hydrate with a molar ratio of 7:3:1 respectively in a 50 mL round bottom flask [7].

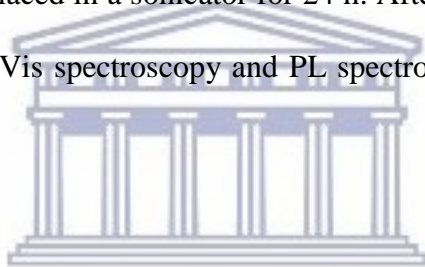
3.7 Blending of PCDTBT and Core-Shell Nanoparticles

Solutions of CuTe (5 mg), CuSb (5 mg) and PPI (5 mg) were prepared in 5 mL of chlorobenzene, while core-shell nanoparticles (CuTe@PPI (15 mg) and CuSb@PPI (15 mg))

and PCDTBT (15 mg) were prepared each in 15 mL chlorobenzene. The solutions were placed in a sonicator for 1 h. After 1 h, solutions of different volume ratios were prepared:

- (i) 0.5 mL of PCDTBT: 1.5 mL of CuTe nanoparticles
- (ii) 0.5 mL of PCDTBT: 1.5 mL of CuSb nanoparticles
- (iii) 0.5 mL of PCDTBT: 1.5 mL of PPI
- (iv) 0.5 mL of PCDTBT: 0.5 mL of core-shell nanoparticles
- (v) 0.5 mL of PCDTBT: 1.5 mL of core-shell nanoparticles
- (vi) 0.5 mL of PCDTBT: 2.5 mL of core-shell nanoparticles
- (vii) 0.5 mL of PCDTBT: 5.0 mL of core-shell nanoparticles

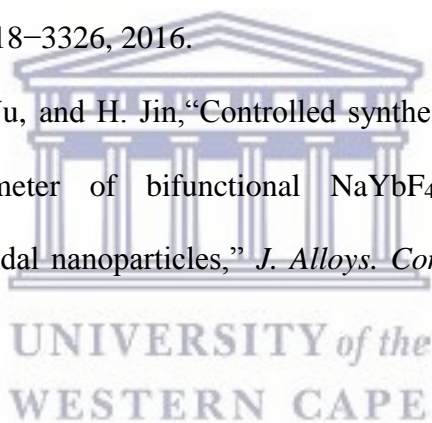
The resulting solutions were placed in a sonicator for 24 h. After 24 h, the resulting solutions were characterized using UV-Vis spectroscopy and PL spectroscopy to study photophysical properties.



3.8 References

1. P. Kumar and K. Singh, "Element directed aqueous solution synthesis of copper telluride nanoparticles, characterization, and optical properties," *Cryst. Growth Des.*, vol. 9, pp. 3089-3094, 2009.
2. M. Mellah, A. Voituriez, and E. Schulz, "Electropolymerized Cr – salen complexes for the heterogeneous asymmetric hetero Diels-Alder reaction," *J. Mol. Catal.*, vol. 272, pp. 20–25, 2007.
3. W. Zhang, W. H. Sun, B. Wu, S. Zhang, H. Ma, Y. Li, J. Chen, P. Hao, "Synthesis of palladium complexes containing 2-methoxycarbonyl-6-iminopyridine ligand and their catalytic behaviors in reaction of ethylene and norbornene, *J. Organomet. Chem.*, vol. 691, pp. 4759-4767", 2006.
4. A. Zulauf, M. Mellah, R. Guillot, and E. Schulz, "Chromium-thiophene-salen-based

- polymers for heterogeneous asymmetric hetero-Diels-Alder reactions,” *European. J. Org. Chem.*, vol. 12, pp. 2118–2129, 2008.
5. J. Martinovic, A. Chiorcea-Paquim, V. C. Diculescu, J. Van Wyk E. Iwuoha, P. Baker, S. Mapolie, A. Oliveira-Brett, “Metallo-functionalized first-generation salicylaldehyde poly(propyleneimine) tetraamine dendrimers: Electrochemical study and atomic force microscopy imaging,” *Electrochim. Acta* 53., vol. 53, pp. 4907–4919, 2008.
6. A. Zimpel, T. Preiß, R. Röder, H. Engelke, M. Ingrisch, M. Peller, J. O. Rädler, E. Wagner, T. Bein, U. Lächelt, and S. Wuttke, “Imparting functionality to MOF nanoparticles by external surface selective covalent attachment of polymers,” *Chem. Mater.*, vol. 28, pp. 3318–3326, 2016.
7. X. Wang, T. Xu, T. Vu, and H. Jin, “Controlled synthesis, multicolor luminescence, and optical thermometer of bifunctional $\text{NaYbF}_4:\text{Nd}^{3+}@\text{NaYF}_4:\text{Yb}^{3+}$ active-core/active-shell colloidal nanoparticles,” *J. Alloys. Compd.*, vol. 691, pp. 530–536, 2017.



CHAPTER 4: CHARACTERIZATION OF CuTe and CuSb NANOPARTICLES SYNTHESIZED VIA CHEMICAL REDUCTION

This chapter focuses on characterization of CuTe NPs and CuSb NPs synthesized via chemical reduction using hydrazine hydrate and mixture of water and ethylene glycol as a solvent. Synthesized CuTe NPs and CuSb NPs were characterized by UV-Vis spectroscopy, FTIR spectroscopy, XRD, HR-SEM, HR-TEM, EDX and electrochemical techniques such as CV and SWV.

4.1 UV-Vis studies of the synthesized CuTe NPs and CuSb NPs

To study the optical properties of the synthesized CuTe NPs and CuSb NPs, the UV-Vis absorption was employed using chlorobenzene as a solvent at room temperature. From Figure 4.1(A), CuTe NPs have a UV-Vis band at 860 nm, while Figure 4.1(B) (CuSb NPs) shows two bands at 509 nm and 631 nm. The absorption spectra of CuTe NPs and CuSb NPS were studied without taking transmission and reflection losses into consideration. Both CuSb NPs and CuTe NPs were black in colour and their colour is confirmed by the non-zero absorbance in the entire wavelength range used during this study [1]. The absorption spectrum of CuTe NPs revealed the suppression of absorption bands from the spectrum of Copper at 302 nm and 626 nm, Tellurium at 303 nm. An absorption spectrum of CuSb NPs revealed suppressed absorption bands from spectra of Copper at 302 nm and Antimonide at 304 nm and 840 nm. This suppression of absorption bands confirms the formation of CuTe NPs and CuSb NPs [2]. The optical band gap of CuTe NPs and CuSb NPs are related with the corresponding absorption coefficient α by the equation:

$$\alpha = \frac{k(h\nu - E_g)^{\frac{n}{2}}}{h\nu} \dots\dots\dots \text{Equation 1}$$

where k and n are constants where n is equal to 4 for indirect band gap and 1 for direct band gap semiconductor materials and E_g is an optical band gap [3]. In this study, we focus only

on direct band gap were $(ahv)^2$ against $h\nu$ was plotted for both CuTe NPs and CuSb NPs. The straight line-portion of the plot was extrapolated to zero absorption coefficient value to get a direct energy band gap for CuTe NPs and CuSb NPs. The direct energy band gap was found to be 1.14 eV for CuTe NPs and 1.25 eV for CuSb NPs shown on figure 4.1(C and D).

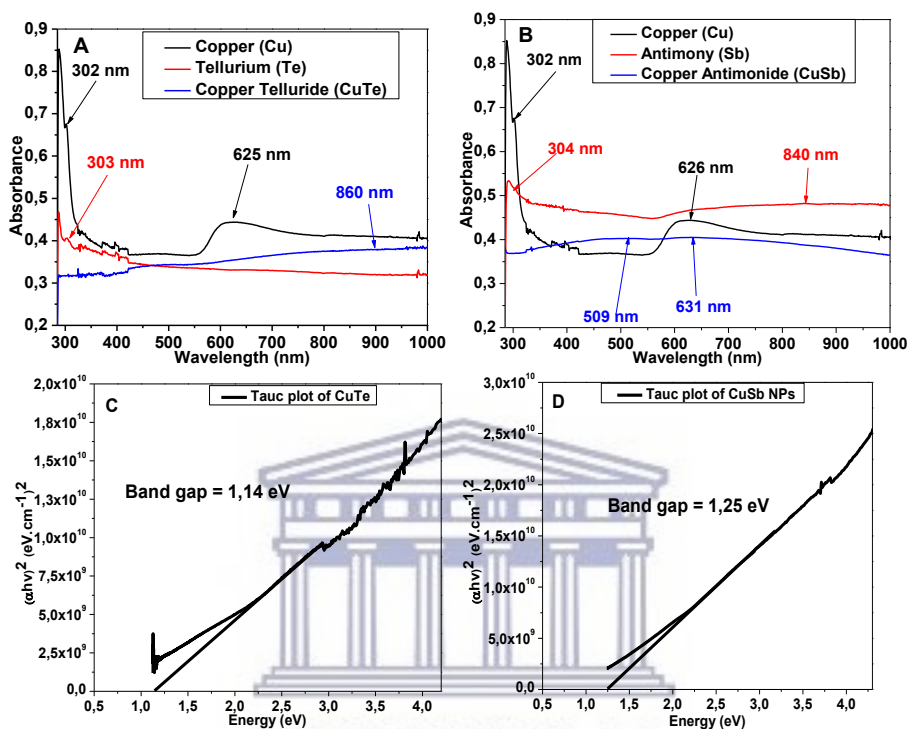


Figure 4. 2: The absorbance spectra of CuTe NPs (A) and CuSb NPs (B) at room temperature with the variation of $(ah\nu)^2$ versus $h\nu$ for direct band gap calculation for both CuTe NPs (C) and CuSb NPs (D) respectively.

4.2 FTIR studies of the synthesized CuTe NPs and CuSb NPs

Figure 4.2 shows the FTIR spectra of CuTe NPs and CuSb NPs which were determined by milling the NPs with KBr. The CuTe NPs and CuSb NPs were washed three times with deionised water and three times with absolute ethanol to remove impurities. Both CuTe NPs (A) and CuSb NPs (B) shows an O-H stretching bands at 3396.80 cm^{-1} and 3425.60 cm^{-1} , while the O-H bending bands are observed at 1643.50 cm^{-1} and 1618.56 cm^{-1} respectively. These bands confirm the adsorption of ethylene glycol on the surface of NPs [3]. The

absorption bands at 1384.40 cm^{-1} on CuTe NPs spectrum and 1416.00 cm^{-1} on CuSb NPs spectrum are the absorption bands of the C-H bonds bending. The spectrum of CuSb NPs shows two bands at 1085.00 cm^{-1} and 967.50 cm^{-1} which are the C-C-O asymmetric stretch and C-C-O symmetric stretch respectively. This bands confirms the presence of ethylene glycol [4]. The bands at 748.46 cm^{-1} and 742.25 cm^{-1} confirms the adsorption of the O-H group on the surface of the CuTe NPs and CuSb NPs respectively [5], [6].

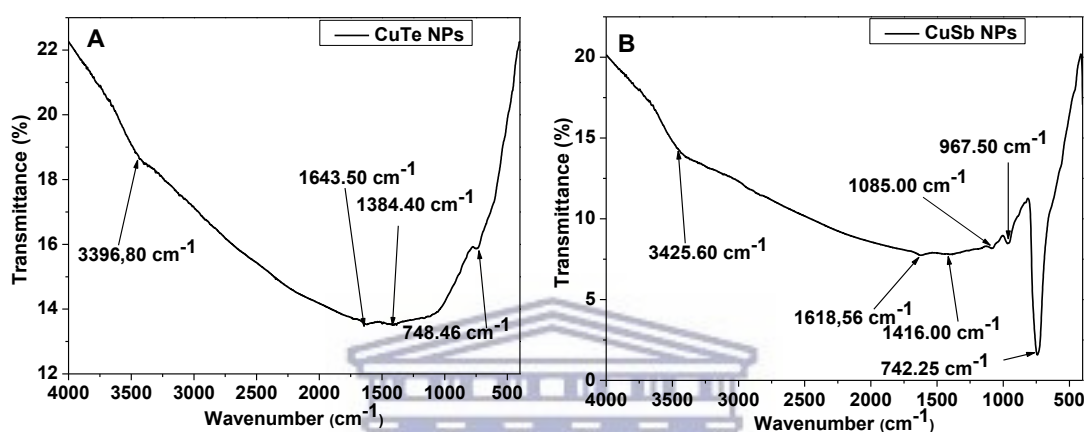


Figure 4. 3: FT-IR spectra of CuTe NPs (A) and CuSb NPs (B) milled in KBr at room temperature.

4.3 X-ray Diffraction analysis of CuTe NPs and CuSb NPs

Powder XRD pattern of CuTe NPs and CuSb NPs are shown in figure 4.3(A) and figure 4.3(B) respectively. The peaks at 12.07° , 19.76° , 26.73° , 27.56° , 31.76° , 35.02° , 38.20° , 40.4° , 43.67° , 45.58° , 53.58° and 56.96° from figure 3(A) correspond to (001), (110), (002), (102), (112), (202), (103), (212), (113), (203), (104) and (204) reflections of Cu_2Te NPs respectively which are in good agreement with hexagonal crystalline phase. These confirm successful synthesis of CuTe NPs with 2Cu:1Te mass ratio. Similar results were reported by Kumar *et al.* [3] and Amiraslanov *et al.* [7]. From figure 3(B), peaks at 13.67° , 27.59° , 29.58° , 32.09° , 34.94° , 43.37° , 48.295° , 50.49° , 54.44° , 57.17° and 59.04° corresponds to (001), (101), (002), (110), (111), (112), (200), (103), (202), (113) and (212) reflections of Cu_2Sb NPs respectively which are in good agreement with tetragonal crystalline phase.

Similar study was reported by Prieto *et al.* [8], [9]. The sizes of NPs were estimated using Scherrer equation:

$$A = \frac{0.94\lambda}{\beta \cos\theta} \dots\dots\dots \text{Equation 2}$$

Where A is the particles size, β is the full width at half maximum of the peak, θ is an angle of diffraction and λ is the wavelength of the X-ray radiation. Particle sizes was obtained from the most intense peaks which are at $2\theta = 43.67^\circ$ and $2\theta = 27.59^\circ$ resulting to 27.6 nm for CuTe NPs and 47.6 nm for CuSb NPs respectively. The method used to calculate particle sizes was also used by Chandra *et al.* [10].

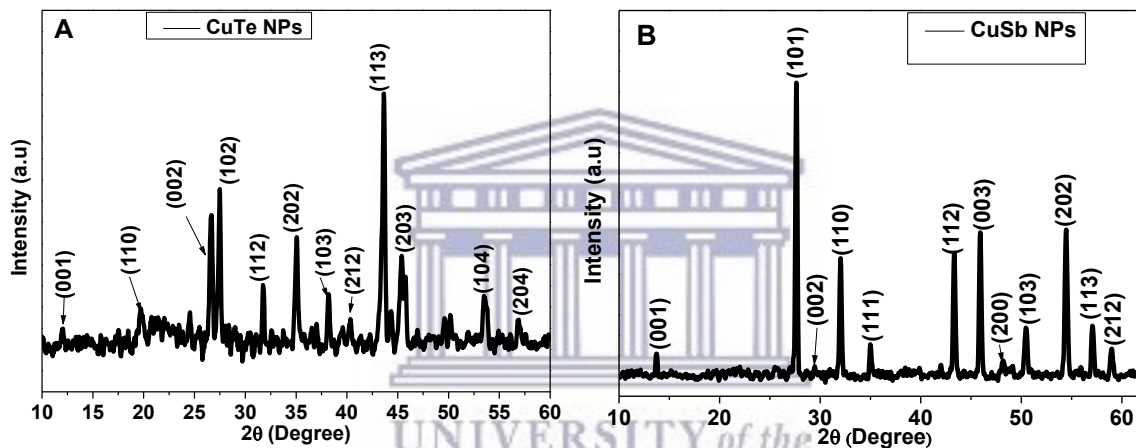


Figure 4. 4: Powder X-ray diffraction pattern of CuTe NPs (A) and CuSb NPs (B).

4.4 Morphological and Compositional Analysis of CuTe NPs and CuSb NPs

The morphological and elemental studies of CuTe NPs and CuSb NPs were done using electron microscopes (TEM and SEM) and EDX respectively.

4.4.1 TEM analysis of CuTe NPs and CuSb NPs

From TEM images shown in figure 4.4, the particles on both images are well distributed due to the presence of ethylene glycol. It was reported that the main reasons for using organic solvents such as ethylene glycol, glycerol or diethylene glycol is that they can also act as stabilising agents which turns to limits the particles growth and agglomeration. They turn to get adsorbed on the surface of the NPs, they continue to adsorb-desorbs on/from surface of

NPs until they form a thin layer that causes the NPs to disperse [11], [12]. The average particle sizes of CuTe NPs with hexagonal shape and CuSb NPs with oval shape were found to be 8.69 nm and 19.00 nm respectively. For CuTe NPs (figure 4.4 (E)), the particles are distributed from 2.17 nm to 29.90 nm. As for CuSb NPs (figure 4.4 (F)), the range of distribution is 5.52 nm to 49.65 nm. These results are in agreement with the results obtained from the XRD analysis. The TEM images for both CuTe NPs (C) and CuSb NPs (D) shows lattices fringes which are shown by drawn black rectangles on the images shows that the NPs have crystalline phases. This observation agrees with the results obtained from XRD analysis. This observation was also observed by Wang *et al.* [13].

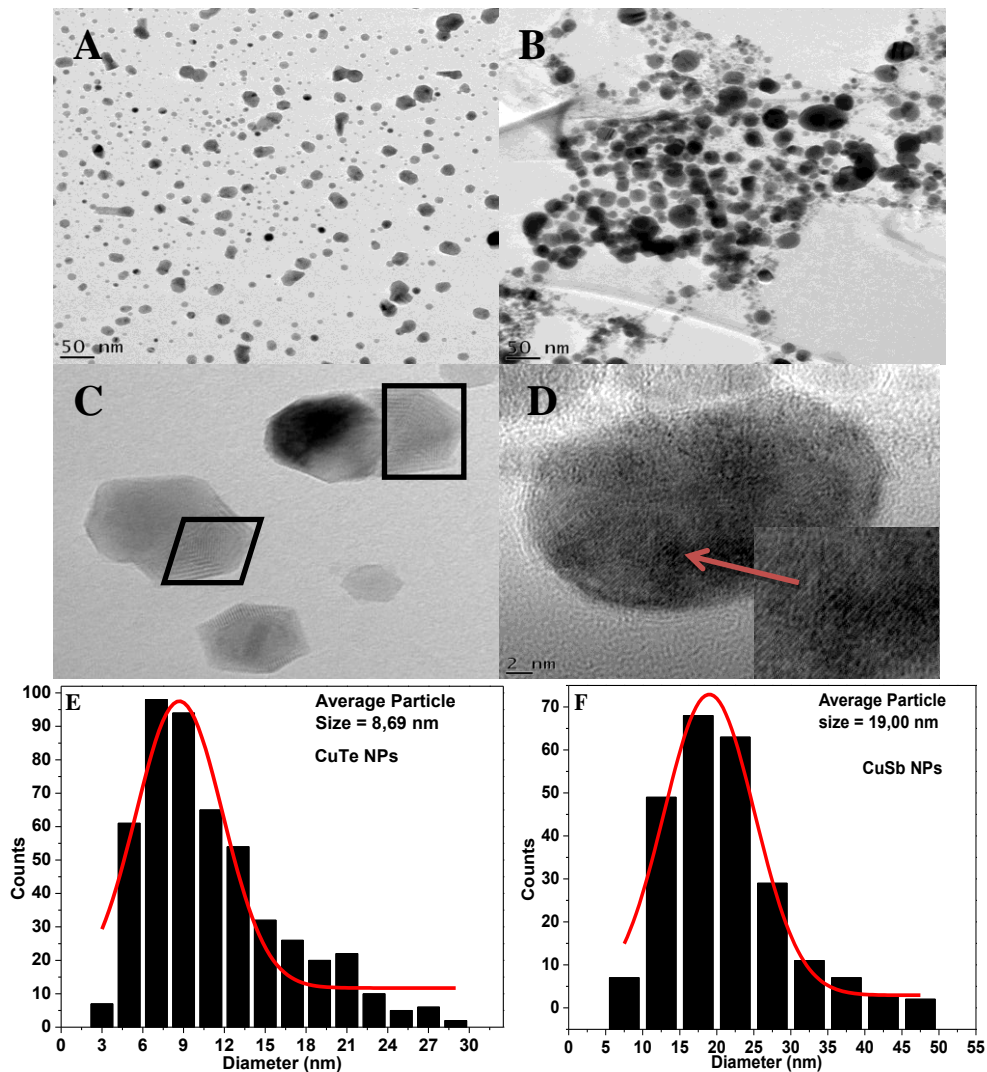


Figure 4. 5: TEM image of CuTe NPs (A and C) and CuSb NPs (B and D), Particle sizes distribution of CuTe NPs (E) and CuSb NPs (F).

4.4.2 Energy dispersive X-ray (EDX) spectra of the CuTe NPs and CuSb NPs

The elements present in the synthesized NPs were confirmed by EDX studies. Figure 4.5 shows the spectrum of CuTe NPs (A) and CuSb NPs (B). The spectra showed the presence of all elements expected from the synthesized NPs. For CuTe NPs (A), it confirmed the presence of 51.06% Cu, 44.55% Te, 3.32% C and 1.05% O. The weight percentages of Cu and Te show that the synthesised CuTe NPs have the stoichiometric ratio of 2Cu:1Te which results to Cu₂Te NPs. These results are in agreement with the results obtained from XRD. For CuSb NPs, it shows the presence of 23.76% Cu, 51.73% Sb, 12.90% C, and 11.60% O. The weight percentages of the synthesised CuSb NPs have the stoichiometric ratio of 1Cu:1Sb which confirms that the synthesized NPs are CuSb NPs. These results do not agree with the results obtained from XRD. Nickel (Ni) appears in both spectrum of NPs. It comes from the nickel grid used during analysis. Carbon (C) and Oxygen (O) come from the ethylene glycol adsorbed on the surface of the NPs.

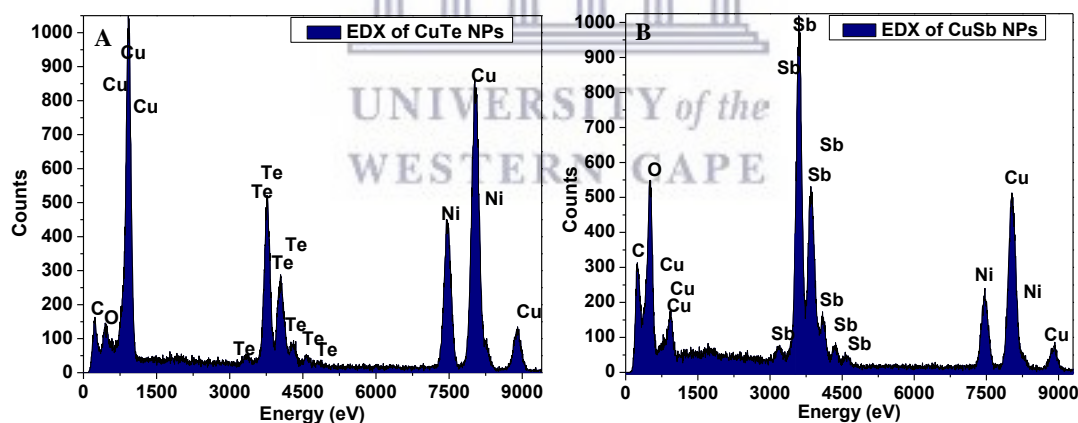


Figure 4. 6: EDX results of CuTe NPs (A) and CuSb NPs (B).

4.4.3 SEM analysis of CuTe NPs and CuSb NPs

Figure 4.6(A) and Figure 4.6(B) shows the SEM images of CuTe NPs and CuSb NPs respectively. The images show rough surface NPs with their size distribution shown by figure 4.6(C and D). The average particle size was determined to be 15.74 nm and 11.64 nm for

CuTe NPs and CuSb NPs respectively. These results are in agreement with the results obtained from TEM.

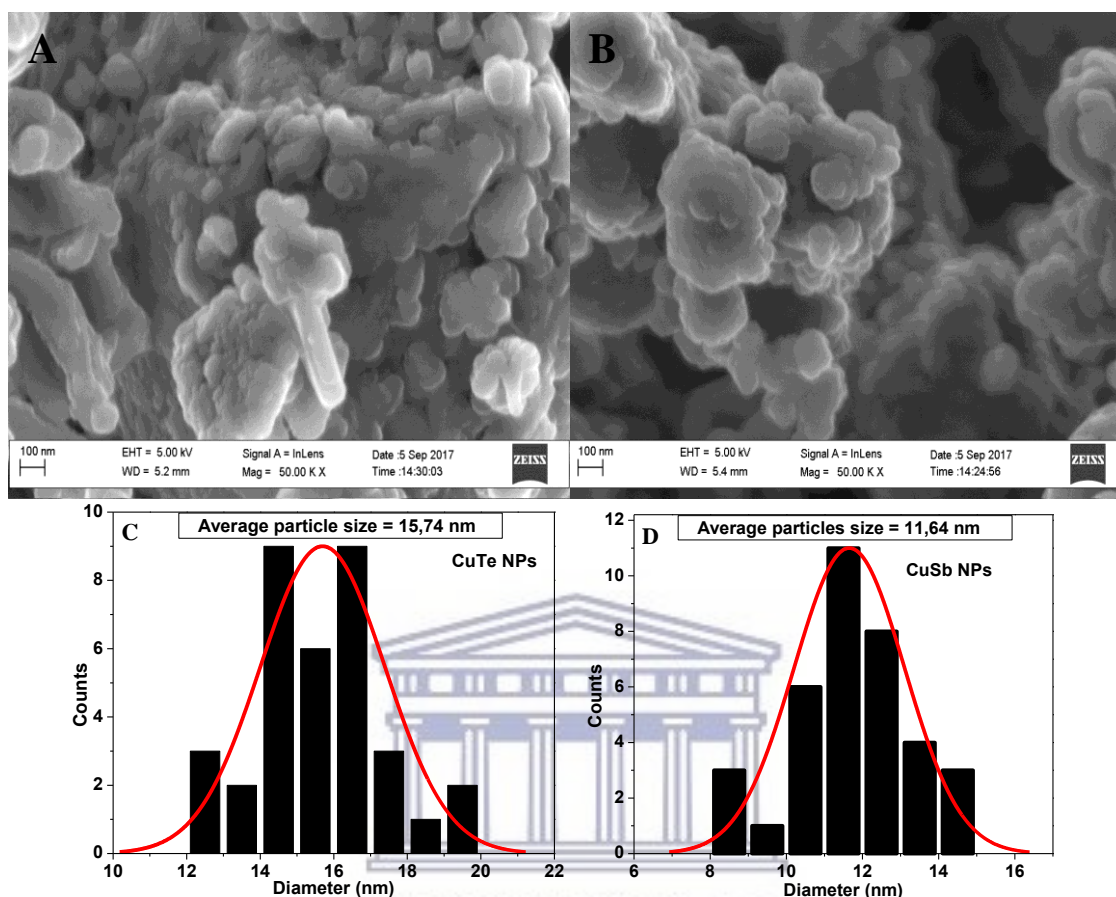


Figure 4. 7: SEM image of CuTe NPs (A) and CuSb NPs (B), Particle sizes distribution of CuTe NPs (C) and CuSb NPs (D).

4.4.4 Energy dispersive X-ray (EDX) spectra of the CuTe NPs and CuSb NPs

Figure 4.7 shows the EDX spectra of CuTe NPs (A) and CuSb NPs (B). For CuTe NPs (A), it confirms the presence of 34.25% Cu, 64.19% Te and 1.56% O. The weight percentages of Cu and Te show that the synthesised CuTe NPs have the stoichiometric ratio of 1Cu:1Te which results to CuTe. These results are not in agreement with the results obtained from XRD and TEM. This confirms that NPs with different elemental weight percentages were synthesized. For CuSb NPs, it shows the presence of 31.74% Cu, 59.08% Sb and 9.17% O. The weight percentages of the synthesised CuSb NPs have the stoichiometric ratio of 1Cu:1Sb which confirms that the synthesized NPs are CuSb NPs. These results agree with the results

obtained from TEM. Carbon (C) and Oxygen (O) come from the ethylene glycol adsorbed on the surface of the NPs. Carbon is also detected from the carbon coated on the sample before analysis.

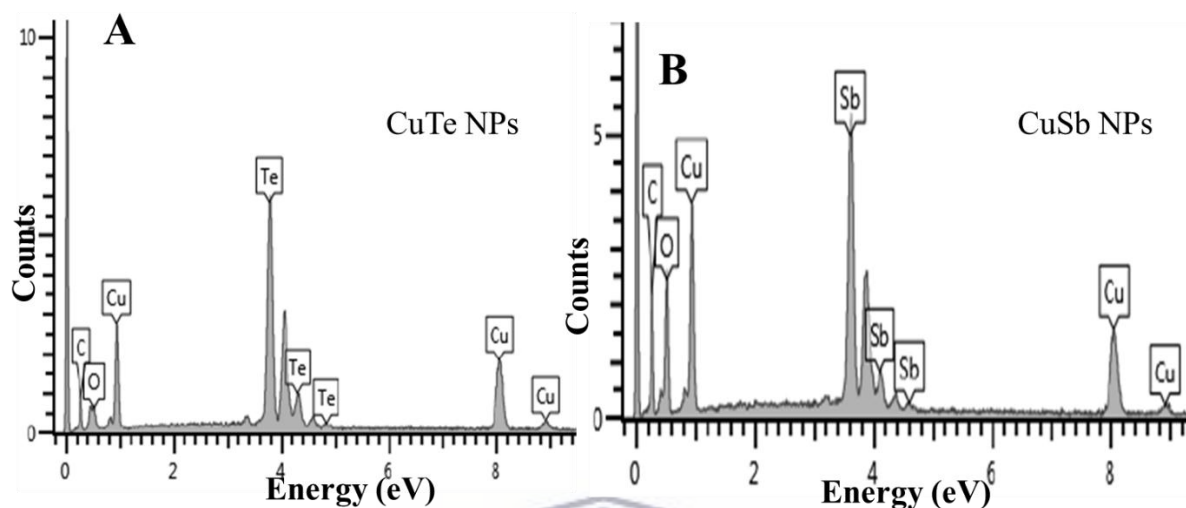


Figure 4. 8: EDX results of CuTe NPs (A) and CuSb NPs (B).

4.5 Electrochemical characteristics of CuTe NPs and CuSb NPs in sulphuric acid medium

Electrochemistry can be considered as an ideal study since it can study the surface behaviour of an electrode sensitively by voltammograms. CV and SWV studied on a polished surface of the glass carbon electrode (GCE) were carried out in 1 M H₂SO₄ solution at 25 °C. From each sample, a concentration 0.05 M was prepared in 5 mL of H₂SO₄ as a solvent. The prepared solution was transferred to an electrochemical cell. It was flushed with nitrogen gas for 10 min before run the electrochemical experiment. Before electrochemical studies of CuTe NPs and CuSb NPs, electrochemical studies of GCE in 1 M H₂SO₄, copper (Cu), tellurium (Te), copper (II) chloride and antimony (III) chloride precursors were conducted

4.5.1 Electrochemical studies of GCE in 1M H₂SO₄

The CV and SWV for GCE in 1 M H₂SO₄ is shown on figure 4.8(A) and figure 4.8(B) respectively. These electrochemical studies were carried out to get the redox peaks on the

surface of GCE in 1 M H₂SO₄ solution and are shown in figure 4.8. Voltammograms from both techniques shows three peaks labelled as I, II and III from the voltammograms. Peak I is due to the hydrogen desorption while peak II are due to hydrogen adsorption. Similar results were reported by Cohen *et al.* [14] and Daubinger *et al.* [15]. Peak III shows the presence of oxygen in the electrolyte solution. SWV (figure 4.8(B)) shows a new peak IV with is due to the reduction of oxide [30].

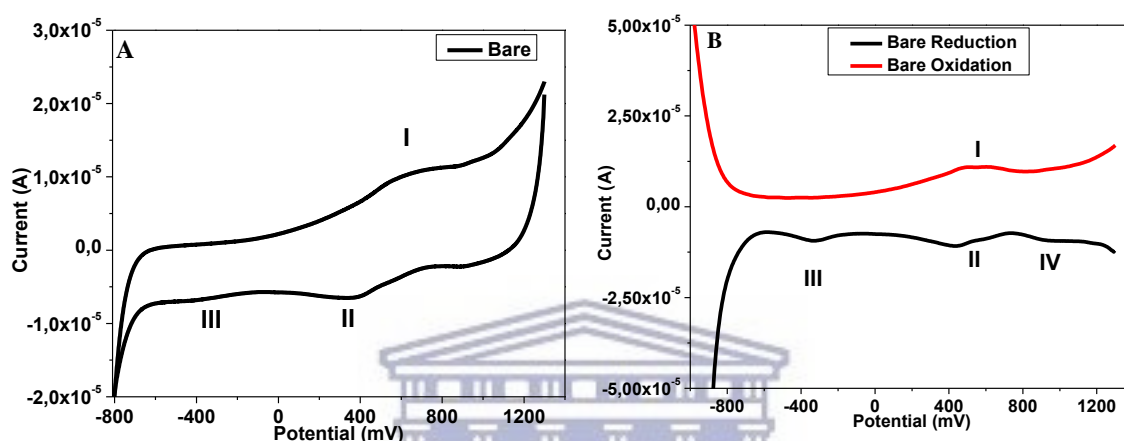


Figure 4. 9: CV (A) at scan rate of 100 mVs⁻¹ and SWV (B) of GCE in 1 M H₂SO₄.

A concentration of 0.05 M was prepared from each powder of precursors (Cu, CuCl₂, Te and SbCl₃) using electrolyte (1 M H₂SO₄) as a solvent to obtain the voltammograms in figure 4.9(A, B, C and D). Figure 4.9(A) shows the cyclic voltammograms of Cu which has one oxidation peak I (533.6 mV) and one reduction peak II (-78.3 mV). Oxidation peak I due to the oxidation of Cu which is given by the equation: $\text{Cu} \rightarrow \text{Cu}^{2+} + 2\text{e}^-$, while the reduction peak (II) is due to $\text{Cu}^{2+} + 2\text{e}^- \rightarrow \text{Cu}$ [24]. Three Oxidation peaks (I, II and III) and two reduction peaks (IV and H₂ desorption) were observed from figure 4.9(B). The oxidation peak I (357.6 mV) is assigned to Te⁰ to Te²⁺, oxidation peak II (613.4 mV) is assigned to oxidation of Te²⁺ to Te⁴⁺ and oxidation peak III (813.6 mV) is assigned to oxidation of Te⁴⁺ to Te⁶⁺. The reduction peak IV (-643.9 mV) is assigned to reduction of Te⁶⁺ to Te⁰ [25], [26]. Figure 4.9(C) shows a cyclic voltammogram for CuCl₂ which shows two oxidation peaks (I and II) which shows that it losses one electron at a time. Oxidation peak I (118.4 mV) and II

(256.5 mV) are assigned to oxidation of $\text{Cu} \rightarrow \text{Cu}^+ + \text{e}^-$ and $\text{Cu}^+ \rightarrow \text{Cu}^{2+} + \text{e}^-$ respectively. The reduction of $\text{Cu}^{2+} \rightarrow \text{Cu} + \text{e}^-$ takes place at the one potential which is labelled III [27], [28]. Figure 4.9(D) shows a cyclic voltammogram of SbCl_3 which shows oxidation peaks I (50.1 mV), II (138.13 mV) and III (207.6 mV) which are assigned to $\text{Sb} \rightarrow \text{Sb}^+ + \text{e}^-$, $\text{Sb}^+ \rightarrow \text{Sb}^{2+} + \text{e}^-$ and $\text{Sb}^{2+} \rightarrow \text{Sb}^{3+} + \text{e}^-$ respectively. It also shows reduction peaks IV (-422.1 mV) and V (-473.9 mV) which are assigned to $\text{Sb}^{3+} + \text{e}^- \rightarrow \text{Sb}^{2+}$ and $\text{Sb}^{2+} + 2\text{e}^- \rightarrow \text{Sb}$ [29].

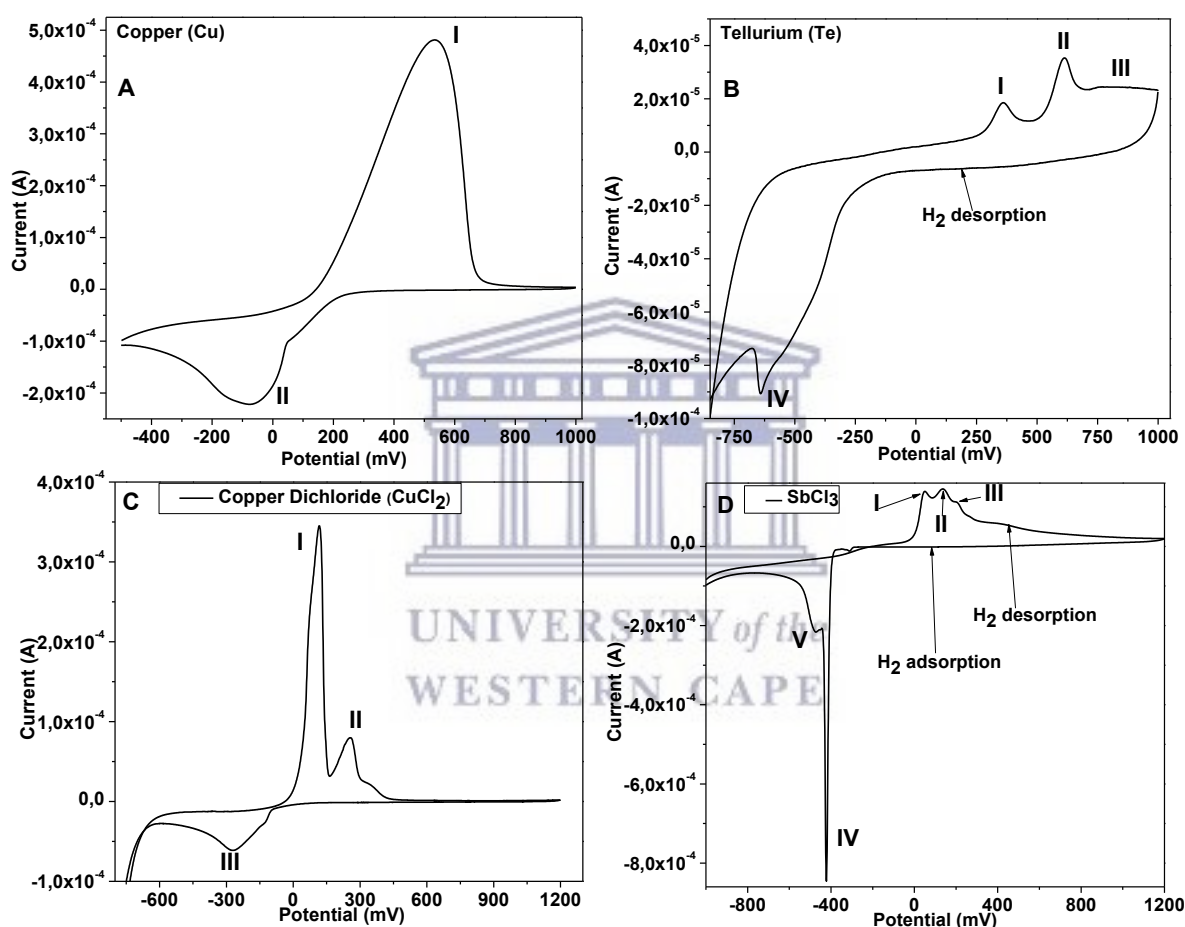


Figure 4. 10: The voltammograms of precursors: (A) Copper, (B) Tellurium, (C) Copper (II) chloride and (D) Antimony (III) chloride in 1 M H_2SO_4 at scan rates of 100 mV s^{-1} .

Figure 4.10 shows the voltammograms for CuTe NPs (A, B and C) and CuSb NPs (D, E and F). From figure 4.10(A), four oxidation peaks labelled as I (288 mV), II (409.8 mV), III (612.4 mV) and IV (789.3 mV) were observe which are respectively due to oxidation of $\text{Cu}_2\text{Te} \rightarrow \text{Te}^0 + 2\text{e}^- + 2\text{Cu}^+$, $\text{Cu}^+ \rightarrow \text{Cu}^{2+} + \text{e}^-$, $\text{Te}^0 \rightarrow \text{Te}^{4+} + 4\text{e}^-$ and $\text{Te}^{4+} \rightarrow \text{Te}^{6+} + 2\text{e}^-$. Then, the

reduction peak IV (114.6 mV) and peak V (-36.4 mV) were also observed. These reduction peaks were due to reduction of $\text{Te}^{6+} \rightarrow \text{Te}^{4+} + 2\text{e}^-$ and $\text{Te}^{4+} \rightarrow \text{Te}^0 + 4\text{e}^-$ respectively. Figure 10(C) shows an additional peak VI at -305.1 mV which is due to the reduction of $\text{Te}^0 \rightarrow \text{Te}^{2-} + 2\text{e}^-$ and $\text{Cu}^{2+} \rightarrow \text{Cu}^+ + \text{e}^-$ which indicate the formation of CuTe NPs. These results reported by consulting the electrochemistry studies of Ag_2Te [16], CdSe [17] and CdTe [18] and are in agreement with the results obtained by Wang *et al.* [19] and Caballero-Briones *et al.* [20] which confirms that the synthesized CuTe NPs have an atomic ratio of 2 Cu:1 Te. From figure 4.10(C and F), it can be clearly seen that as the scan rate increases, the peak potential changes in such a way that the formal potential increases. This phenomenon indicates that the systems are quasi-reversible. Electrochemical responses of CuSb NPs are shown on voltammograms in figure 4.10(D, E and F). Figure 4.10(D) shows the comparison of CuSb NPs with the precursors CuCl_2 and SbCl_3 . It shows two Oxidation peaks were peak I (203.5 mV) is due to the oxidation of $\text{CuSb} \rightarrow \text{Sb}^0 + \text{e}^- + \text{Cu}^+$ and peak II (544.5 mV) is due to the overlap of the oxidation of $\text{Cu}^+ \rightarrow \text{Cu}^{2+} + \text{e}^-$, $\text{Sb}^0 \rightarrow \text{Sb}^{3+} + 3\text{e}^-$ and H_2 desorption. Reduction peak III (-234.7 mV) is due to reduction $\text{Cu}^{2+} \rightarrow \text{Cu}^+ + \text{e}^-$ while the reduction peaks IV (-538.1 mV) and V (-614.4 mV) are due to reduction of $\text{Sb}^{3+} + \text{e}^- \rightarrow \text{Sb}^0$. Peaks IV and V, they somehow overlap which is the sign of the formation of CuSb NPs. Figure 4.10(F) confirms the presence all peaks observed on Figure 4.10(D) without any additional peak. These results are reported after consulting electrochemical studies of Cu_2Sb [21], InSb [22] and Li- Cu_2Sb [23].

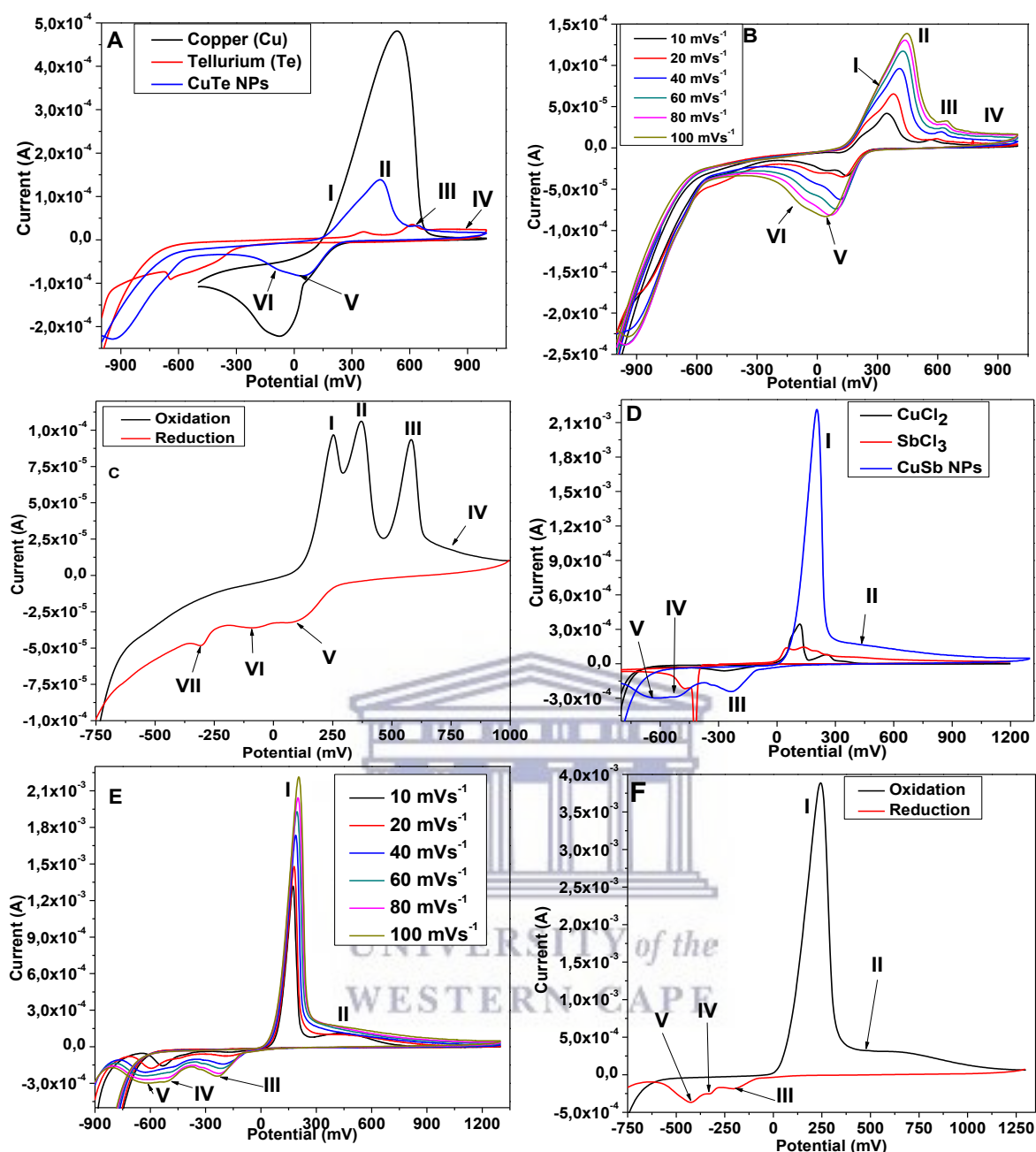


Figure 4. 11: The voltammograms of CuTe NPs and CuSb NPs were obtained at different potential regions: (A) comparison of CuTe NPs with precursors at scan rate of 100 mVs^{-1} ; (B) CuTe NPs at different scan rates, (C) SWV of CuTe NPs (D) comparison of CuSb NPs with precursors at scan rate of 100 mVs^{-1} ; (E) CuSb NPs at different scan rates, (F) SWV of CuSb NPs in $1 \text{ M H}_2\text{SO}_4$.

4.6 Sub-Conclusion

Successful synthesis of CuTe NPs and CuSb NPs were confirmed by variety of characterization techniques. UV-Vis spectroscopy results showed that absorption response of CuTe NPs and CuSb NPs are different from those of precursors while FTIR confirms the adsorption of ethylene glycol on the surface of the NPs. XRD showed that the synthesized NPs are crystalline. HR-TEM showed that the synthesized CuTe NPs and CuSb NPs have the average diameter of 8.69 nm and 19.00 nm while HR-SEM represented the average diameter of 15.74 nm and 11.64 nm respectively.

4.7 References

1. D. Wang, J. Yang, X. Li, J. Wang, J. Lang, and J. Wang, "Preparation of morphology-controlled TiO₂ nanocrystals for the excellent photocatalytic activity under simulated solar irradiation," *Mater. Res. Bull.*, vol. 94, pp. 38–44, 2017.
2. J. F. Sánchez-Ramírez and U. Pal, "Optical absorption of colloidal dispersion of bimetallic nanoparticles Au/Pd," *J. Vac. Sci. Technol.*, vol. 13, pp. 114–116, 2001.
3. P. Kumar and K. Singh, "Element directed aqueous solution synthesis of copper telluride nanoparticles , characterization , and optical properties," *Cryst. Growth. Des.*, vol. 9, pp. 3089–3094, 2009.
4. B. C. Smith, "Alcohols—the rest of the story," *Spectrosc. Lett.*, vol. 32, pp. 19-23, 2017.
5. G. E. Rachkovskaya, G. B. Zakharevich, and E. Results, "IR spectra of tellurium germanate glasses and their structure," *J. Appl. Spectrosc.*, vol. 74, pp. 78–81, 2007.
6. G. Carotenuto, M. Palomba, S. De Nicola, G. Ambrosone, and U. Coscia, "Structural and photoconductivity properties of structural and photoconductivity properties of tellurium / PMMA films," *Nanoscale. Res. Lett.*, 2015.
7. I. R. Amiraslanov, N. A. Alieva, G. G. Guseinov, and G. M. Agamirzoeva, "Crystal

- structure of Cu_{2-m}Te ($m = 0.25$),” *Crystallogr. Rep.*, vol. 62, pp. 210–214, 2017.
8. E. D. Jackson and A. L. Prieto, “Copper antimonide nanowire array lithium ion anodes stabilized by electrolyte additives,” *ACS. Appl. Mater. Interfaces.*, vol. 8, pp. 30379-30386, 2016.
 9. J. M. Mosby and A. L. Prieto, “Direct electrodeposition of Cu_2Sb for lithium-ion battery anodes,” *J. Am. Chem. Soc.*, vol. 80523, pp. 10656–10661, 2008.
 10. C. Paper, S. Ambosakka, and U. Hasanuddin, “Thermal and infrared studies of garnierite from the Soroako nickeliferous laterite deposit, Sulawesi, Indonesia,” *Jurnal. Geologi. Indonesia.*, vol. 7, pp. 77-85, 2015.
 11. C. Hai, S. Li, Y. Zhou, J. Zeng, X. Ren, and X. Li, “Roles of ethylene glycol solvent and polymers in preparing uniformly distributed MgO nanoparticles,” *Integr. Med. Res.*, vol. 5, pp. 176–182, 2017.
 12. J. Wojnarowicz A. Opalinska, T. Chudoba, S. Gierlotka, R. Mukhovskiy, E. Pietrzykowska, K. Sobczak, and W. Lojkowski, “Effect of water content in ethylene glycol solvent on the size of ZnO nanoparticles prepared using microwave solvothermal synthesis,” *J. Nanomater.*, vol. 2016, 2016.
 13. W. Wang, G. Hu, Z. Peng, K. Du, Y. Cao, and J. Duan, “Nano-sized over-lithiated oxide by a mechano-chemical activation-assisted microwave technique as cathode material for lithium ion batteries and its electrochemical performance,” *Cereal. Chem.*, vol. 44, pp. 1425–1431, 2018.
 14. D. Abrun, J. L. Cohen, and D. J. Volpe, “Electrochemical determination of activation energies for methanol oxidation on polycrystalline platinum in acidic and alkaline electrolytes,” *Phys. Chem. Chem. Phys.*, vol. 9, pp. 49-77, 2007.
 15. P. Daubinger, J. Kieninger, T. Unmu, and G. A. Urban, “Electrochemical characteristics of nanostructured platinum electrodes – a cyclic voltammetry study,”

- Phys. Chem. Chem. Phys.*, vol. 16, pp. 8392–8399, 2014.
16. P. Zuo, S. Zhang, B. Jin, Y. Tian, and J. Yang, “Rapid synthesis and electrochemical property of Ag₂Te nanorods,” *J. Phys. Chem. C.*, vol. 112, pp. 14825–14829, 2008.
 17. S. Kim, W. Han, and J. Lee, “Electrochemical characterization of CdSe and CdTe thin films using cyclic voltammetry,” *Curr. Appl. Phys.*, vol. 10, pp. S481–S483, 2010.
 18. P. Sobrova, M. Ryvolova, J. Hubalek, and V. Adam, “Voltammetry as a tool for characterization of CdTe quantum dots,” *Int. J. Mol. Sci.*, vol. 14, pp. 13497–13510, 2013.
 19. H. Wang, P. Zuo, A. Wang, S. Zhang, C. Mao, J. Song, H. Niu, B. Jin, and Y. Tian “Facile synthesis and electrochemical property of Cu₂Te nanorods,” *J. Alloys. Compd.*, vol. 581, pp. 816–820, 2013.
 20. F. Caballero-briones, A. Palacios-padrós, J. L. Peña, and F. Sanz, “Phase tailored, potentiodynamically grown p-Cu_{2-x}Te/Cu layers,” *Electrochem. commun.*, vol. 10, pp. 1684–1687, 2008.
 21. L. Wang, C. Wang, N. Zhang, F. Li, F. Cheng, and J. Chen, “High anode performance of in situ formed,” *ACS. Energy. Lett.*, vol. 2, pp. 265 -262, 2017.
 22. T. Sarakonsri, C. S. Johnson, S. A. Hackney, and M. M. Thackeray, “Solution route synthesis of InSb , Cu₆Sn₅ and Cu₂Sb electrodes for lithium batteries,” *J. Power. Sources.*, vol. 153, pp. 319–327, 2006.
 23. H. Bryngelsson, J. Eskhult, and K. Edstr, “Thin films of Cu₂Sb and Cu₉Sb₂ as anode materials in Li-ion batteries,” *Electrochim. Acta.*, vol. 53, pp. 7226–7234, 2008.
 24. E. P. Grishina, A. M. Udalova, and E. M. Rummyantsev, “Anodic oxidation of copper in concentrated sulphuric acid solutions,” *Russ. J. of electrochem.*, vol. 38, pp. 1041-1045, 2002.
 25. Y. Feng, and M. Gu, “The electrochemical behavior of tellurium on GCE in sol and

- solutions,” *Electrochim. Acta*, vol. 90, pp. 416-420, 2013.
26. R. W. Tsai, Y. T. Hsieh, P. Y. Chen, and I. W. Sun, “Voltammetric study and electrodeposition of tellurium, lead, and lead telluride in room-temperature ionic liquid 1-ethyl-3-methylimidazolium tetrafluoroborate,” *Electrochim. Acta.*, vol. 137, pp. 49-56, 2014.
27. A. K. Satpati, and A. V. R. Reddy, “Electrochemical study on corrosion inhibition of copper in hydrochloric acid medium and the rotating ring-disc voltammetry for studying the dissolution,” *Int. J. Electrochem.*, vol. 2011, pp. 1-8, 2011.
28. A. M. Gustafsson, F. Björefors, B. M. Steenari, and C. Ekberg, “Investigation of an electrochemical method for separation of copper, indium, and gallium from pretreated CIGS solar cell waste materials,” *Sci. World J.*, vol. 2015, pp. 1-11, 2015.
29. H. K. Lin, X. Wu, and P. D. Rao, “Cathodic behaviour of antimony (III) species in chloride solutions,” *J. Appl. Electrochem.*, vol. 24, pp. 758-766, 1994.
30. J. T. Kuo, B. J. Kim, S. A. Hara, C. D. Lee, C. A. Gutierrez, T. Q. Hoang, and E. Meng, “Novel flexible Parylene neural probe with 3D sheath structure for enhancing tissue integration”, *Lab. Chip.*, vol. 13, pp. 554-561, 2013.

CHAPTER 5: CHARACTERIZATION OF SYNTHESIZED POLYPROPYLENIMINE TETRA (5-(2-THIENYL)SALICYLALDIMINE) FIRST GENERATION DENDRIMER (PPI)

This chapter focuses on characterization of 5-(2-thienyl)salicylaldehyde and PPI organic materials which were synthesized via Suzuki coupling reaction and Schiff base condensation respectively by UV-Vis spectroscopy, FTIR, XRD, NMR, HR-TEM and electrochemical techniques such as CV and SWV.

5.1 UV-Vis spectroscopy Characterization

The UV-Vis absorption properties were investigated in chlorobenzene as a solvent. Figure 5.1(A) shows the absorption properties of 5-(2-thienyl)salicylaldehyde which was synthesized via Suzuki coupling and its precursors 2-thienylboronic acid and 5-bromosalicylaldehyde. The UV-Vis absorption properties were studied from 285 nm to 600 nm. The spectrum of 5-bromosalicylaldehyde shows a band at 344 nm which is due to $n \rightarrow \pi^*$ transition from the C = O of the aldehyde group and $\pi \rightarrow \pi^*$ transition due to benzene ring does not appear since its absorption occur at shorter wavelength than 285 nm [1]. The absorption spectrum of 2-thienylboronic acid shows no absorption bands since its absorption bands appears at a wavelength lower than 285 nm according to work done by Sachan *et al.* [2]. After synthesizing 5-(2-thienyl)salicylaldehyde, two absorption bands appear at 293 nm due to $\pi \rightarrow \pi^*$ transition of C = C from aromatic rings (thiophene and benzene) and 367 nm due to $n \rightarrow \pi^*$ transition of C = O from aldehyde group. The $\pi \rightarrow \pi^*$ and $n \rightarrow \pi^*$ transitions bands show a bathochromic shift (red shift) on 5-(2-thienyl)salicylaldehyde spectrum as compared to on 5-bromosalicylaldehyde spectrum. This shift is due to an increase in π -conjugated bonds which are increased by introduction of thiophene on salicylaldehyde. On figure 5.1(B), poly (propylenimine) tetramine G1 dendrimer shows no absorption band while

PPI shows absorption bands at 295 nm due to $\pi \rightarrow \pi^*$ transition of $C = C$ from aromatic rings (thiophene and benzene) and 350 nm due to $n \rightarrow \pi^*$ transition of newly formed $C = N$. The $n \rightarrow \pi^*$ from PPI spectrum shows a hypochromic (blue shift) as compared to on 5-(2-thienyl)salicylaldehyde spectrum. This shift indicate a change from $C = O$ to $C = N$.

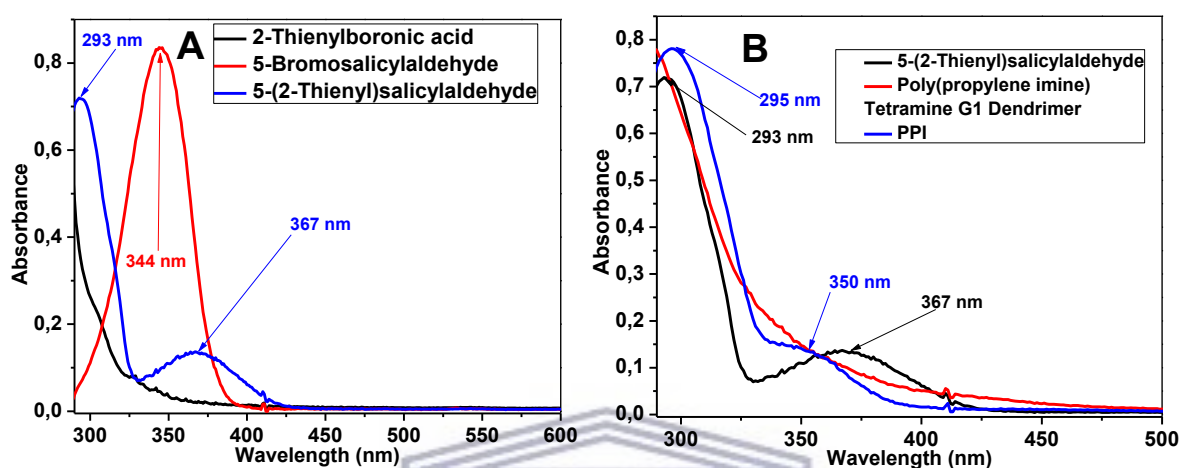


Figure 5. 1: UV-Vis spectra of (A) 2-Thienylboronic acid, 5-bromosalicylaldehyde and 5-(2-thienyl)salicylaldehyde and (B) 5-(2-thienyl)salicylaldehyde, Poly (propylenimine) tetramine G1 dendrimer and PPI.

5.2 FTIR analysis of PPI

FTIR analysis was done to check the disappearance of functional groups and appearance of new functional groups during the synthetic route of PPI. The discussion of figure 5.2(A) will be based on comparing the spectra of 5-bromosalicylaldehyde and 2-Thienylboronic acid with the spectrum of 5-(2-thienyl)salicylaldehyde, while figure 5.2(B) will be based on comparing the spectra of 5-(2-thienyl)salicylaldehyde and Poly (propylenimine) G1 dendrimer with the spectrum of PPI. The spectrum of 2-Thienylboronic acid (2) on figure 5.2(A) shows vibration bands of B – OH at 1526.50 cm^{-1} and 1340.59 cm^{-1} , B – C at 1062.45 cm^{-1} and O – H at 3270.00 cm^{-1} . These bands do not appear on the spectrum of 5-(2-thienyl)salicylaldehyde which confirms successful removal of boronic acid group. Due to the overlap from all three spectra in the range $930.00\text{ cm}^{-1} - 530.00\text{ cm}^{-1}$, it is difficult to identify

the C – Br band which is supposed to be in that range. The presence of C – H of aldehyde at 2853.00 cm^{-1} and C – S at 1082.34 cm^{-1} on spectrum 3 confirms synthesis of 5-(2-thienyl)salicylaldehyde. From Figure 12(B), spectrum 1 shows C – H at 2853.00 cm^{-1} and C – C at 1165.12 cm^{-1} of aldehyde carbon and C = O (aldehyde) at 1647.27 cm^{-1} vibration bands and spectrum 2 shows vibration bands for N – H (3372.78 cm^{-1} , 1579.86 cm^{-1} and 728.20 cm^{-1}) from the primary amines. All those bands do not appear on the spectrum 3 because the reaction took place between aldehyde and primary amine (Schiff base condensation) which results to formation of C = N (1634.98 cm^{-1}) functional group which confirms the successful synthesis of PPI. These results were discussed while referring to work done by *Gao et al.* [3], *Wang et al.* [4] and *Saleem et al.* [5].

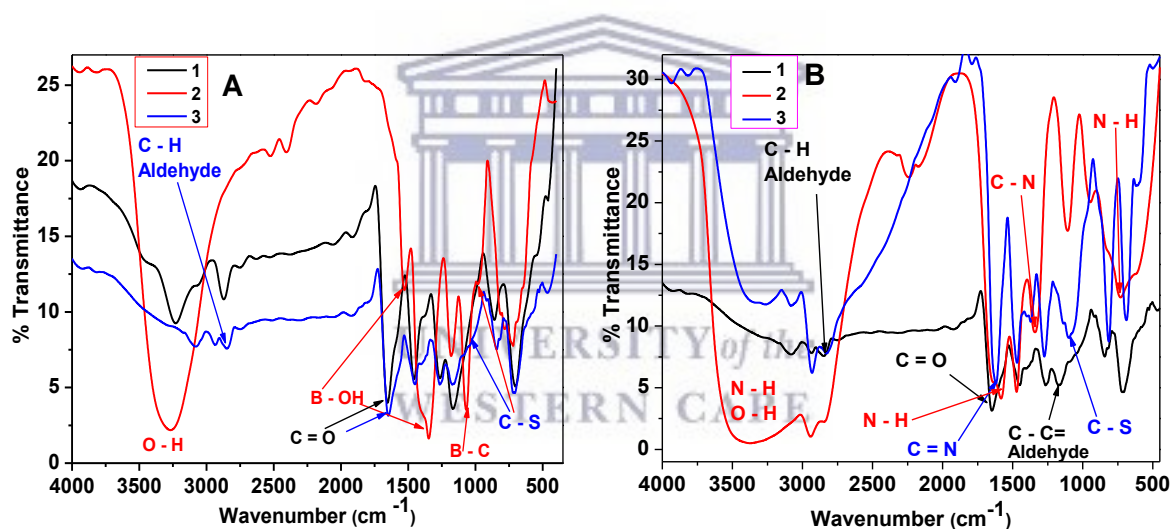


Figure 5. 2: FTIR spectra of (A) 5-bromosalicylaldehyde (1), 2-Thienylboronic acid (2) and 5-(2-thienyl)salicylaldehyde (3) and (B) 5-(2-thienyl)salicylaldehyde (1), Poly(propylenimine) G1 dendrimer (2) and PPI (3).

5.3 XRD studies of 5-(2-thienyl) salicylaldehyde and PPI

The XRD spectrum of Schiff base ligand PPI and 5-(2-thienyl)salicylaldehyde are shown in figure 5.3(A). The spectrum of 5-(2-thienyl)salicylaldehyde shows sharp reflections at 16.06°, 19.93°, 21.23°, 23.41°, 24.79°, 26.80°, 28.33° and 29.56° which indicate the formation of a crystalline compound. After Schiff base condensation took place between

poly(propylenimine) tetramine G1 dendrimer and 5-(2-thienyl)salicylaldehyde, there is a change in crystallinity of 5-(2-thienyl)salicylaldehyde which is observed by broadening of diffraction peaks on the spectrum of PPI. The PPI spectrum has poorly crystalline as compared to 5-(2-thienyl)salicylaldehyde due to the presence of poly(propylenimine) tetramine G1 dendrimer.

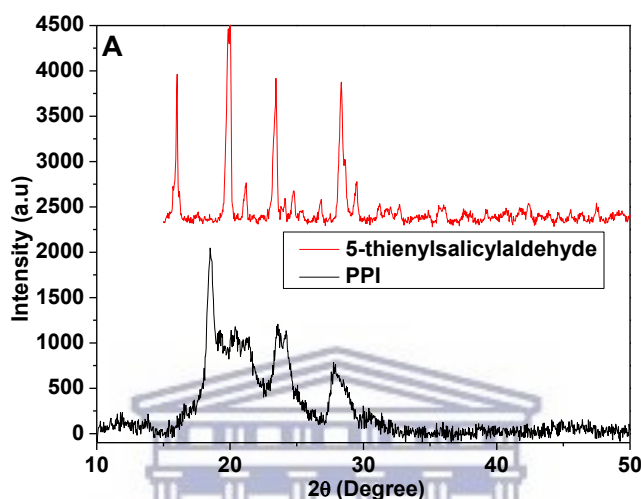


Figure 5. 3: XRD spectra of (A) 5-(2-thienyl) salicylaldehyde and PPI.

5.4 TEM and SEM analysis of PPI

The PPI were further investigated by HR – TEM. As shown on figure 5.4, the image A shows that the PPI is composed of entangled fibril structure with an average diameter of 3.30 nm. They have entangled fibril structure due the presence of G1 dendrimer [6]. Image B shows lattice fringes which indicate that synthesized PPI is crystalline. In figure 5.5(C), HR – TEM – EDX mappings of C, O and S elements in the samples shows that the elements are distributed uniformly in the entangled fibril structure. The quantitative analysis shows that the dendrimer has 93.07% C, 1.59% O, 5.14% Ni (From the grid), and 0.18% S (weight percentages). Silicon detected comes from the EDX detector lens and magnesium comes from the drying agent used during synthesis, where copper is a contamination during sample preparation.

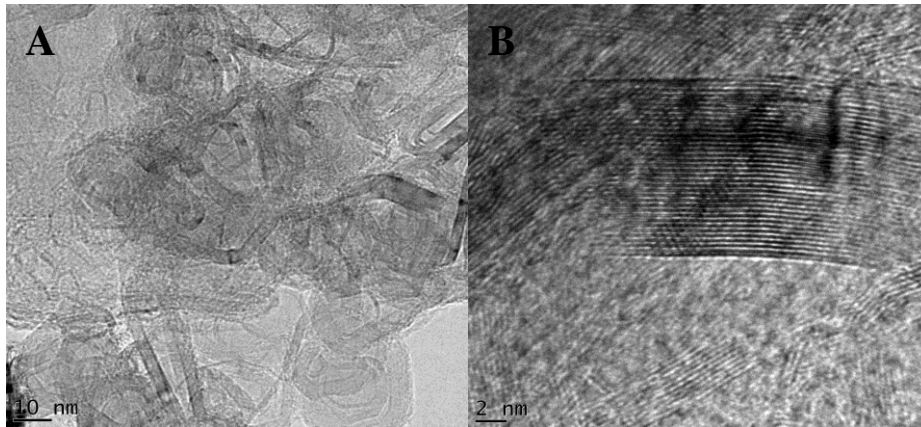


Figure 5. 4: HR-TEM images of the synthesized PPI (A and B).

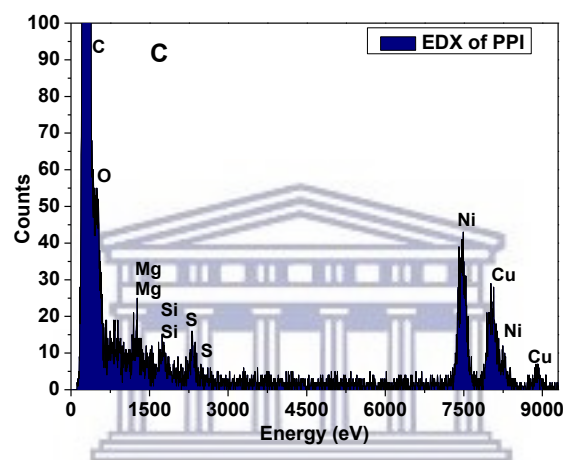


Figure 5. 5: HR-TEM-EDX of PPI.

Figure 5.6(A) shows HR – SEM image of synthesized PPI have a smooth surface. To determine if the analysed sample is PPI, HR – SEM – EDX analysis was conducted both qualitative and quantitative analysis. Figure 5.6(B) shows the elements detected from the sample. The detected elements with their weight percentages were C, 28.32% O, 2.63% Mg, 2.74% Si and 66.31% S. Quantitative analysis were not performed for carbon because carbon was detected from carbon coated the sample before analysis and carbon from the sample. Silicon is detected from the EDX lenses, while magnesium is detected from the drying agent used during synthesis of PPI.

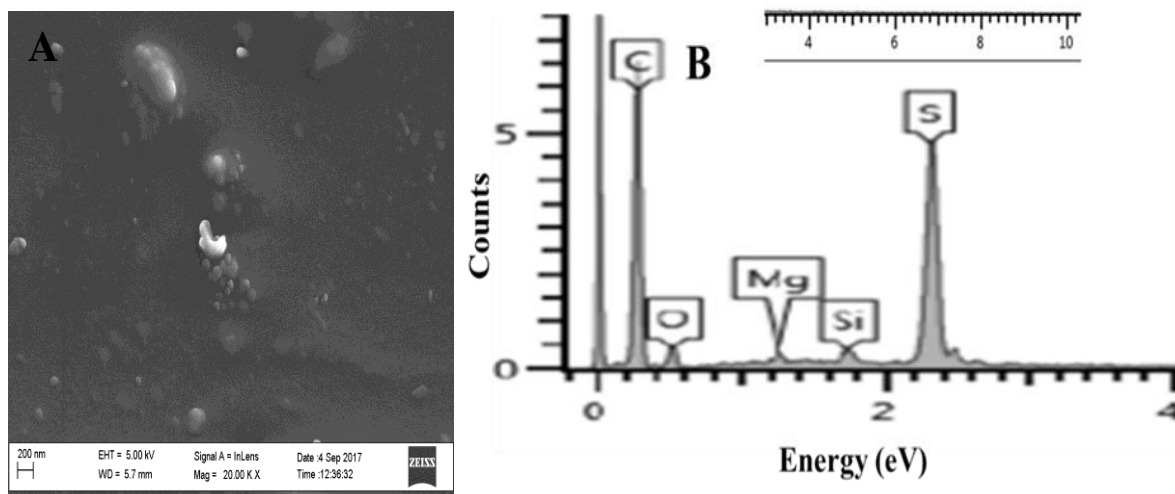


Figure 5. 6: HR-SEM images of the synthesized PPI and HR-SEM-EDX of PPI.

5.5 Electrochemical studies of PPI with cyclic voltammetry (CV) and square wave voltammetry (SWV).

The voltammograms shown on figure 5.7 were done to investigate the oxidation reduction properties of both PPI and 5-(2-thienyl)salicylaldehyde. Figure 5.7(A) shows CV of PPI and 5-(2-thienyl)salicylaldehyde. The voltammogram of 5-(2-thienyl)salicylaldehyde shows two oxidation peaks labelled at H₂ desorption and II (1000 mV) and three reduction peaks labelled as H₂ adsorption, III (-527 mV) and IV (-1010 mV). Peak II and Peak IV correspond to the formation of polarons on thiophene. The higher oxidation potential of thiophene reveals that they are better resistance to oxidation. Peak III is assign as the reduction of carbonyl group from the aldehyde. All peaks observed on a voltammogram of 5-(2-thienyl)salicylaldehyde were also observed on the voltammogram of PPI. New peak I in the voltammogram of PPI was observed which due to reduction of imines group. Figure 5.7(B) shows the SWV of both materials and it confirms the presence of all peaks observed on CV. New peak was observed at 281 mV (labelled V) which is due to the oxidation of O – H group present in the sample (from salicylaldehyde). Figure 5.7(C and D) shows the results obtained from studying the effect of scan rate. It shows that as the scan rate increases the peaks current also increases which indicate good adherence of the sample. These results were interpreted

with reference to the work done by Rawat *et al.* [7], Cui *et al.* [8], Liu *et al.* [9], and Chung *et al.* [10].

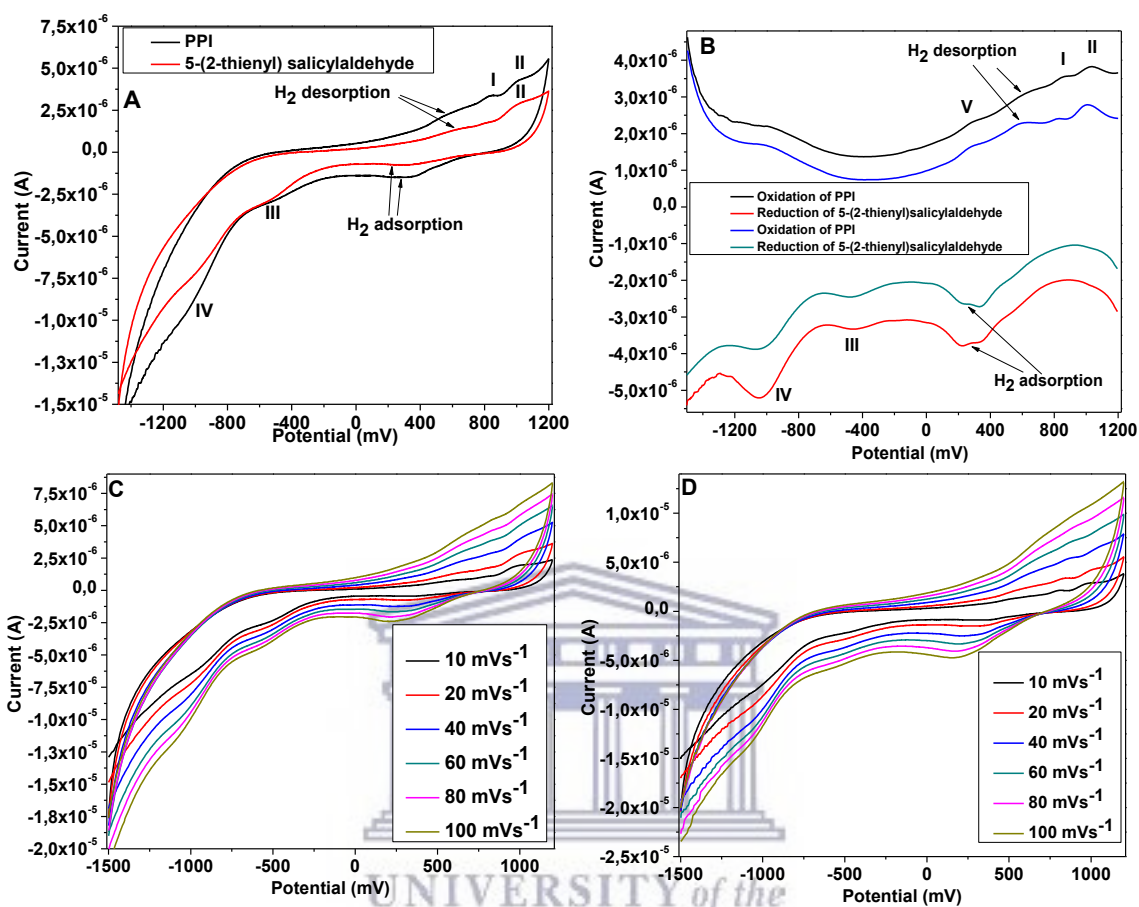


Figure 5. 7: (A) CV of 0.05 M PPI and 0.05 M 5-(2-thienyl)salicylaldehyde at scan of 10 mVs^{-1} , (B) SWV of 0.05 M PPI and 0.05 M 5-(2-thienyl)salicylaldehyde, (C) CV of 0.05 M 5-(2-thienyl)salicylaldehyde at different scan rates and (D) CV of 0.05 M PPI at different scan rates.

5.6 Sub-Conclusion

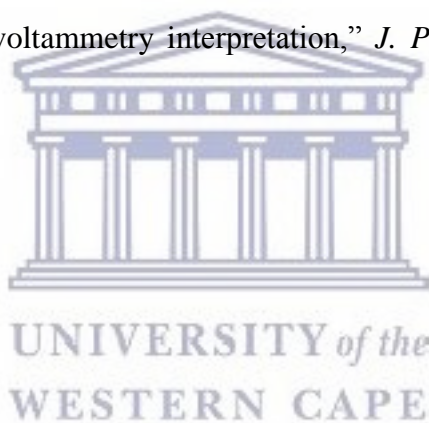
Synthesis of 5(2-thienyl)salicylaldehyde and PPI organic materials were confirmed by UV-Vis spectroscopy which showed a red shift and blue shift indicating successful introduction of thiophene on salicylaldehyde and formation of C = N respectively. FTIR showed the disappearance of boronic acid groups and C = O group. It also showed appearance of new functional group C = N. NMR confirmed their structures of 5(2-thienyl)salicylaldehyde and

PPI. XRD showed that PPI has poor crystallinity as compared to 5(2-thienyl)salicylaldehyde. HR-TEM confirmed that PPI has a fibril structure while EDX has confirmed that PPI contains C, O and S. Electrochemical studies showed that a new peak labelled I in the voltammogram of PPI which is absent on the voltammogram of 5(2-thienyl)salicylaldehyde confirms successful formation of C = N.

5.7 Reference

1. Y. Wang, H. Jiang, J. Tian, and J. He, "Spectroelectrochemistry of salicylaldehyde oxidation," *Electrochim. Acta.*, vol. 125, pp. 133–140, 2014.
2. A. K. Sachan, S. K. Pathak, L. Sinha, O. Prasad, M. Karabacak, and A. M. Asiri, "A combined experimental and theoretical investigation of 2-Thienylboronic acid: Conformational search, molecular structure, NBO, NLO and FT-IR, FT-Raman, NMR and UV spectral analysis," *J. Mol. Struct.*, vol. 1076, pp. 639–650, 2014.
3. Y. Yoa, J. Gao, F. Bao, S. Jiang, X. Zhang, and R. Ma, "Covalent functionalization of graphene with polythiophene through a Suzuki coupling reaction," *RSC. Adv.*, vol. 5, pp. 42754 - 42761, 2016.
4. M. Wang, R. Jamal, Y. Wang, L. Yang, F. Liu, and T. Abdiryim, "Functionalization of graphene oxide and its composite with poly(3,4-ethylenedioxythiophene) as electrode material for supercapacitors," *Nanoscale. Res. Lett.*, 2015.
5. M. Saleem, H. Yu, L. Wang, Z. Abdin, H. Khalid, M. Akram, N. Abbasi, and Y. Chen, "Study on synthesis of ferrocene-based boronic acid derivatives and their saccharides sensing properties," *J. Electroanal. Chem.*, vol. 763, pp. 71-78, 2016.
6. Q. Beuguel, J. Ville, J. Crepin-leblond, P. Mederic, and T. Aubry, "Influence of formulation on morphology and rheology of polypropylene/polyamide blends filled with nanoclay mineral particles," *Appl. Clay. Sci.*, vol. 147, pp. 168–175, 2017.
7. N. K. Rawat, A. Ghosal, and S. Ahmad, "Influence of microwave irradiation on

- various properties of nanopolythiophene and their anticorrosive,” *RSC. Adv.*, vol. 4, pp. 50594–50605, 2014.
8. B. Cui, T. Chen, H. Yan, D. Wang, and L. Wan, “Adlayer structures of thiophene and pyrrole derivatives on Au (111) probed by scanning tunneling microscopy,” *J. Electroanal. Chem.*, vol. 716, pp. 87–92, 2014.
 9. W. Liu, C. Gu, J. Wang, M. Sun, and R. Yang, “Electrochemistry and near-infrared electrochromism of electropolymerized polydithiophenes with β,β' -positions bridged by carbonyl or dicarbonyl substitute,” *Electrochim. Acta.*, vol. 142, pp. 108–117, 2014.
 10. D. Y. Chung, K. Lee, and Y. Sung, “Methanol electro-oxidation on the Pt surface: Revisiting the cyclic voltammetry interpretation,” *J. Phys. Chem. C.*, vol. 120, pp. 9028 - 9035, 2016.



CHAPTER 6: CHARACTERIZATION OF CuTe@PPI and CuSb@PPI CORE-SHELL NANOPARTICLES SYNTHESIZED VIA TWO-POTS AND ONE-POT METHODS

This chapter focuses on characterization of CuTe@PPI and CuSb@PPI which were synthesized via two-pots method and one-pot method. The results of CuTe@PPI and CuSb@PPI obtained by FTIR, UV-Vis, HR-TEM, HR-SEM, XRD, and electrochemical techniques (CV and SWV) are discussed below.

6.1 UV-Vis studies CuTe@PPI and CuSb@PPI core-shell NPs

UV-Vis spectroscopy can be used to study the structure and formation of complexes. To study the structural changes of PPI following its interaction with the CuTe NPs and CuSb NPs, UV – Vis absorption were performed in the wavelength range from 285 nm to 800 nm (figure 6.1(A and B)). As shown in figure 6.1(A), the spectrum of PPI shows the absorption band at 295 nm which is due $\pi \rightarrow \pi$ transitions and band at 350 nm is due to $n \rightarrow \pi^*$ transition. After the introduction of CuTe NPs, the bands show hyperchromic shift. The band at 350 nm shows red shift to 390 nm for core-shell NPs synthesized via two-pots method and 480 nm for core-shell NPs synthesized via one-pot method. This bathochromic shift indicates that the nitrogen atoms are coordinated to the CuTe NPs and the electrons are transferred from the ligand to CuTe NPs [1]. The band due to $n \rightarrow \pi^*$ shift more to longer wavelength for core-shell NPs synthesized via one-pot synthesis as compared to the ones synthesized via two-pots synthesis which indicate that PPI coordinate well when using one-pot synthesis method. This fact is also observed by high absorption of one-pot synthesized NPs as compared to two-pots synthesized core-shell NPs [2]. From figure 6.1(B), $\pi \rightarrow \pi^*$ transition band is observed at 300 nm and it shows bathochromic shift as compared to the spectrum of PPI. It does not show the band due to $n \rightarrow \pi^*$ transition on the spectrum of two-pots

synthesized core-shell NPs while it appears at 397 nm on the spectrum of one-pot synthesized core-shell NPs which also shows bathochromic shift revealing the interaction between PPI and CuSb NPs [3]. It shows a band at 702 nm which is due to the presence of CuSb NPs. The optical band gap of core-shell NPs were evaluated by plotting $(\alpha h\nu)^2$ against $h\nu$. The figure 6.2(C-F) shows the plots for the synthesized core-shell NPs with the optical band gaps found to be 1.67 eV (CuTe@PPI (Two-pots)), 1.52 eV (CuTe@PPI (One-pots)), 1.42 eV (CuSb@PPI (Two-pots)) and 1.77 eV (CuSb@PPI (One-pot)).

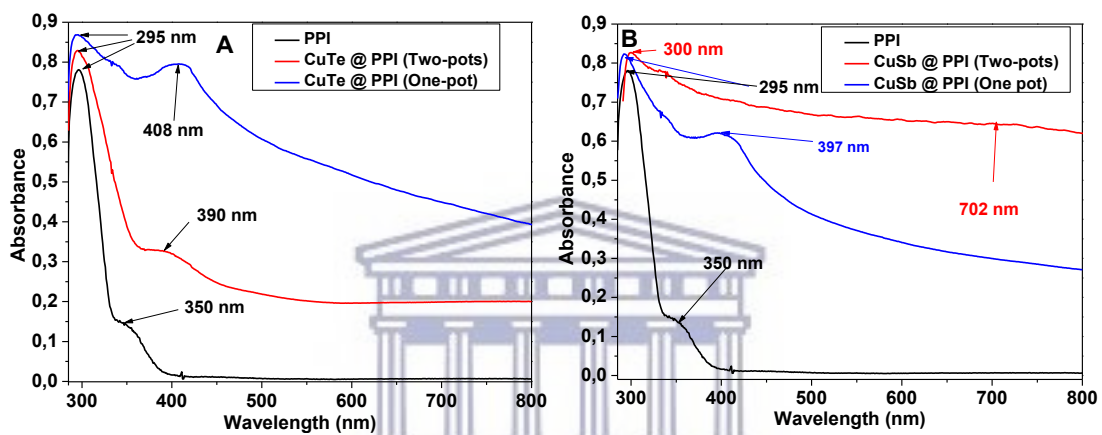


Figure 6.1 : UV-Vis spectrum of PPI compared with spectra of (A) CuTe@PPI synthesized via two-pots synthesis (red) and one-pot synthesis (blue) and (B) CuSb@PPI synthesized via two-pots synthesis (red) and one-pot synthesis (blue).

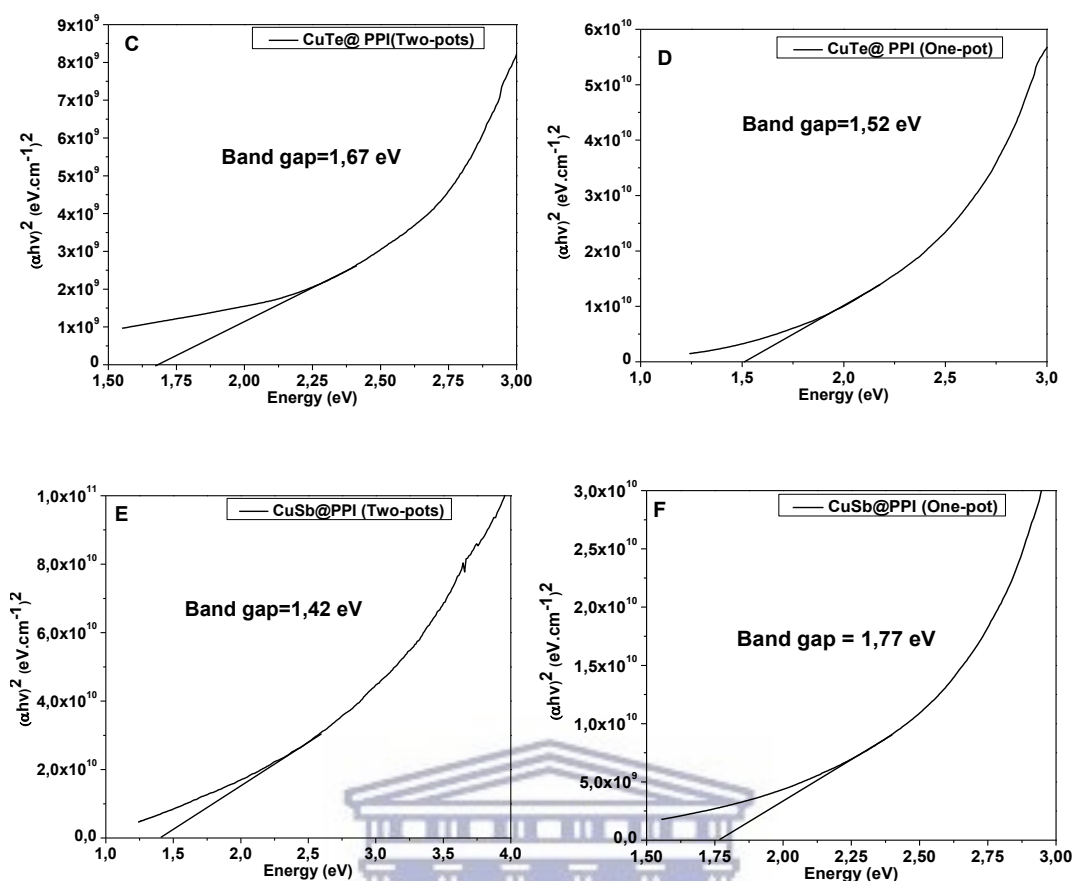


Figure 6. 2: $(\alpha h\nu)^2$ against $h\nu$ of synthesized core-shell NPs.

6.2 FTIR analysis of CuTe@PPI and CuSb@PPI core-shell NPs

Several bands were observed from the FTIR spectra of free PPI and were also observed after PPI coordinated to CuTe NPs and CuSb NPs. Figure 6.3 shows the comparison of CuTe@PPI and CuSb@PPI spectra compared with the spectrum of free PPI. Figure 6.3(A) shows that the bands are suppressed which is due to low concentration of PPI. The spectrum of PPI shows a sharp band at 1634.98 cm^{-1} due to C = N which shift to 1625.36 cm^{-1} and 1586.80 cm^{-1} due to a decrease in C = N bond order after coordination to CuTe NPs for two-pots synthesized and one-pot synthesized CuTe@PPI respectively. The O – H group also disappeared on a spectrum of one-pot synthesized core-shell NPs but still appears on the spectrum of two-pots synthesized core-shell NPs. This changes confirms successful coordination of C = N and O – H to CuTe NPs for one-pot synthesized NPs but only C = N coordinated successfully for two-

pots synthesized core-shell NPs [4]–[6]. Due to suppression of bands on spectrum of this core-shell NPs, it is difficult to identify other expected bands such as N – M and O – M. From figure 6.2(B), vibration band of C = N appears at 1628.49 cm^{-1} and 1591.43 cm^{-1} after coordination to CuSb NPs for two-pots synthesized and one-pot synthesized respectively. Disappearance of O – H group band at 3270.00 cm^{-1} in both spectra confirms coordination of O – H group to CuSb NPs. New vibration bands appeared on both spectra, which are due to O – M bond at 734.4 cm^{-1} (two-pots) and 688.0 cm^{-1} (one-pot) and also N – M bond at 513.6 cm^{-1} (two-pots) and 574.4 cm^{-1} (one-pot) where M is CuSb NPs. The appearance of these kind of vibration bands in the fingerprint region indicates the formation of CuSb @PPI core-shell NPs [7], [8].

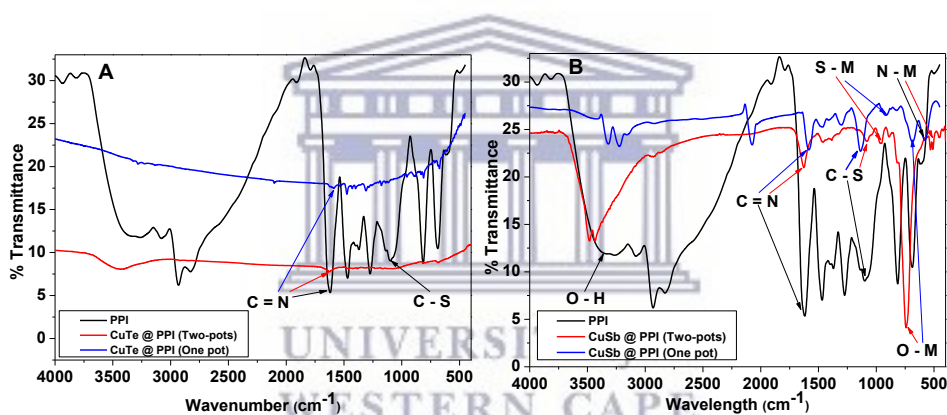


Figure 6. 3: FTIR spectrum of PPI compared with spectra of (A) CuTe@PPI synthesized via two-pots synthesis (red) and one-pot synthesis (blue) and (B) CuSb@PPI synthesized via two-pots synthesis (red) and one-pot synthesis (blue).

6.3 PL Characterization of CuTe@PPI and CuSb@PPI NPs

PL studies helps to find out structural defects in NPs. It is well known that the intensity of PL depends on density of particles in the solvent. The PL properties of synthesized core-shell NPs were studied to determine its dependence on the particle size. Figure 6.4 shows the PL spectra of the core-shell NPs obtained using different excitation wavelengths. Figure 6.4(A) shows four emission bands were two of those bands are UV emission bands (362 nm and 392

nm), one band is violet emission band (440 nm) and fourth band is blue emission band (470 nm) which does not shift as the excitation wavelength changes. Polydispersity of the core-shell NPs is observed by the broadness of bands. Figure 6.4(B) shows five emission bands were three of those bands are UV emission bands (355 nm, 377 nm and 392 nm) and other two bands are violet emission (434 nm) and blue emission (469 nm). Figure 6.4(C) shows four emission bands were two of those bands are UV emission bands (367 nm and 383 nm), other two bands are violet emission (433 nm) and blue emission (450 nm). Figure 6.4(D) shows UV emission bands at 361 nm and 379 nm. The UV emissions are known as near-band edge emissions which initiated from the recombination of free exciton through a collision process of exciton-exciton [9]. In general, it is difficult to obtain PL of metal tellurides due to magnetic interactions which turns to quench the radiation [10]. The PL spectra on figure 6.4(B, C and D) all shows blue shift when the excitation wavelength decreases. This shift is due to different particle sizes or polydispersity of the synthesized core-shell NPs [11]. Since the analysed samples are at nanometer scale, quantum confinement and surface effects becomes important and also the magnetic interactions which turn to quench the radiation are reduced [10]. As the excitation wavelength increases, the spectra (B, C, and D) shows red shifts which indicate that large NPs emits at longer wavelength than smaller NPs [12].

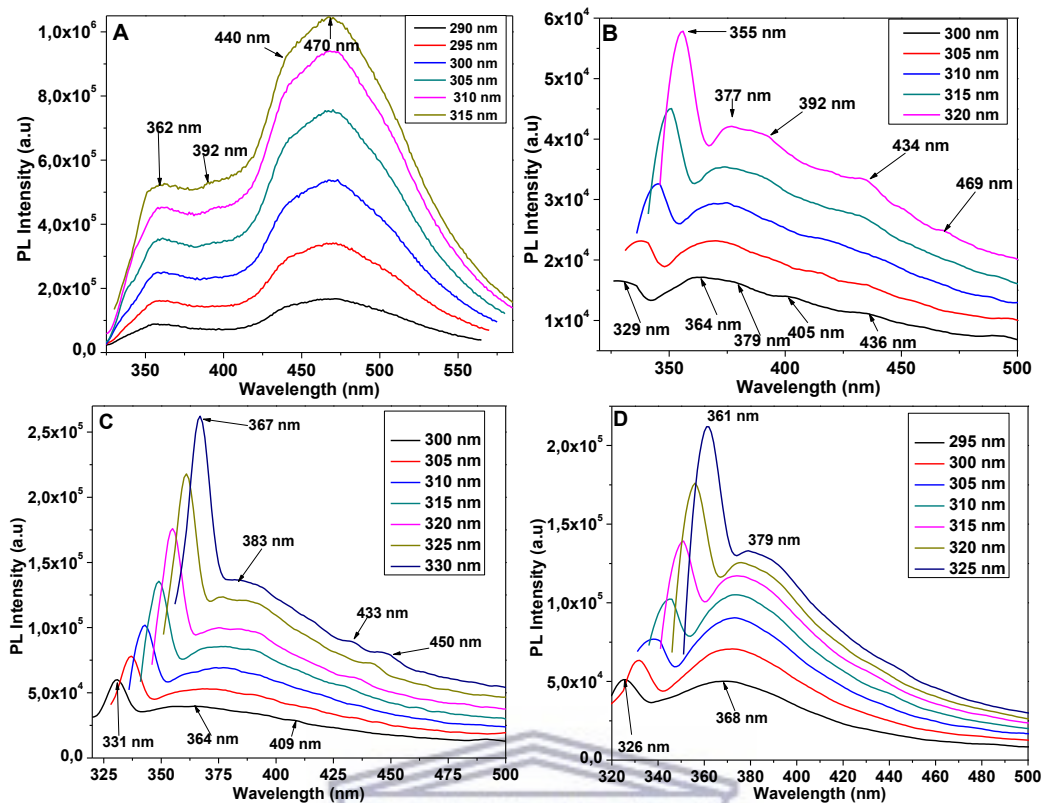


Figure 6. 4: PL spectra of CuTe@PPI synthesized via two-pots synthesis (A) and one-pot synthesis (B), CuSb@PPI synthesized via two-pots synthesis (C) and one-pot synthesis (D).

6.4 XRD characterization of CuTe@PPI and CuSb@PPI NPs

XRD was used to validate the structure of the synthesized core-shell NPs. Figure 6.5(A and B) shows the XRD patterns of CuTe@PPI and CuSb@PPI compared with the diffraction patterns of PPI and NPs (CuTe NPs and CuSb NPs). Since PPI is presence on the surface of CuTe NPs and CuSb NPs, then mixture of diffraction patterns must be obtained on the diffraction patterns of CuTe@PPI and CuSb@PPI. The diffraction patterns of CuTe@PPI and CuSb@PPI are the same as those of CuTe NPs and CuSb NPs respectively. This indicate that the thickness of PPI on the surface of NPs is not enough to be detected by XRD for core-shell NPs synthesized via two-pots method [13]. The increase in intensity of CuTe@PPI and CuSb@PPI diffraction patterns as compared to diffraction patterns of NPs (CuTe NPs and CuSb NPs) indicates that the CuTe NPs and CuSb NPs are decorated with PPI and also reveals an increase in stability of the core (CuTe NPs and CuSb NPs) [14], [15]. On figure

6.5(A) (red) significant increase appears clearly on a peak at $2\theta = 27.56^\circ$ while on figure 6.5(B) (red) all diffraction peaks shows an increase in intensity as compared to the diffraction pattern of NPs (black). Figure 6.6(C and D) shows the comparison of core-shell NPs synthesized via one-pot method and two-pots methods. Figure 6.6(C) shows that the diffraction patterns of one-pot synthesized core-shell NPs are more intense than the ones synthesized via two-pots method and the diffraction patterns of one-pot synthesized core-shell NPs shows the presence of PPI. The peaks due to the presence of PPI are marked with # symbol. According to XRD results, one-pot method gives core-shell NPs with thick shell than two-pots method. Equation 2 was used to calculate the particle sizes which were found to be 38.31 nm (two-pots) and 30.01 nm (one-pot) for CuTe@PPI and 45.11 nm (two-pots) and 41.03 nm (one-pot) for CuSb@PPI. These particle sizes were calculated using three most intense peaks from diffraction patterns.

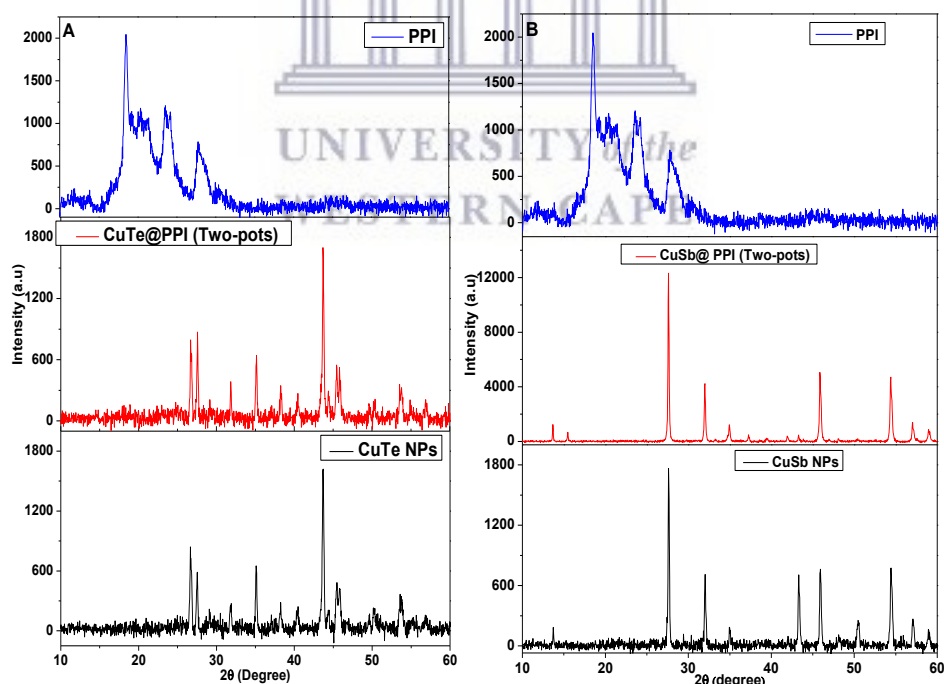


Figure 6. 5: XRD patterns showing the comparison of (A) CuTe@PPI synthesized via two-pots synthesis with patterns of CuTe NPs and PPI and (B) CuSb@PPI synthesized via two-pots synthesis with patterns of CuSb NPs and PPI.

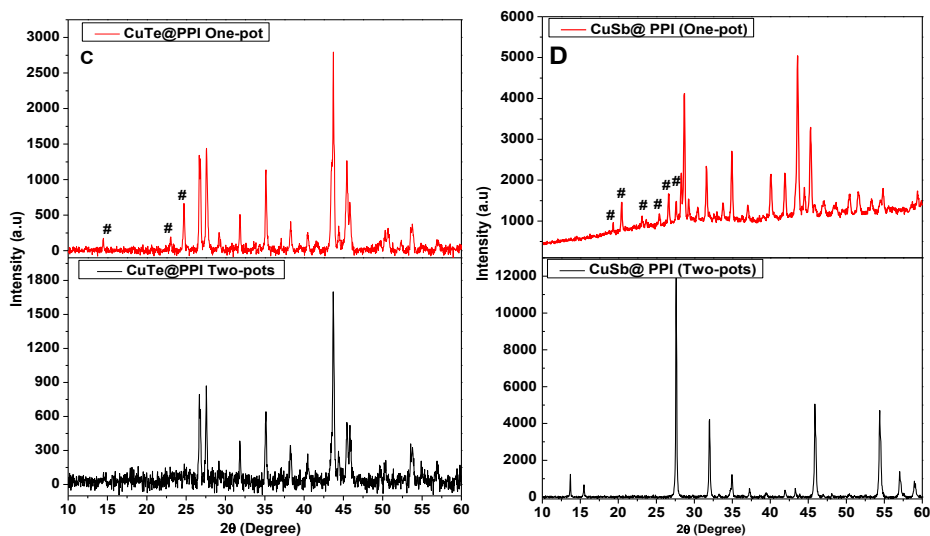


Figure 6. 6: XRD patterns C and D shows comparison of CuTe@PPI and CuSb@PPI synthesized via two-pots and one-pot methods.

6.5 HR-TEM analysis of core-shell NPs

The morphology and particles sizes of the synthesized core-shell nanoparticles were recorded by HR-TEM. Figure 6.7 shows the HR-TEM images of CuTe@PPI synthesized via two-pots (A, B, and C) and one-pot (D, E and F). Figure 6.7(A) shows that CuTe@PPI synthesized via two-pots are agglomerated which makes it impossible to determine their sizes. The presence of the shell material on the core surface can be seen on the image B labelled ii, while the core is labelled i. Thickness of the shell material was found to be 7.79 nm. Figure 6.7(C and F) shows the lattice fringes at point i which indicate that the material at that point is crystalline and at point ii shows no lattice fringes which indicate that the material at that point is poorly crystalline. From the results obtained from the XRD of CuTe NPs and PPI, reveals that the material at point i is CuTe NPs and at point ii is PPI. These confirm successful synthesis of core-shell NPs. Figure 6.7(D and E) shows the NPs produce via one-pot method are not well stable. The particles distribution obtained from figure 6.7(D) is presented in figure 6.8(G) in which the histogram of a wide particles size from 4 nm to 28 nm and gives average particle

size of 13.50 nm in diameter which not in agreement with the particle size obtained from XRD pattern. The size distribution of the NPs is described quite satisfactorily by a Gaussian function. The thickness of the shell material was found to be 1.92 nm. Figure 6.8(H and I) show the elemental analysis results which were obtained from HR-TEM-EDX for CuTe@PPI synthesized via two-pots and one-pot respectively. All of the expected element were detected (C, O, S, Cu and Te) confirming the presence of CuTe NPs and PPI. Ni is detected form the grid used, while Cl is contaminated during sample preparation and Si is detected from the lenses of the EDX.

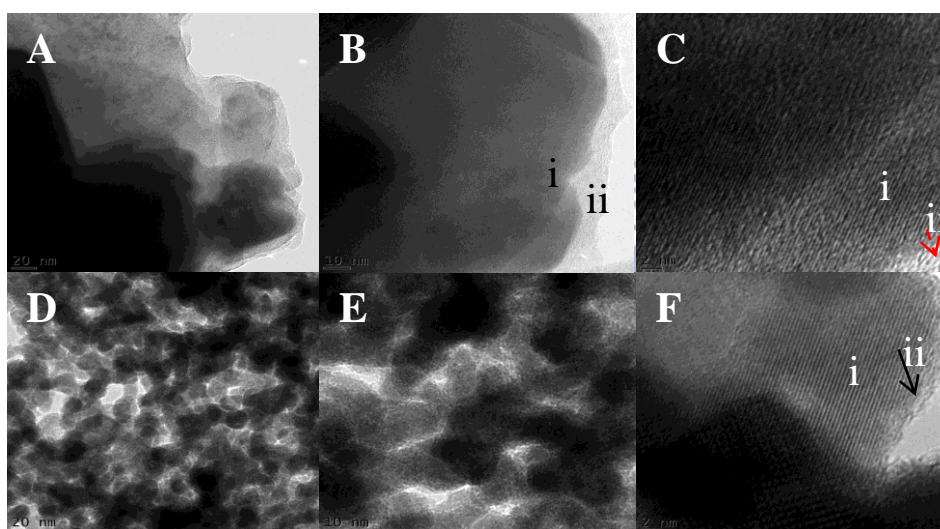


Figure 6. 7: HR-TEM images of CuTe@PPI synthesized via two-pots (A, B, and C) and one-pot (D, E and F) at different magnifications of 20 nm, 10 nm and 5 nm.

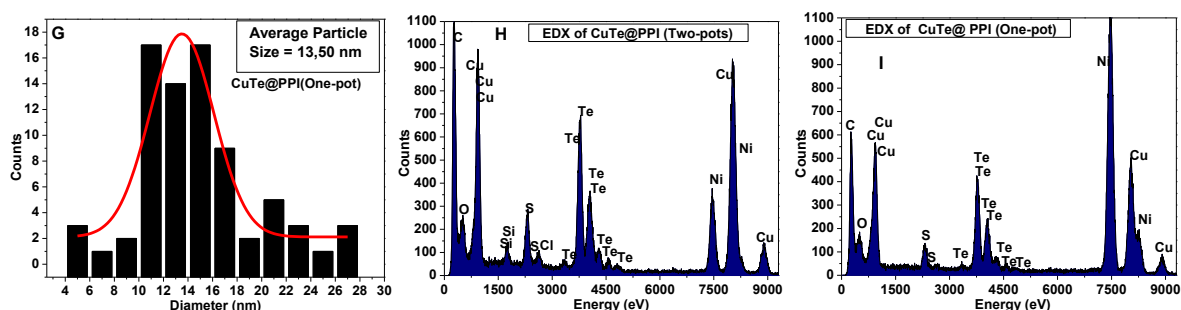


Figure 6. 8: The particle size of distribution of one-pot synthesized CuTe@PPI (G). HR-TEM-EDX of CuTe@PPI synthesized via two-pots (H) and one-pot (I).

Figure 6.9 shows the HR-TEM and EDX results for CuSb@PPI synthesized via two-pots (A, B, and C) and one-pot (D, E and F). Figure 6.9(A) and figure 6.9(D) shows that the synthesized NPs are stable since they are well dispersed with a spherical shape. Image A and B shows that two-pots synthesized NPs were widely distributed in sizes as compared to the one-pot synthesized NPs shown by image D and E. These distribution sizes are shown by figure 6.9(G) and figure 6.9(H) which are 0.54 nm – 39.65 nm for two-pots synthesized core-shell NPs with average particle size of 7.98 nm and 5.08 nm – 20.90 nm for one-pot synthesized core-shell NPs with average particle size of 11.61 nm respectively. These results are not in agreement with the results obtained from the XRD pattern. Figure 6.10(I) and figure 6.10(J) shows the EDX results presenting the presence of C, O, S, Cu and Sb in the CuSb@PPI synthesized via one-pot but absence of S for the ones synthesized via two pots synthesis. Mg is detected from MgSO₄ as drying agent during synthesis of PPI.

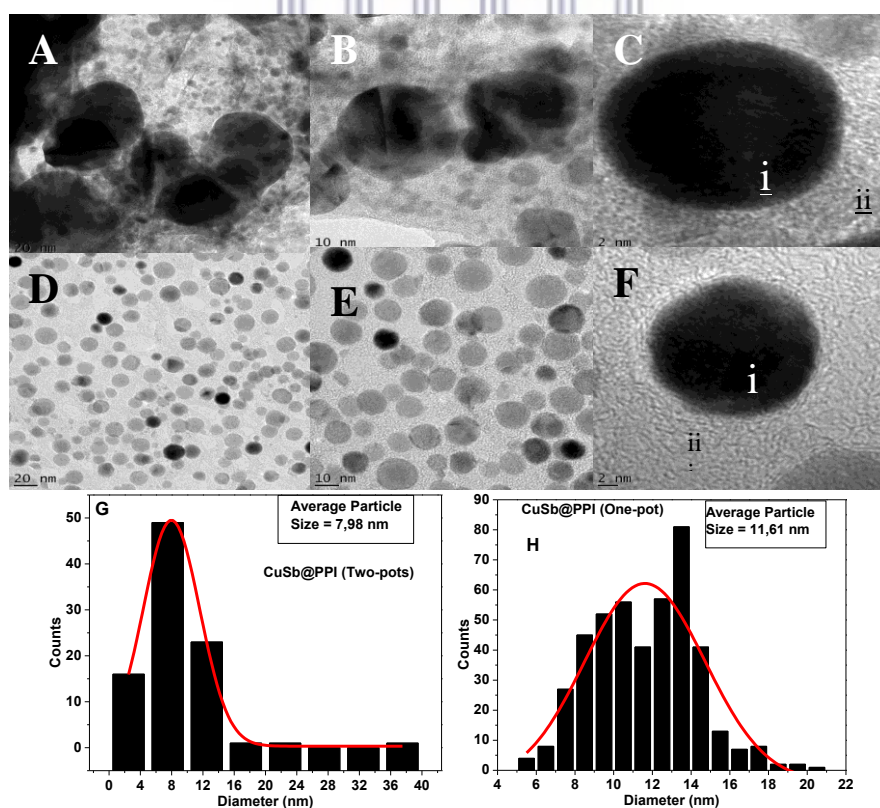


Figure 6. 9: HR-TEM images of CuSb@PPI two-pots (A, B, and C) and one-pot (D, E and F) and the particle size of distribution of CuSb@PPI (two-pots) G and (one-pot) H.

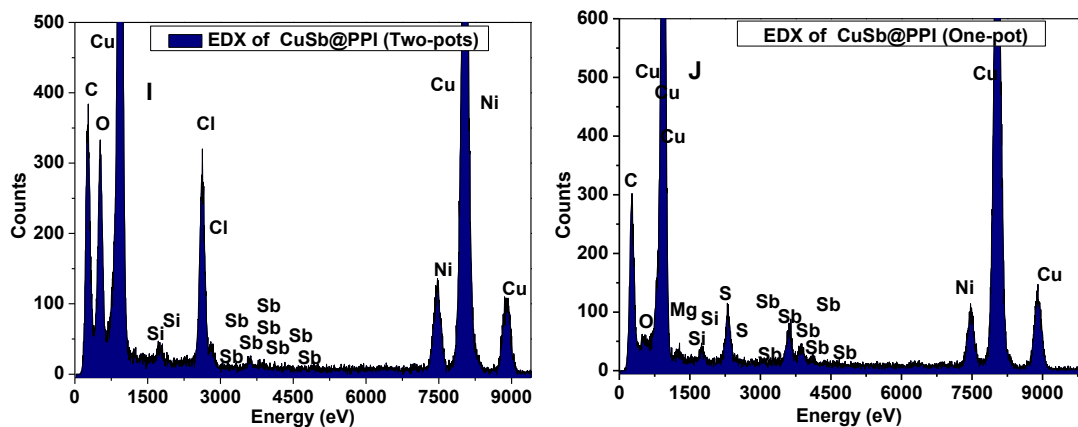


Figure 6. 10: HR-TEM-EDX of CuSb@PPI synthesized via two-pots (I) and one-pot (J).

6.6 HR - SEM Analysis of CuTe@PPI and CuSb@PPI NPs

From SEM analysis, the images of NPs (CuTe NPs and CuSb NPs) were compared with the images of core-shell NPs to check the effect of PPI on the surface of the NPs. The NPs shown on figure 6.11 image A (CuTe NPs) and image B (CuSb NPs) appear bright and rough as compared to the core-shell NPs on the images B, C, E and F. This reveals the presence of PPI on the surface of the NPs (CuTe NPs and CuSb NPs). The particle sizes were found to be 35.24 nm and 33.90nm for CuTe@PPI synthesized via two-pots and one-pot respectively and they are both widely distributed as shown on figure 6.11(G) (two-pots) and H (one-pot). These results are in agreement with the results obtained from XRD. Figure 6.11(I) and figure 6.11(J) shows a narrow particle size distributions of CuSb@PPI with the average particle sizes of 18.30 nm and 16.18 nm respectively. These results are in agreement with the results obtained from TEM.

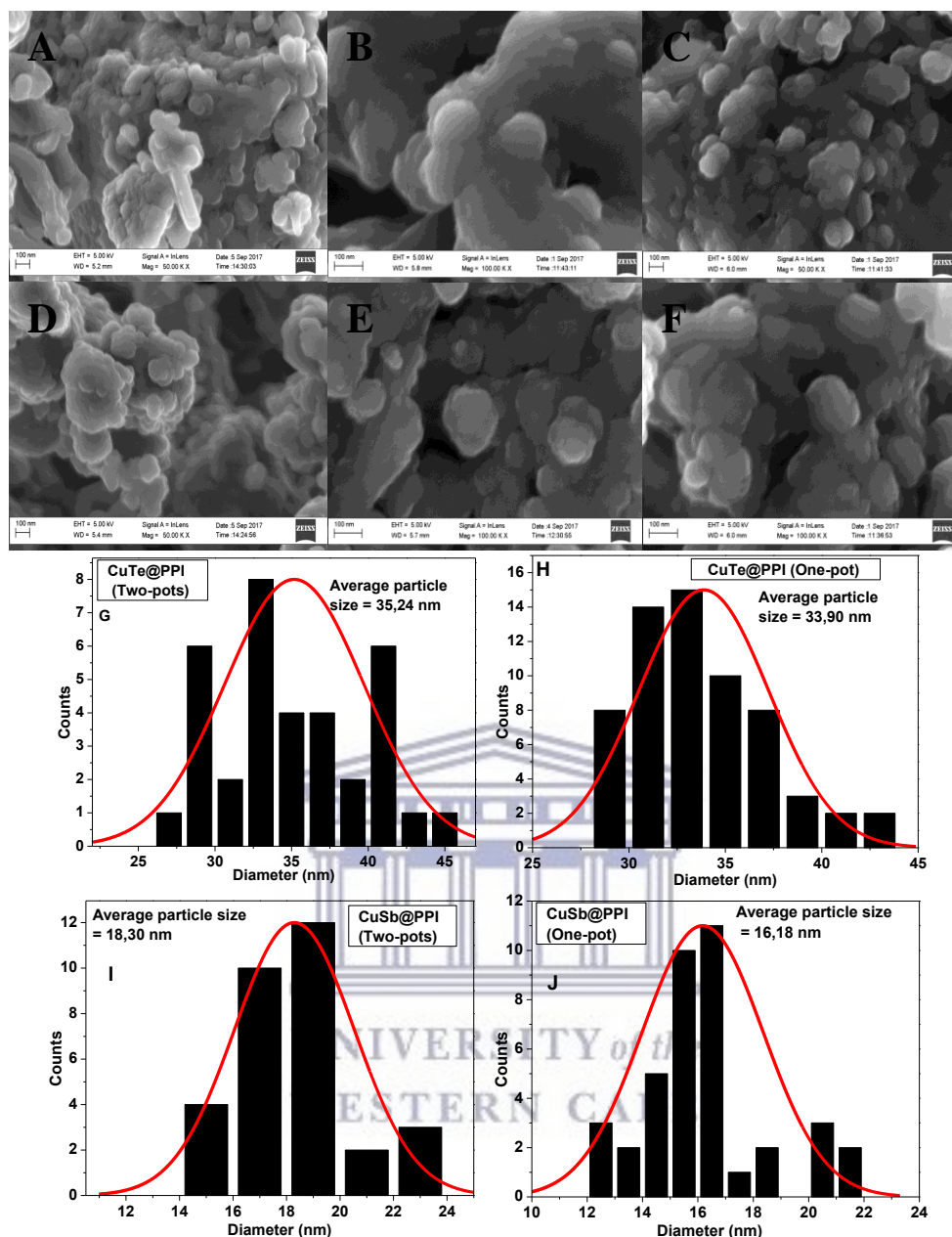


Figure 6. 11: HR-SEM images of CuTe NPs (A), CuTe@PPI synthesized via two-pots (B) and one-pot (C), CuSb NPs (D), CuSb@PPI synthesized via two-pots (E) and one-pot (F). The particle size distribution for CuTe@PPI synthesized via two-pots (G) and one-pot (H) and CuSb@PPI synthesized via two-pots (I) and one-pot (J) are shown.

6.7 EDX Analysis of CuTe@PPI and CuSb@PPI NPs

From figure 6.12(A) and figure 6.12(B) shows that the elements detected are C, O, S, Cu and Te where the presence of Cu and Te confirms the presence of the core while the presence of

C, O, and S confirms the presence of shell material. Some of the carbon detected is the one coated on the sample before analysis. The absence of S on image C confirms the absence of PPI which indicate that CuSb@PPI was not successfully synthesized via two-pots synthesis. Tantalum (Ta) has the same binding energy as nitrogen but since PPI is absent, it means it came upon during sample preparation. Image D shows all expected element which are C, O, S, Cu and Sb.

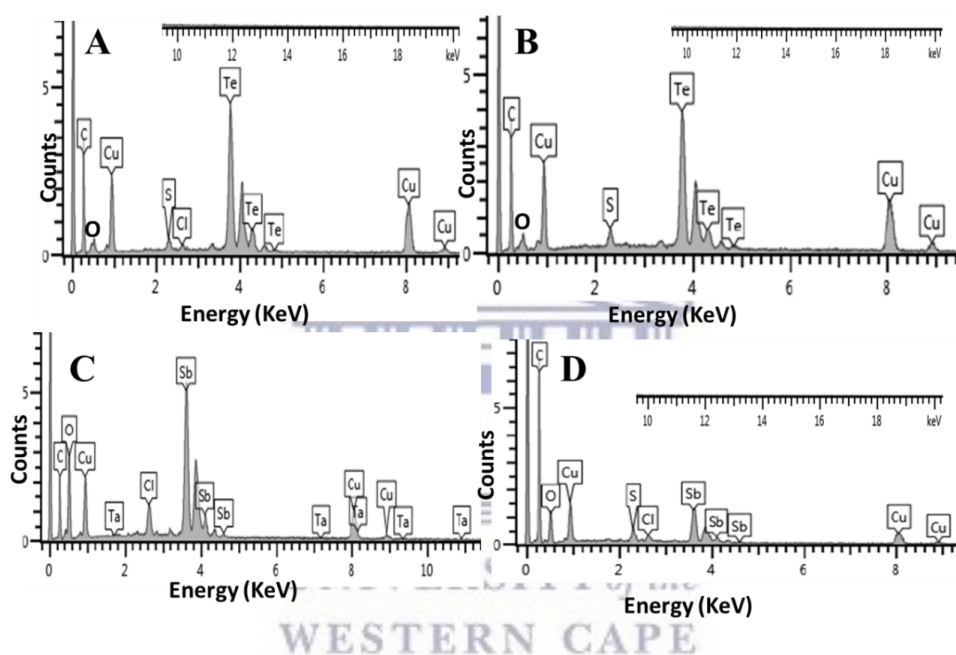


Figure 6. 12: HR-SEM-EDX of CuTe@PPI synthesized via two-pots (A) and one-pot (B) and CuSb@PPI synthesized via two-pots (C) and one-pot (D).

6.8 Electrochemical analysis of Core – Shell NPs

The electrochemical responses of CuTe@PPI were studied in 1 M H₂SO₄. Figure 6.13(A) shows an oxidation peak IV on the CV of CuTe@PPI which is absent on the voltammogram of CuTe NPs. The absence of oxidation was confirmed by SWV on figure 6.13(B). This peak confirms the presence of PPI in the synthesized core-shell NPs. Oxidation peak IV is due to the polarons formed after coordination of PPI. The reduction peaks (V and VI) from the voltammogram of CuTe NPs do not appear on the same potential as the reduction peak VII

from the voltammograms of CuTe@PPI which indicate the change in particles size and change in structure of NPs [16]. More interestingly, a crossing is observed from CuTe@PPI voltammograms when the potential scan is reverse. This cross corresponds to the reduction of species resulting from initial reduction and that are easily reduced than the parent material [17]. Figure 6.13(C) and figure 6.13(D) shows that as the scan rate increase, the oxidation peaks shift to more positive potential indicating that the reaction kinetics are well controlled by diffusion step [18].

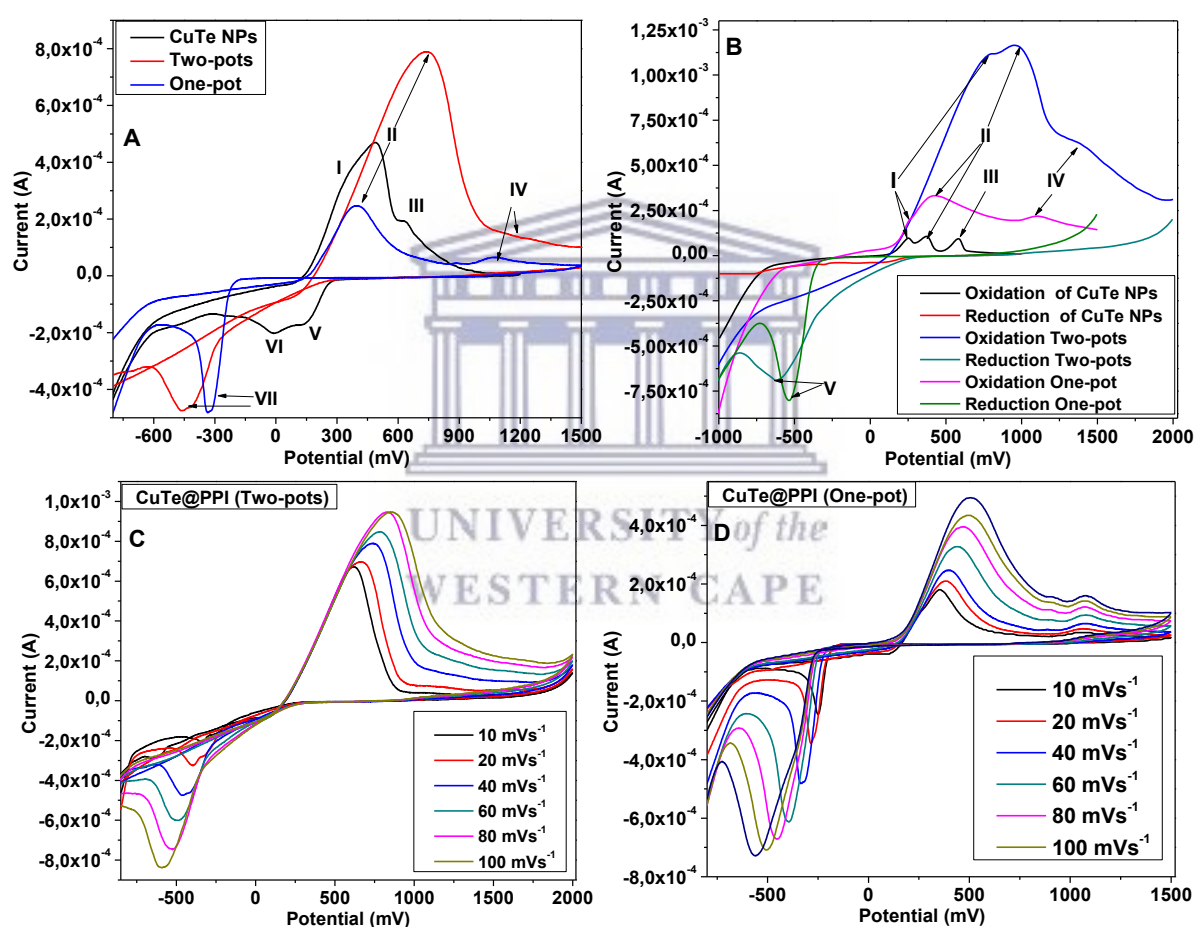


Figure 6. 13: Electrochemical responses of CuTe@PPI synthesized via two-pots and one-pot compared with electrochemical response of CuTe NPs (A and B) at scan rate of 40 mVs^{-1} , C and D shows the response of CuTe@PPI synthesized via two-pots (C) and one-pot (D) at different scan rates.

CV of CuSb NPs and CuSb@PPI synthesized via two-pots method shown on Figure 6.14(A) does not show peak III which is due to the polarons formed after coordination PPI took place. This indicates that two-pots synthesized NPs do not contain PPI meaning is just CuSb NPs. The absence of peak III was confirmed by a SWV on figure 6.14(B). Peak III only appears on the CV of CuSb@PPI which shows that it contains PPI on the surface of CuSb NPs. These results are in agreement with the results obtained from HR-TEM-EDX and HR-SEM-EDX by not detecting sulphur. The scan rate studies shown on figure 6.15(C) and figure 6.15(D) shows that as the scan rate increase the potential peak separation also increases. It also shows a directly proportional relationship between anodic peak current and the scan rate which suggest that the electrochemical behaviour of the electro-active species on the surface of the electrode is controlled by diffusion process [19], [20].

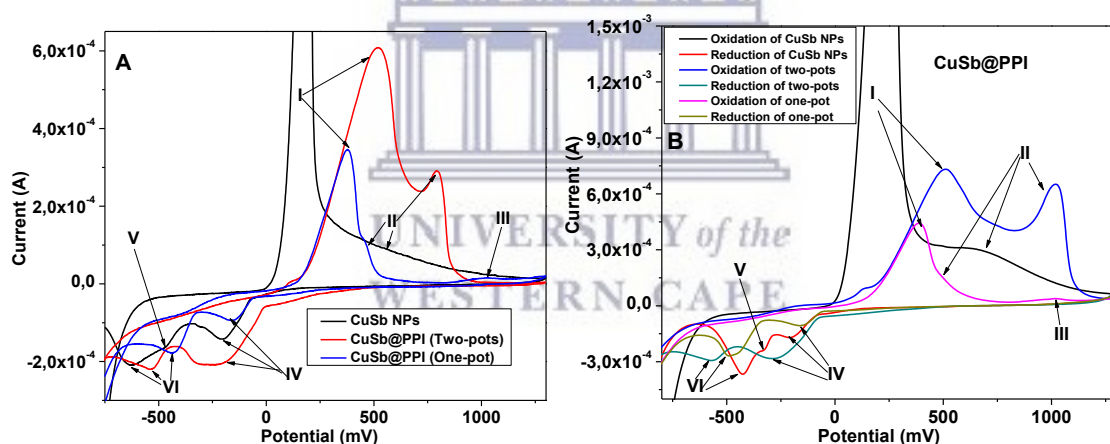


Figure 6. 14: Electrochemical responses of CuSb@PPI synthesized via two-pots and one-pot compared with electrochemical response of CuTe NPs (A and B) at scan rate of 40mVs^{-1} .

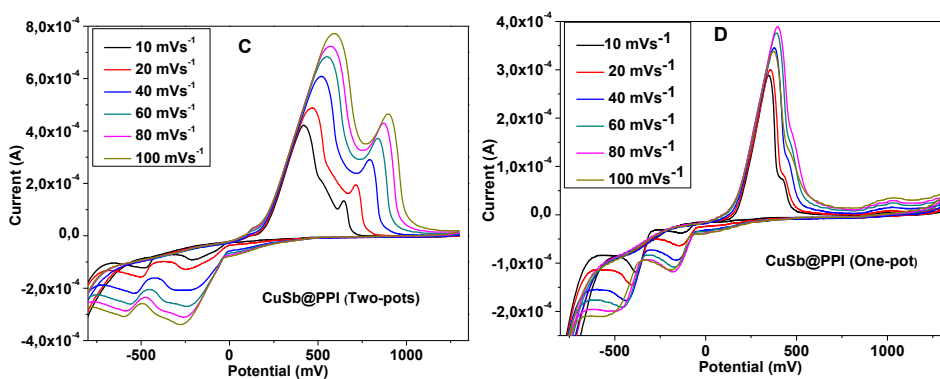


Figure 6. 15: Electrochemical responses of CuSb@PPI synthesized via two-pots (C) and one-pot (D) at different scan rates.

6.9 Determination of HOMO and LUMO energy states

CV measurements on figure 6.13 (C and D) and Figure 6.15 (C and D) were used to directly determine the HOMO and LUMO energy levels of the core-shell NPs in order to find the electrochemical energy band gap. The CV obtained at scan rate of 40mVs⁻¹ was used to determine HOMO and LUMO energy levels. Applying potentials below the HOMO energy level to form inversion layers or above LUMO to form accumulation layer can lead to abrupt emergence of anodic and cathodic currents respectively [21]. An oxidation and reduction peaks associated to electron and hole injection into the conduction and valence bands were used to find the E_{LUMO} and E_{HOMO} using the following three equations:

$$E_{LUMO} = (E_{\text{red}}^{\text{onset}} + 4.4) \text{ eV} \quad \text{Equation 3}$$

$$E_{HOMO} = (E_{\text{ox}}^{\text{onset}} + 4.4) \text{ eV} \quad \text{Equation 4}$$

$$\text{Electrochemical band gap} = E_{HOMO} - E_{LUMO} \quad \text{Equation 5}$$

Where E^{onset}_{red} and E^{onset}_{ox} are onset reduction and oxidation potentials versus the Ag/AgCl as reference electrode. The electrochemical energy band gap (E_g) is determined by taking the difference of E_{LUMO} and E_{HOMO}. Similar equations were used by S. Admassie *et al.* [22]. The table below shows the results obtained. The results obtained shows that the electrochemical

band gaps of core-shells are smaller than the optical band gaps. This difference might be due to the fast reactions which cause peaks to shift to less extreme potentials [23].

Core-shell NPs	E_{LUMO} (eV)	E_{HOMO} (eV)	E_g (eV)
CuTe@PPI Two-pots	4.13	5.77	1.64
CuTe@PPI One-pot	4.20	5.38	1.18
CuSb@PPI Two-pots	3.94	5.12	1.18
CuSb@PPI One-pot	4.08	5.29	1.21

Table 6. 1: The LUMO energies, HOMO energies and electrochemical band gaps.

6.10 Sub-Conclusion

UV-Vis spectroscopy showed that the presence of PPI on the surface of CuTe NPs and CuSb NPs improves optical properties of PPI. After coordination of PPI on CuTe NPs and CuSb NPs, the IR vibration bands of C = N shifts to a lower wavenumber confirming successful coordination. HR-TEM showed that the core material has good crystallinity as compared to the shell material which agree with the results obtained from XRD of PPI, CuTe NPs and CuSb NPs. Electrochemical studies showed a new peak labelled III which confirmed the presence of PPI indicating successful synthesis of CuTe@PPI and CuSb@PPI via two-pots method and one-pot method except for CuSb@PPI synthesized via two-pots method.

6.11 References

1. Y. Tan, Z. Zhang, Y. Liu, J. Yu, X. Zhu, D. Kuang, W. Jiang, "Synthesis , crystal structure and biological activity of the Schiff base organotin(IV) complexes based on salicylaldehyde- o -aminophenol," *J. Mol. Struct.*, vol. 1149, pp. 874–881, 2017.

2. S. Shahraki and A. Heydari, "Biointerfaces New zinc(II) N4 tetradentate Schiff base complex : A potential cytotoxic metallodrug and simple precursor for the preparation of ZnO nanoparticles," *Colloids. Surf. B.*, vol. 160, pp. 564–571, 2017.
3. G. Anbarasu, M. Malathy, P. Karthikeyan, and R. Rajavel, "Silica functionalized Cu(II) acetylacetonate Schiff base complex : An efficient catalyst for the oxidative condensation reaction of benzyl alcohol with amines," *J. Solid. State. Chem.*, vol. 253, pp. 305–312, 2017.
4. M. Sedighipoor, A. Hossein, W. Ahmad, and K. Mahmood, "Epoxidation of alkenes by an oxidovanadium(IV) tetradentate Schiff base complex as an efficient catalyst with tert -butyl hydroperoxide," *Inorganica. Chim. Acta*, vol. 457, pp. 116–121, 2017.
5. D. Elhamifar, P. Mofatehnia, and M. Faal, "Magnetic nanoparticles supported Schiff-base/copper complex : An efficient nanocatalyst for preparation of biologically active," *J. Colloid. Interface. Sci.*, vol. 504, pp. 268–275, 2017.
6. M. Shabbir, Z. Akhter, H. Ismail, and B. Mirza, "Synthetic bioactive novel ether based Schiff bases and their copper (II) complexes," *J. Mol. Struct.*, vol. 1146, pp. 57–61, 2017.
7. A. Rauf, A. Shah, K. S. Munawar, S. Ali, M. N. Tahir, M. Javed, and A. M. Khan, "Synthesis , physicochemical elucidation , biological screening and molecular docking studies of a Schiff base and its metal (II) complexes," *Arab. J. Chem.*, 2017.
8. M. Shabbir, Z. Akhter, A. Raza, H. Ismail, A. Habib, and B. Mirza, "Nickel (II) and palladium (II) triphenylphosphine complexes incorporating tridentate Schiff base ligands : Synthesis , characterization and biocidal activities," *J. Mol. Struct.*, vol. 1149, pp. 720–726, 2017.
9. L. F. Koao, F. B. Dejene, and H. C. Swart, "Effect of pH on the properties of ZnO nanostructures prepared by chemical bath deposition method," *SA. Institute. of*

- Physics.*, pp. 43–48, 2015.
10. L. Jiang, Y. Zhu, and J. Cui, “Cetyltrimethylammonium bromide assisted self-assembly of NiTe₂ nanoflakes: Nanoflake arrays and their photoluminescence properties,” *J. Solid. State. Chem.*, vol. 183, no. 10, pp. 2358–2364, 2010.
 11. S. Javad, A. Aslani, H. Motahari, and H. Salimi, “Offer a novel method for size appraise of NiO nanoparticles by PL analysis: Synthesis by sonochemical method,” *J. Saudi. Chem. Soc.*, vol. 20, pp. 245–252, 2016.
 12. V. Kravets, Z. Almemar, K. Jiang, K. Culhane, R. Machado, G. Hagen, A. Kotko, I. Dmytruk, K. Spendier, and A. Pinchuk, “Imaging of biological cells using luminescent imaging of biological cells using luminescent silver nanoparticles,” *Nanoscale. Res. Lett.*, vol. 11, pp. 1-9, 2016.
 13. B. Sarma, B. K.Sarma, “Fabrication of Ag/ZnO heterostructure and the role of surface coverage of ZnO microrods by Ag nanoparticles on the photophysical and photocatalytic properties of the metal-semiconductor system,” *Appl. Surf. Sci.*, vol. 410, pp. 557-565, 2017.
 14. A. Sakthisabarimoorathi, S. A. M. B. Dhas, and M. Jose, “Fabrication and nonlinear optical investigations of SiO₂@Ag core-shell nanoparticles,” *Mater. Sci. Semicond. Process.*, vol. 71, pp. 69–75, 2017.
 15. W. Luiz, D. Fernandes, L. Gustavo, N. Lincopan, V. Kumar, A. Benevolo, “Fabrication of polypropylene/silver nanocomposites for biocidal applications,” *Mater. Sci. Eng. C*, vol. 75, pp. 845–853, 2017.
 16. T. Jeon, S. Jong, Y. Cho, H. Park, and Y. Sung, “Electrochemical determination of the surface composition of Pd–Pt core–shell nanoparticles,” *Electrochem. commun.*, vol. 28, pp. 114–117, 2013.
 17. P. B. Taunk, R. Das, and D. P. Bisen, “Structural characterization and

- photoluminescence properties of zinc oxide nano particles synthesized by chemical route method,” *J. Radiat. Res. Appl. Sci.*, vol. 8, pp. 433–438, 2015.
18. L.J. Fu, H. Liu, H.P. Zhang, C. Li, T. Zhang, Y.P. Wu, R. Holze, and H.Q. Wu, “Synthesis and electrochemical performance of novel core/shell structured nanocomposites,” *J.elecom.*, vol. 8, pp. 1–4, 2006.
19. D. Su, Y. Zhang, Z. Wang, Q. Wan, and N. Yang, “Decoration of graphene nano platelets with gold nanoparticles for voltammetry of 4-nonylphenol,” *Carbon. N. Y.*, vol. 117, pp. 313–321, 2017.
20. I. M. Apetrei and C. Apetrei, “A modified nanostructured graphene-gold nanoparticle carbon screen- printed electrode for the sensitive voltammetric detection of rutin,” *Measurement*, vol. 114, pp. 37–43, 2018.
21. A. Bayat, “Synthesis of green-photoluminescent single layer graphene quantum dots : Determination of HOMO and LUMO energy states,” *J. Lumin.*, vol. 192, pp. 180–183, 2017.
22. S. Admassie, O. Ingan, E. Perzon, and M. R. Andersson, “Electrochemical and optical studies of the band gaps of alternating polyfluorene copolymers,” *Synth. Met.*, vol. 156, pp. 614–623, 2006.
23. S. K. Haram, B. M. Quinn, and A. J. Bard, “Electrochemistry of CdS nanoparticles : A correlation between optical and electrochemical band gaps,” *J. Am. Chem. Soc.*, vol. 123, pp. 8860–8861, 2001.

CHAPTER 7: PHOTO-PHYSICAL PROPERTIES OF CORE – SHELL NANOPARTICLES:PCDTBT COMPOSITES

For this study, synthesized CuTe@PPI and CuSb@PPI were blended with the poly [*N*-9'-heptadecanyl-2, 7-carbazole-*alt*-5, 5-(4',7'-di-2-thienyl-2',1',3'-benzothiadiazole)] (PCDTBT) in chlorobenzene. The amounts of PCDTBT added in the mixtures were kept constant while the amounts of the PPI, NPs, and core-shell NPs were varied. The resulting solutions were characterized by UV-Vis spectroscopy and Photoluminescence (PL).

7.1 UV-Vis characterization

Figure 7.1 shows the UV – Vis spectra of PCDTBT and PCDTBT blended with different materials in a weight ratio of 3:1 while the amount of PCDTBT was kept constant. The spectrum of PCDTBT (Black) shows two absorption bands II and III. Absorption band II is due to $\pi \rightarrow \pi^*$ transition, whereas absorption band III is due to a charge transfer from a donor unit of carbazole to the acceptor unit dithienylbenzothiadiazole since it is consisting of those units [1]. After blending PCDTBT and PPI with weight ratio of 3:1, the absorption band I is due $\pi \rightarrow \pi^*$ transition from aromatic rings of PPI and $n \rightarrow \pi^*$ transition band from PPI overlap with the $\pi \rightarrow \pi^*$ transition band from carbazole unit of PCDTBT. CuTe NPs and CuSb NPs in PCDTBT cause an increase in absorbance on the spectrum of PCDTBT from 650 nm to 1000 nm. While the core-shell NPs causes a new absorption band IV.

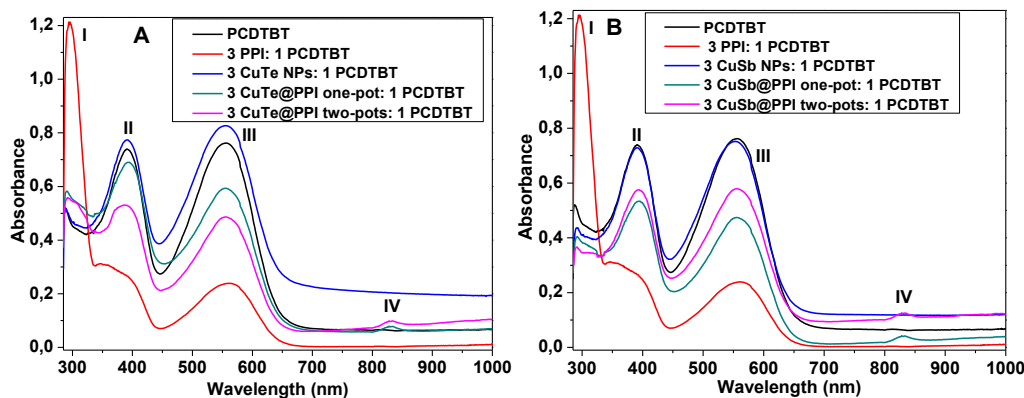


Figure 7. 1: UV-Vis spectra of PCDTBT and its composites.

Figure 7.2 shows the UV – Vis spectra of CuTe@PPI synthesized via two-pots (A) and one-pot (B) and CuSb@PPI synthesized via two-pots (C) and one-pot (D) blended with PCDTBT at different weight ratios of 1:1, 3:1, 5:1 and 10:1. At a ratio of 1:1, the absorption band IV does not appear. It starts to appear when the ratio is 3:1. As the concentration of core-shell NPs increases from 1 to 10, the absorbance of the absorption bands I, II, III and IV increases until reaches when weight ratio is 5:1 then decreases when the ratio is 10:1. This change is only observed on the CuTe@PPI (figure 7.2(A and B)) and CuSb@PPI (figure 7.2(D)) blended solutions. Figure 7.2(C) shows that as the concentration of CuSb@PPI increases, the absorbance of all absorption bands increases. This material behaves differently as compared to other materials. These results are supported by the results obtained from HR – TEM- EDX, HR – SEM – EDX and electrochemistry of CuSb@PPI (two-pots). The composite absorbs more light when the ratio is 5:1 and also shows absorption band IV. Therefore, this composite is suitable for application in photovoltaics as active layer at a ratio of 5:1.

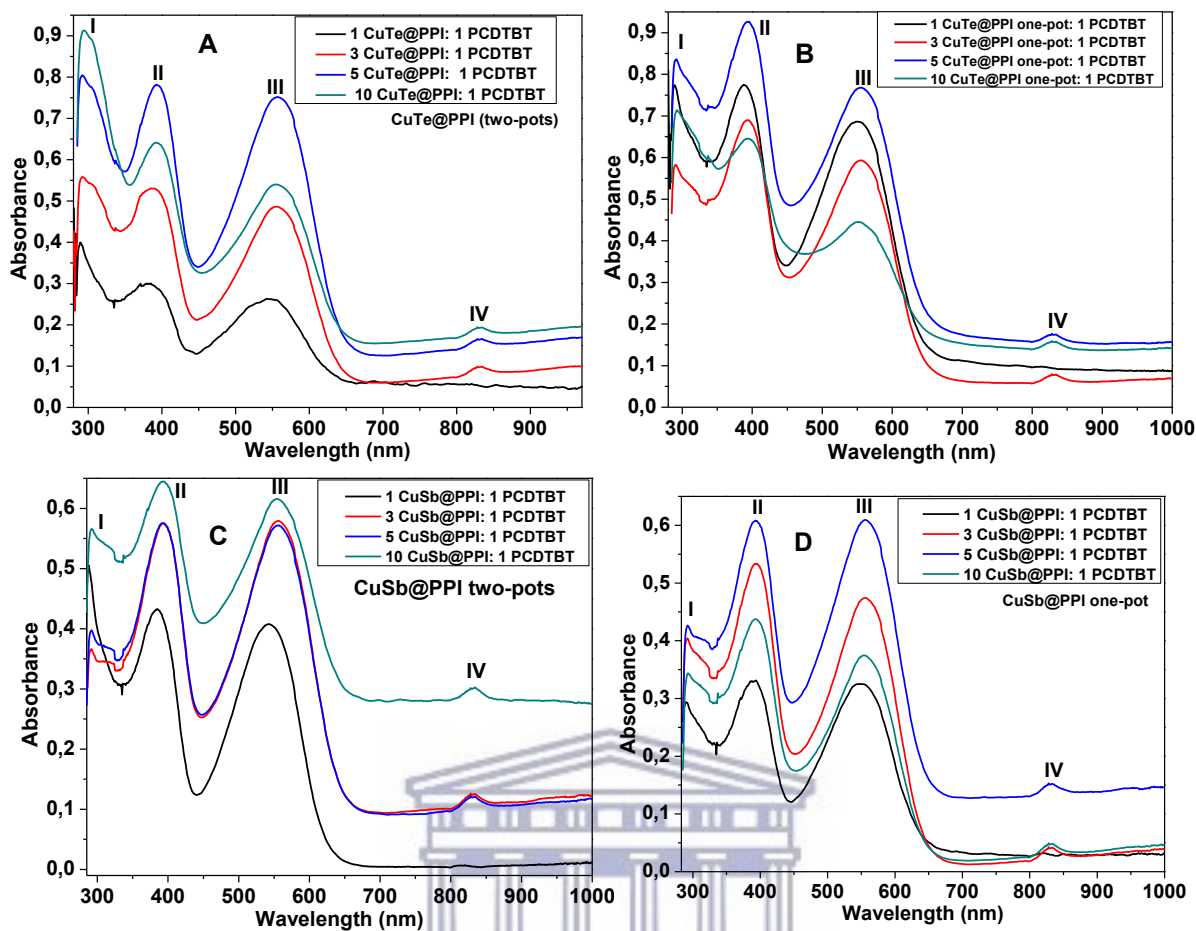


Figure 7. 2: UV-Vis spectra of PCDTBT blended with core-shell NPs at different ratios.

7.2 PL characterization

The PL emission spectra of PCDTBT composites with core-shell NPs are presented on Figure 7.3. The excitation wavelength was set at 385 nm for all samples. The PL spectra of PCDTBT and 1 core-shell NPs: 1 PCDTBT shows two bands. When the ratios are 3 core-shell NPs: 1 PCDTBT, 5 core-shell NPs: 1 PCDTBT and 10 core-shell NPs: 1 PCDTBT, four bands I, II, III and IV were observed. Bands I, II, III and IV were observed. Bands I and II are due to the presence of core-shell NPs while bands III and IV are due to the presence of PCDTBT. It can be seen from figure 7.3(A, B and C) that as the amount of core-shell NPs increase, the intensity of the bands I, II and III increases up until the ratio is 3:1 then when the ratios are 5:1 and 10:1 their intensity decreases. On figure 7.3(D), the intensity of bands I, II, and III increases up until the ratio is 5:1 then decreases when the ratio is 10:1. This indicates that as the amount of the core-shell

NPs increases, they turn to emit light up until a certain concentration then turn to serve as quenchers [2], [3].

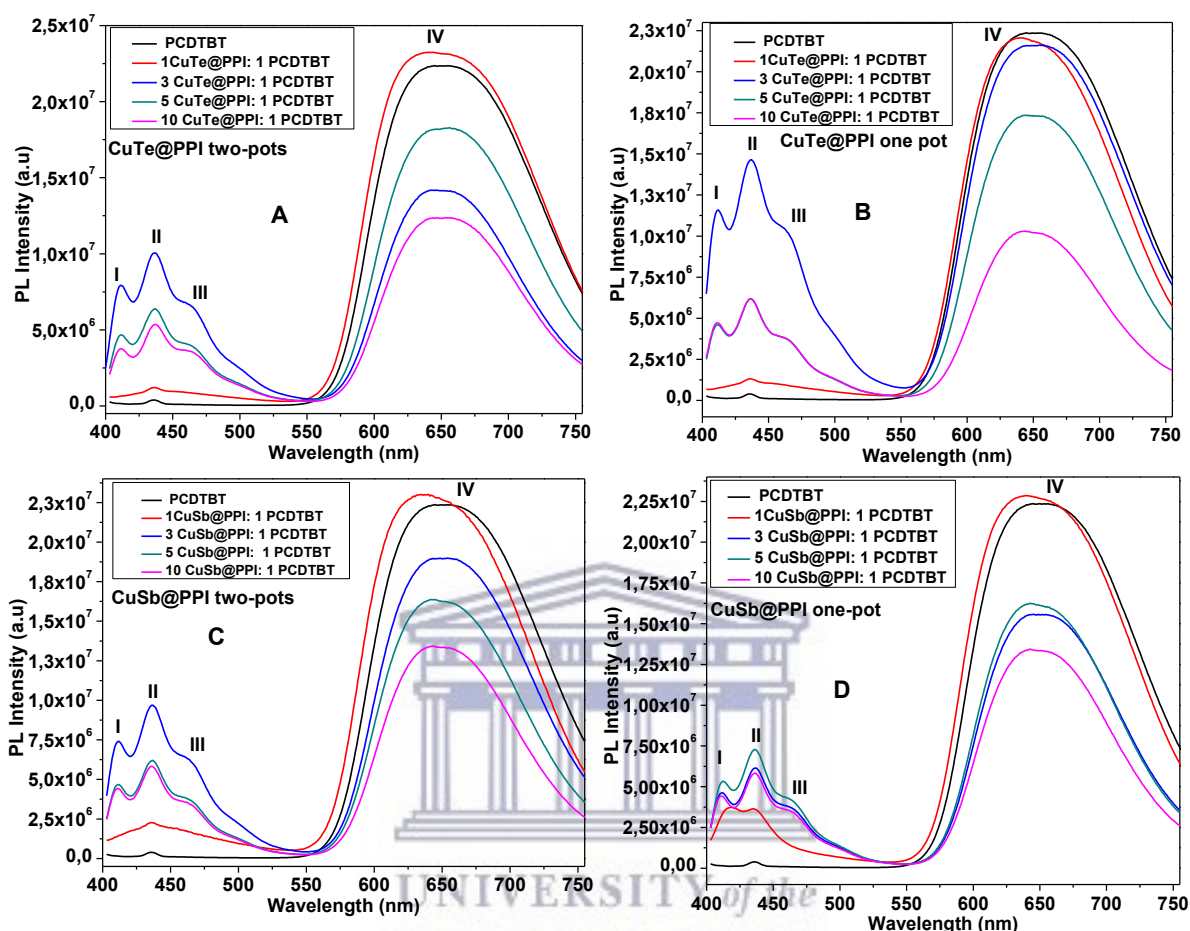


Figure 7. 3: PL emission spectra of PCDTBT blended with core-shell NPs at different ratios.

Figure 7.4 shows the PL emission spectra of core-shell NPs: PCDTBT composites at near infrared region. Three bands were observed which are labelled I, II and III. As the amounts of core-shell NPs increase, the bands show both hyperchromic and hypochromic shifts. The fluorophores re-emit intense light when the ratio is 3:1 shown in figure 7.4(A, B and C) while in figure 7.4(D) re-emit intense light when the ratio is 5:1. At the ratios above these ratios, hypochromic shift takes place.

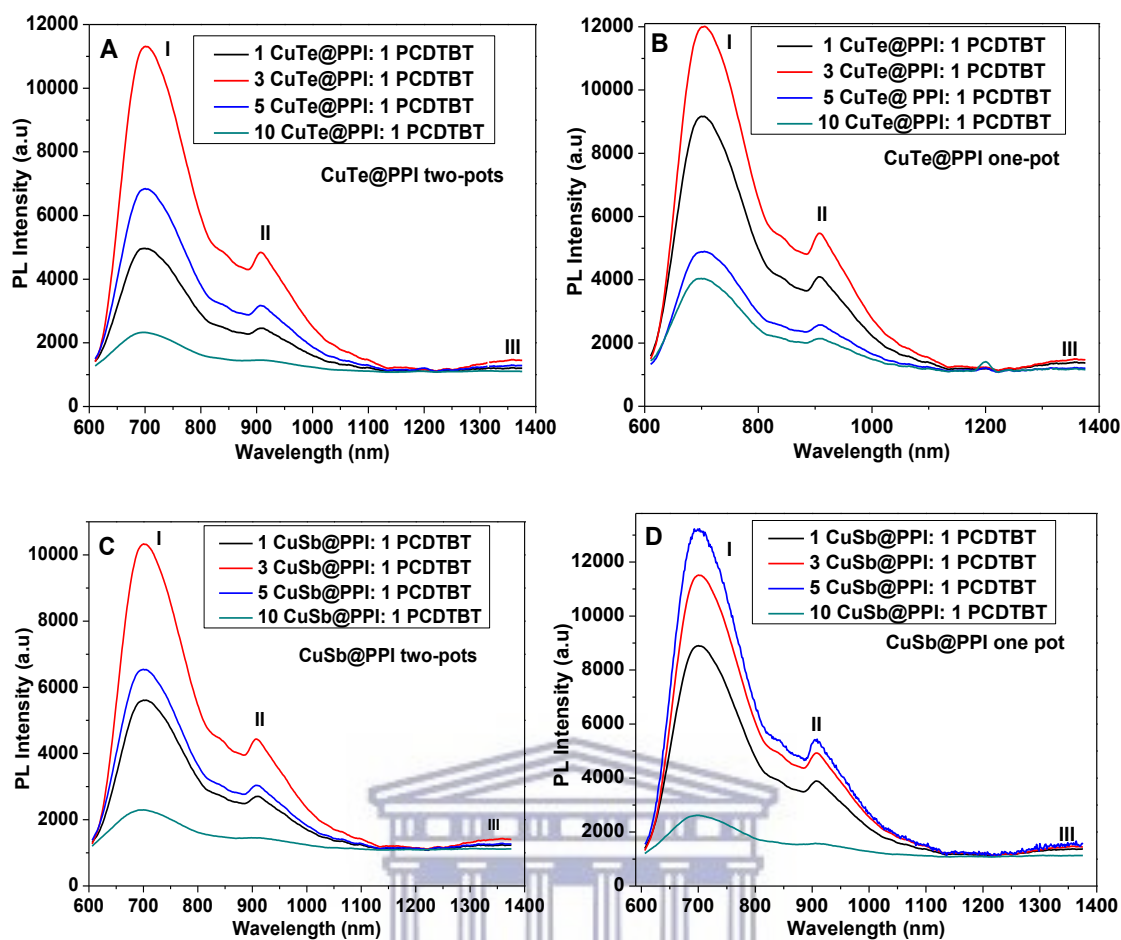
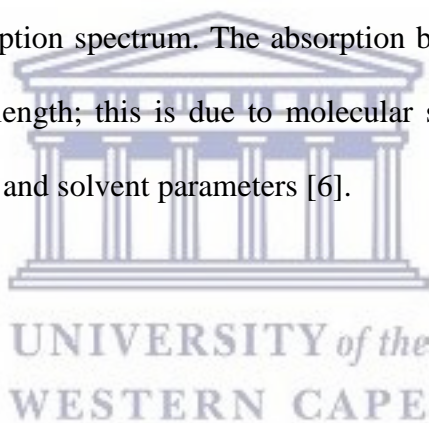


Figure 7. 4: PL (infrared) spectra of PCDTBT blended with core-shell NPs at different ratios.

7.3 Absorption, Excitation and Emission spectra

Figure 7.5 shows the absorption, emission and excitation of (A) 3 CuTe@PPI (two pots): 1 PCDTBT, (B) 3 CuTe@PPI (one-pot): 1 PCDTBT, (C) 3 CuSb@PPI (two pots): 1 PCDTBT and D) 3 CuSb@PPI (one-pot): 1 PCDTBT. The absorption spectra of all samples show four absorption bands. The 3 CuTe@PPI (two pots): 1 PCDTBT exhibited emission at 411 nm, 435 nm, 469 nm and 654 nm upon excitation at 355 nm, 369 nm, 378 nm and 526 nm with observed stokes shifts of 56 nm, 66 nm, 91 nm, 128 nm respectively. The 3 CuTe@PPI (one-pot): 1 PCDTBT exhibited emission at 412 nm, 437 nm, 465 nm and 650 nm upon excitation at 368 nm, 378 nm, 396 nm and 529 nm with observed stokes shift of 44 nm, 59 nm, 69 nm, 121 nm respectively. The 3 CuSb@PPI (two-pots): 1 PCDTBT exhibited emission at 412 nm,

435 nm, 465 nm and 648 nm upon excitation at 358 nm, 378 nm, 398 nm and 533 nm with observed stokes shift of 54 nm, 57 nm, 67 nm, 115 nm respectively. The 3 CuSb@PPI (one-pot): 1 PCDTBT exhibited emission at 411 nm, 437 nm, 467 nm and 650 nm upon excitation at 358 nm, 378 nm, 396 nm and 532 nm with observed stokes shift of 53 nm, 59 nm, 71 nm, 118 nm respectively. The absorption spectra are not the same as the excitation spectra because of the overlap of $n \rightarrow \pi^*$ transition band from PPI with the $\pi \rightarrow \pi^*$ transition band from carbazole unit of PCDTBT. Excitation spectra were mirror images of the emission spectra because for large molecules the vibration spacing in the ground state (S_0) is frequently similar to the first excited single state (S_1). The energy involved in emission is less than that of excitation and absorption, thus the emission spectrum appears at longer wavelength than excitation spectrum and absorption spectrum. The absorption bands and excitation bands do not appear at the same wavelength; this is due to molecular structure [4], the presence of heavy atoms in the solvent [5] and solvent parameters [6].



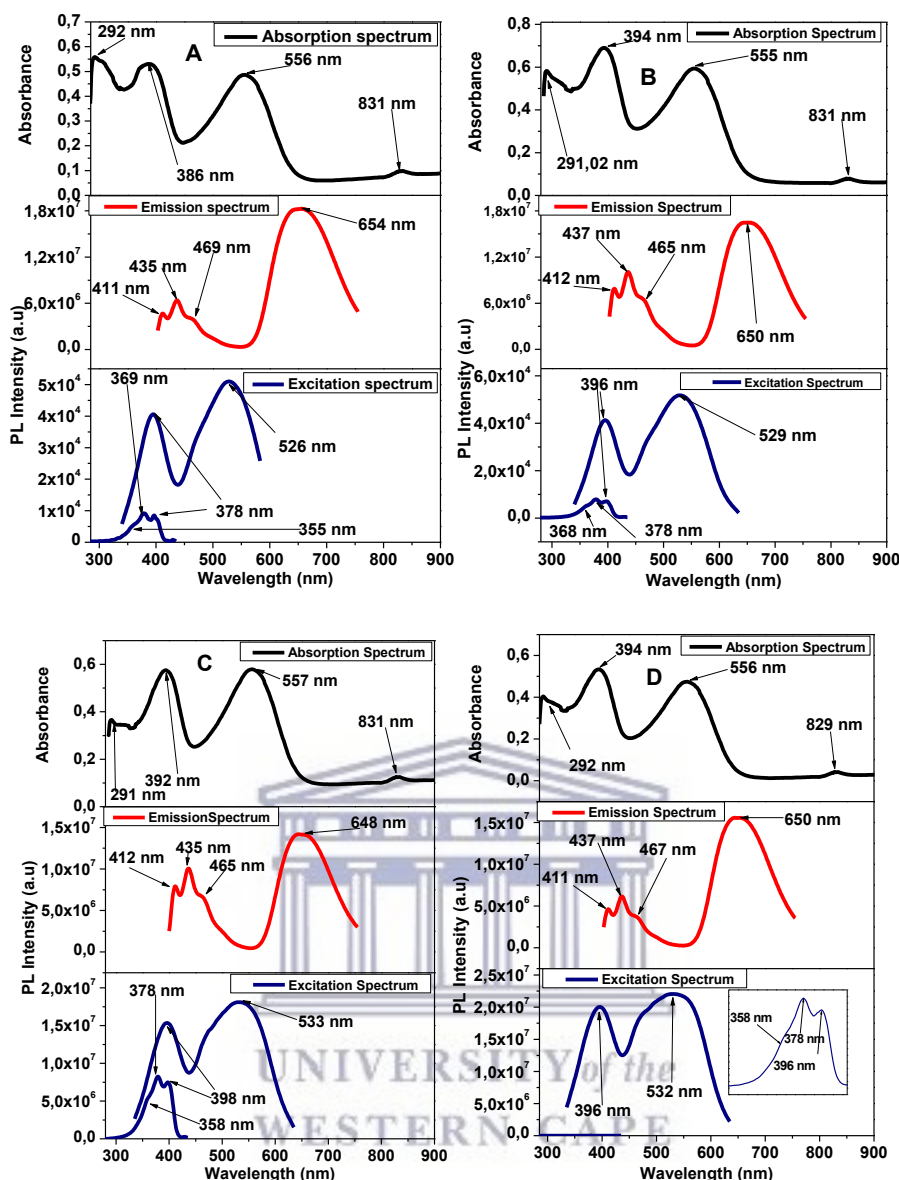


Figure 7. 5: Absorption, excitation and emission spectra for core-shell NPs: PCDTBT composite in chlorobenzene.

7.4 Sub-Conclusion

Photophysical properties of core-shell NPs: PCDTBT composites are presented in this chapter. UV-Vis spectroscopy results showed that the composite absorbs more light when the ratio is 5 core-shell: 1 PCDTBT. Therefore, this composite is good for application in photovoltaics as an active layer. In PL, the intensity increases as the quantity of CuTe@PPI and CuSb@PPI but there is no specific trend. But the ratio 10 CuTe@PPI or 10 CuSb@PPI:

1 PCDTBT has less intensity meaning that as the quantity of CuTe@PPI and CuSb@PPI increases, they turn to serve as quenchers.

7.5 References

1. P. Jhas, S. P. Koiry, V. Saxena, P. Veerender, A. K. Chauhan, A. K. Debnath, D.K. Aswal. S. K. Gu, "Air-stability and bending properties of flexible organic field-effect transistors based on poly[N-9'-heptadecanyl-2,7-carbazole-alt-5,5-(4',7'-di-2-thienyl-2',1',3'-benzothiadiazole)]", *Org. Electro.*, vol. 14, pp. 2635-2644, 2013.
2. B. Sarma, B. K.Sarma, "Fabrication of Ag/ZnO heterostructure and the role of surface coverage of ZnO microrods by Ag nanoparticles on the photophysical and photocatalytic properties of the metal-semiconductor system" *appl. Surf. Sci.*, vol.410, pp. 557-565, 2017.
3. S. Javad, A. Aslani, H. Motahari, and H. Salimi, "Offer a novel method for size appraise of NiO nanoparticles by PL analysis : Synthesis by sonochemical method," *J. Saudi. Chem. Soc.*, vol. 20, no. 3, pp. 245–252, 2016.
4. E. Kırbaç Y. Atmaca, and A. Erdoğan, "Novel highly soluble fluoro, chloro, bromo-phenoxy-phenoxy substituted zinc phthalocyanines; synthesis, characterization and photophysical properties," *J. Organomet. Chem.*, vol. 752, pp. 115-122, 2014.
5. A. Erdoğan, and M. Arıcıb, "Novel soluble octa-substituted phthalocyanines bearing chloro and long alkyl chain containing fluorine: Synthesis, characterization and photophysical and photochemical properties," *J. Fluo. Chem.*, vol. 166, pp. 127-133, 2014.
6. A. Erdoğan, M. Durmu, O. Avciata, U. Avciata, and T. Nyokong "Synthesis, photophysics, photochemistry and fluorescence quenching studies on highly soluble substituted oxo-titanium(IV) phthalocyanine complexes," *Synth. Met.*, vol. 160, pp. 1868-1876, 2010.

CHAPTER 8: CONCLUSIONS

8.1 Conclusion

In conclusion; two chemical approaches were employed for the development of core-shell NPs. CuTe@PPI core-shell NPs were successfully synthesized via one-pot method and two-pots method, while CuSb@PPI core-shell NPs were successfully synthesized via one-pot method alone according to the results obtained from spectroscopic, electron microscopic and electrochemical studies. The UV-Vis results showed that the NPs material has an effect on the optical properties of the PPI. As PPI coordinate on the surface of the NPs, the $\pi \rightarrow \pi^*$ and $n \rightarrow \pi^*$ bands shows a red shift with an increase in absorbance. FTIR showed that after coordination; the vibration band due to C=N group from PPI shift to a lower wavenumber confirming coordination. XRD showed an increase in intensity of diffraction peaks and mixture of the diffraction patterns on CuTe@PPI and CuSb@PPI diffraction patterns as compared to the diffraction patterns of CuTe NPs and CuSb NPs respectively. This increase and mixture of diffraction patterns indicates a successful decoration of PPI on the surface of CuTe NPs and CuSb NPs. HRTEM showed that the CuTe@PPI synthesized via one pot method have an average particles size of 13.60 nm while for CuTe@PPI synthesized via two pots showed aggregation which made it impossible to determine average particles size. CuSb@PPI synthesized via two pots method and one pot method has an average size of 7.98 nm and 11.61 nm respectively. HRSEM showed that the average particle sizes are 35.24 nm for CuTe@PPI two pots method, 33.90 nm for CuTe@PPI one-pot method, 18.30 nm for CuSb@PPI two pots method, and 16.18 nm for CuSb@PPI one-pot method. PL showed broad bands which indicates a wide particles size distribution of core-shell NPs. HRTEM-EDX and HRSEM-EDX showed that CuSb@PPI two-pots method were unsuccessfully synthesized due to the absence of sulphur from the thiophene group of PPI on the spectrum. Electrochemistry was used for qualitative analysis. They confirmed successful synthesis core-

shell NPs by showing a new peak (IV) which is due to polarons of PPI formed coordination. This new peak indicates successful decoration of PPI on the surface of CuTe NPs and CuSb NPs while for CuSb@PPI (two-pots) no new peak was observed. The core-shell NPs were blended with PCDTBT in chlorobenzene as a solvent with different ratios and their photophysical properties were studied. PL showed that when the ratio is 10 core-shell NPs:1 PCDTBT less light is emitted as compared to other ratios indicating that core-shell NPs turn to serve as quenchers. The UV-Vis spectrum of the Core-shell NPs:PCDTBT composition showed an increase in absorbance and a new UV-Vis band at ~830 nm which indicate a good characteristic for this composite be used in photovoltaics.

8.2 Future work

- 8.2.1 Use the LUMO level of the acceptor and HOMO level of the donor to estimate the maximum open-circuit voltage of the device.
- 8.2.2 Construction photovoltaic cells to investigate the performance of Core-shell NPs:PCDTBT as an active layer.
- 8.2.3 Use fluorescence to determine the fluorescence quantum yields and fluorescence lifetime of the synthesized materials and active layer (Core-shell NPs:PCDTBT).

8.3 Recommendations

- 8.3.1 XPS analysis to determine chemical information about the surface of the core-shell NPs. Determine both the quantitative information about the amount of element present on the surface of core-shell NPs and chemical states of elements on the surface of core-shell NPs which may lead to determination of elements that coordinate to CuTe NPs and CuSb NPs.
- 8.3.2 Thermo-gravimetric analysis-FTIR (TGA-FTIR) to determine the weight loss of synthesized materials (PPI, CuTe NPs, CuSb NPs and core-shell NPs) caused by

degradation as a function of temperature while FTIR provide information the functional groups that evolve as gas during degradation.

8.3.3 Parameters such as blending time, temperature and solvent are investigated in order to notice their effect on the optical properties of the blended composites.

8.4 Appendix

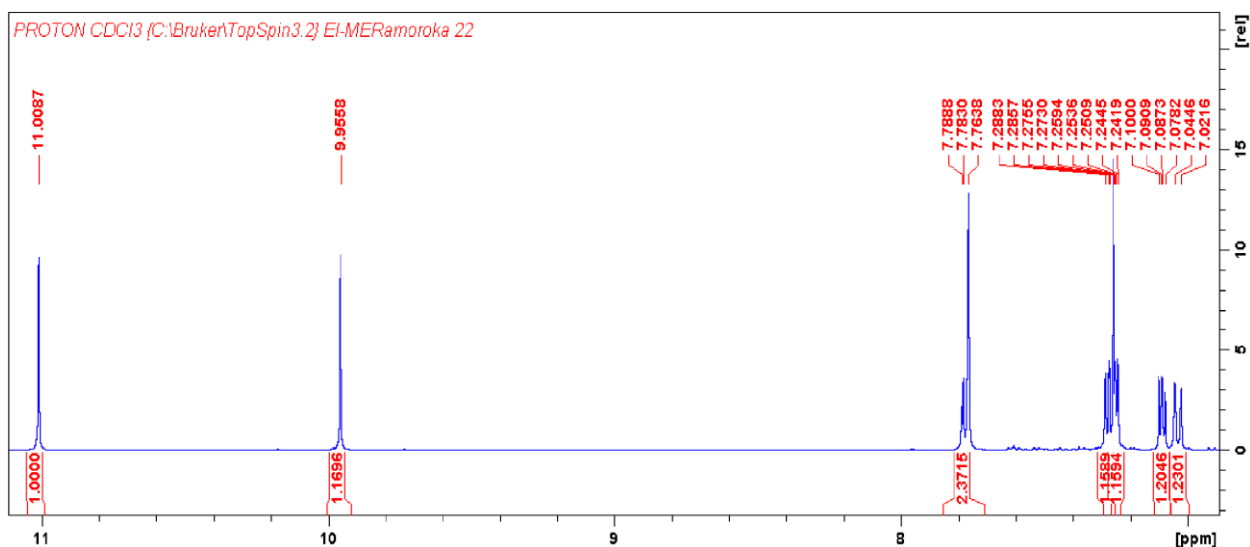


Figure 8.1: ¹H-NMR spectrum of 5(2-thienyl)salicylaldehyde

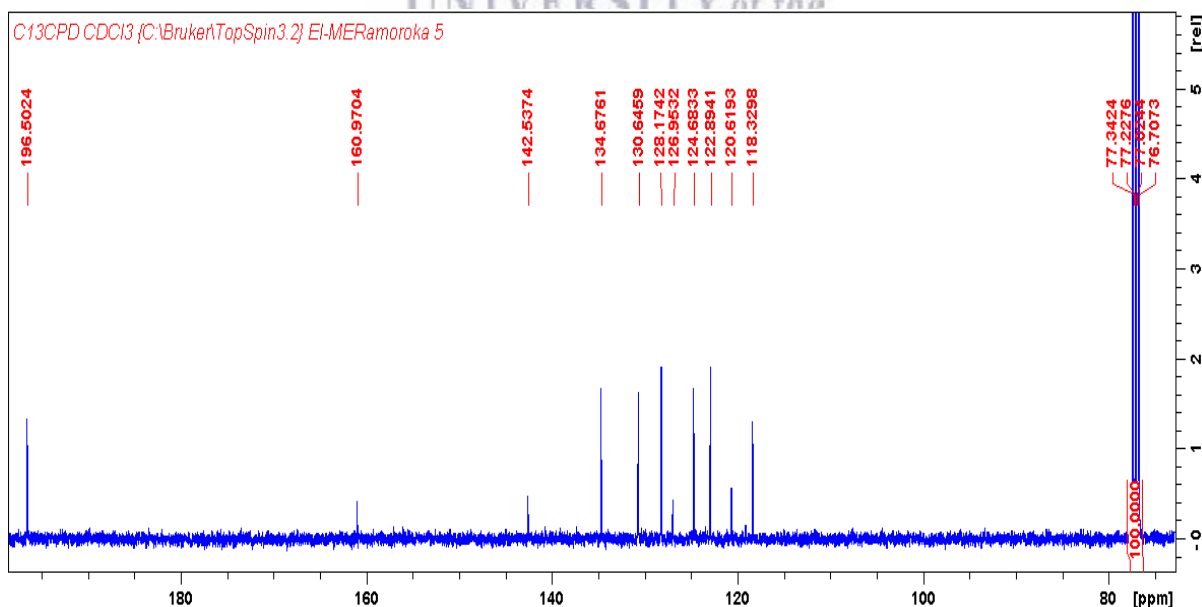


Figure 8.2: ¹³C-NMR spectrum of 5(2-thienyl)salicylaldehyde

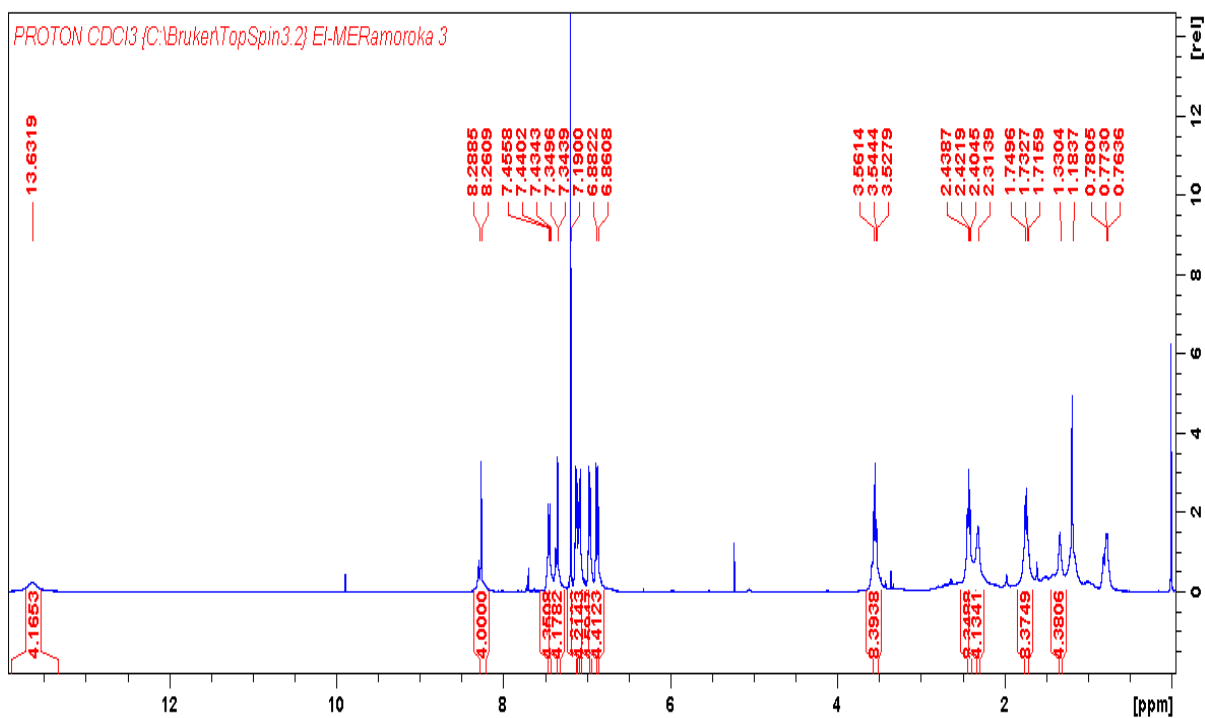


Figure 8.3: $^1\text{H-NMR}$ spectrum of PPI.

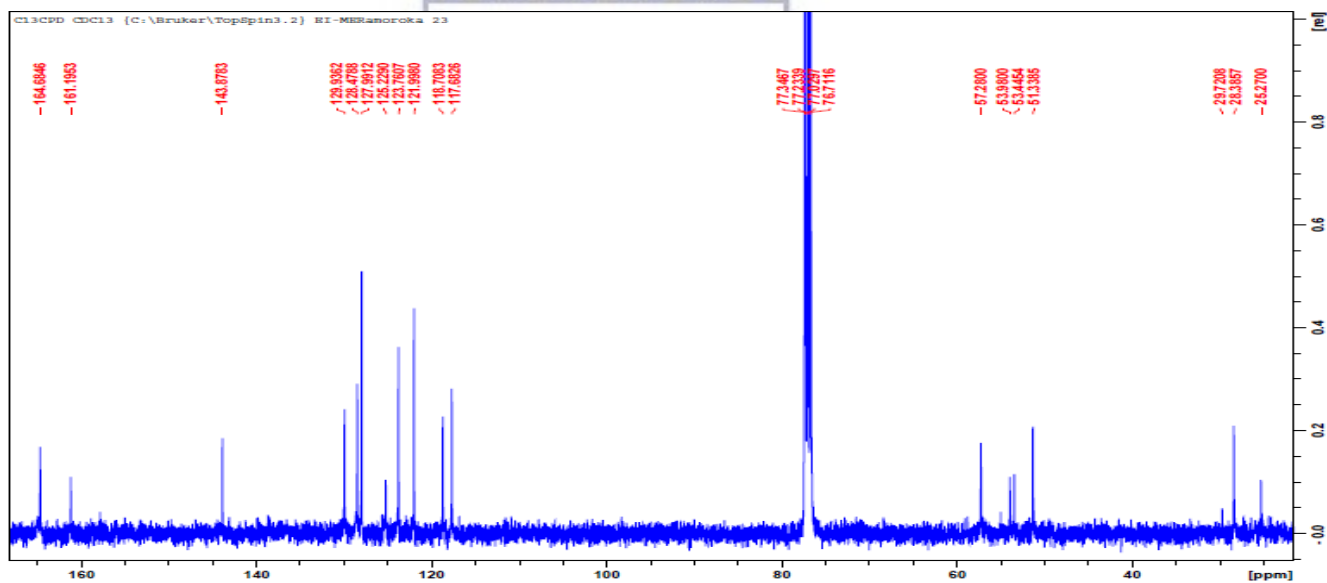


Figure 8.4: $^{13}\text{C-NMR}$ spectrum of PPI.